Title
Vehicle-to-Grid Integration to Power Grids

Author
Wang, Yubo

Publication Date
2017

UNIVERSITY OF CALIFORNIA

Los Angeles

Vehicle-to-Grid Integration to Power Grids

A dissertation submitted in partial satisfaction of the
requirements for the degree of Doctor of Philosophy
in Mechanical Engineering

by

Yubo Wang

2017

ABSTRACT OF THE DISSERTATION

Vehicle-to-Grid Integration to Power Grids

by

Yubo Wang

Doctor of Philosophy in Mechanical Engineering

University of California, Los Angeles, 2017

Professor Rajit Gadh, Chair

Increasing Electric Vehicle (EV) integration to power grid has created additional technical challenges by requiring additional power/energy for charging EVs. With the introduction of Vehicle-to-Grid (V2G), EVs can strategically feed power stored in the batteries back to the power grid for grid supports, shifting their roles from traditional loads to distributed generations.

Different than other types of storages in power grids, the availabilities and energy demands of EVs are subject to change. Traditional deterministic modeling and control methods for Demand Side Management (DSM) of stationary storages failed to capture the stochastic nature in EVs, thus making suboptimal control decisions. This dissertation proposes a stochastic optimization based DSM for energy management of V2G EVs a microgrid setting. In order to make the stochastic problem tractable, a model-free probability density estimation method is utilized together with sample average approximation. Real-life EV data is applied for demonstrating the correctness and merits of the proposed DSM.

As EV penetration continues to grow, the energy management problem becomes oversized to be efficiently solved in a centralized manner. Towards this concern, a distributed DSM for V2G integration into distribution grids is proposed to dispatch the centralized computational burden to distributed nodes. The proposed DSM accounts for both nodal and networked operational cost. To accelerate the computational speed and guarantee convergence, the proposed DSM is tightly relaxed to a convex form using second-order cone programming. Real-life EV data is used to test the proposed DSM in an IEEE benchmark test system.

Most of other existing researches on V2G integration has focused on numerical simulations. As an important area of research, this dissertation shows the design and implementation of two V2G prototypes which could be used as testbed for verification of various V2G applications. One platform is capable of both supplying DC loads and V2G, the other one is capable of bidirectional charging. The prototypes utilize a commercialized EV model with widely used CHAdeMO communication interface. Hardware and software design considerations are shown with test results showing the performances of the prototypes.

This dissertation of Yubo Wang is approved.

Adrienne Lavine

Xiaochun Li

Asad M. Madni

Gaurav N. Sant

Rajit Gadh, Committee Chair

University of California, Los Angeles

2017

To my family.

TABLE OF CONTENTS

LIST OF ACORNYMS

ADMM	Alternating Direction Method of Multipliers
ARMA	Auto-Regressive Moving Average
BESS	Battery Energy Storage System
BMS	Battery Management System
DFS	Discrete Fourier Series
DR	Demand Response
DSM	Demand Side Management
DSO	Distribution System Operator
EV	Electric Vehicle
EVSE	Electric Vehicle Supply Equipment
G2V	Grid-to-Vehicle
KDE	Kernel Density Estimation
k-NN	k-Nearest Neighbors
NN	Neural Network
OPF	Optimal Power Flow
RMSE	Root Mean Squared Error
SAA	Sample Average Approximation
SCADA	Supervisory Control And Data Acquisition
SDSO	Sub-Distribution System Operator
SoC	State-of-Charge
SoE	State-of-Energy

V2G	Vehicle-to-Grid
V2H	Vehicle-to-Home
VR	Voltage Regulation

LIST OF FIGURES

LIST OF TABLES

ACKNOWLEDGEMENT

This work has been sponsored in part by grants from the LADWP/DOE (fund 20699, Smart Grid Regional Demonstration Project) and the California Energy Commission (fund EPC-14-056, Demonstration of PEV Smart Charging and Storage Supporting Grid Operational Needs).

I would like to express my deepest gratitude to my Ph.D advisor Prof. Rajit Gadh for guiding me through my dissertation. He has provided me inspirations during the course of research as well as valuable advice. Most importantly, he taught me the way to conduct independent research and the importance of linking theoretical developments with real-life applications.

I would like to thank my committee members, Prof. Adrienne Lavine, Prof. Xiaochun Li, Prof. Asad M. Madni and Prof. Gaurav N. Sant, for giving me feedbacks on my research. Special thanks to Prof. Madni, who has shared with me a lot of wise advices on both research and career.

I am grateful for the staffs and students at UCLA SMERC: Dr. Peter Chu, Dr. Ching-Yen Chuang, Dr. Joshua Chynoweth, Dr. Wenbo Shi, Dr. Rui Huang, Dr. David Yao, Dr. Bin Wang, Omar Sheikh, Hamidreza Nazaripouya, Zhiyuan Cao, Yingqi Xiong, Tianyang Zhang, Arturo Diaz and HoChang Lee, for their supports and collaborations. Special thanks to two of the visiting scholars to SMERC, Prof. Hemanshu R. Pota and Dr. Boyang Hu, for their significant technical guidance.

I am also thankful for my supervisors at my internships, Dr. Song Zhen at Siemens, and Dr. Jun Wen at Southern California Edison. They made me realize how my PhD research could be applied in industries and create values.

Finally, I am grateful for my family. They are always there for me.

VITA

Educations

2011-2012 M.S in Electrical Engineering, University of California, Los Angeles, U.S.

2007-2011 B.S in Electrical Engineering, Southeast University, Nanjing, China.

Professional Experiences

2016/03-2016/06 Technical Intern, Siemens-Corporate Technology

2016/07-2016/12 Ph.D Intern, Southern California Edison-Advanced Technology

Journal Publications

[1] **Yubo Wang**, Wenbo Shi, Bin Wang, Chi-Cheng Chu and Rajit Gadh, "Optimal Operation of Stationary and Mobil Batteries in Distribution Grids", Applied Energy (Accepted)

[2] **Yubo Wang**, Bin Wang, Chi-Cheng Chu, Hemanshu R. Pota and Rajit Gadh, "Energy management for a commercial building microgrid with stationary and mobile battery storage", Energy and Buildings, 2016, vol. 116, pp.141-150

[3] Bin Wang, **Yubo Wang**, Hamidreza Nazaripouya, Charlie Qiu, Chi-Cheng Chu and Rajit Gadh, "Predictive Scheduling Framework for Electric Vehicle with Uncertainties of User Behavior", IEEE IoT Journal, 2016, vol. PP, no. 99, pp.1-12

[4] Rui Huang, **Yubo Wang**, Chi-Cheng Chu and Rajit Gadh, "Optimal Configuration of Distributed Generation on Jeju Island Power Grid Using Genetic Algorithm: A Case Study", Special Issue on RFID Technologies & Internet of Things in the Journal of Communication Software and Systems, 2014, vol.10, no.2, pp.135-144

Selected Conference Publications

[1] **Yubo Wang**, Bin Wang, Rui Huang, Chi-Cheng Chu, Hemanshu R. Pota and Rajit Gadh, “Two-Tier Prediction of Power Generation with Limited Sensing Resource,” IEEE PES T&D 2016, pp.1-5

[2] **Yubo Wang**, Bin Wang, Tianyang Zhang, Hamidreza Nazaripouya, Chi-Cheng Chu and Rajit Gadh, “Optimal energy management for Microgrid with stationary and mobile storages”, IEEE PES T&D 2016, pp. 1-5

[3] **Yubo Wang**, Omar Sheikh, Boyang Hu, Chi-Cheng Chu and Rajit Gadh, "Integration of V2H/V2G hybrid system for demand response in distribution network," IEEE Smart Grid Communications 2014, pp.812-817

[4] **Yubo Wang**, Hamidreaza Nazaripouya., Chi-Cheng Chu, R. Gadh and Hemanshu R. Pota., "Vehicle-to-grid automatic load sharing with driver preference in microgrids," IEEE ISGT-Europe 2014, pp.1-6

Patents

Zhen Song, Sanjeev Srivastava and **Yubo Wang**, “Adaptive Demand Response Method Using Batteries with Commercial Building for Grid Stability and Sustainable Growth”, 2015P26428 US01(Pending)

1 Introduction

In this chapter, we briefly introduce the backgrounds of this dissertation. This introduction gives a picture of the motivations behind this research, shows the state-of-art of the studied areas, summarizes the key contributions and finally presents the organization of this dissertation. There are introductions in greater details at the beginning of each chapter for specific studied area.

1.1 Motivations

Electric Vehicles (EVs), as alternatives to traditional fuel vehicles, are gaining popularities over the last decades [1]. Such motivations include the major drawbacks of fuel vehicles: energy security [2], air pollution [3], and greenhouse emission concerns [4]. Bearing all these benefits of EVs in mind, the integration of EV to power grid has brought new technical challenges as well as opportunities.

Table 1-1 summarizes popular EV models [5] [6] [7] in the market. The capacity of EV batteries ranges from 16-80 kWh. When comparing these numbers with U.S average household load size of 30 kWh per day [8], the extra load EV introduces will be phenomenon. On the other hand, Table 1-2 summarizes the common charging levels of Electric Vehicle Supply Equipment (EVSE) [9]. In DC fast charging mode, the load power could be as much as 50 kW, creating large impacts on distribution grid. No matter from total energy or instant power point of view, the introduction of EVs create considerable impacts to the power grid. Therefore, EV integration to power grid has caught tremendous attentions and become a heated on-going research.

Table 1-1Popular EV models

Maker	**Nissan**	**Chevrolet**	**Tesla Motor**

Model	Leaf	Volt	Model S
Battery Size (kWh)	24	16	53/80

Table 1-2 Existing charging levels

Charging Levels	**Circuit Rating**	**Peak Power**
AC Level 1	120V/15A	3 kW
AC Level 2	208V/30A	6 kW
DC Level 3	480V/100A	48 kW

1.2 Backgrounds and State-of-Art

1.2.1 Smart Grid

With technology advancement on sensing [10], control [11] and communication [12], the power grid is going through a major shift from less intelligent, unidirectional control and bulk generation to smarter, bidirectional and distributed counterpart [13]. Though there is not a single definition of smart grid, however, the increasing penetration of renewable generations [14], deployment of advanced metering infrastructures [15] and installation of distributed energy resources [16] represent some of the examples of smart grid technology. All these afore mentioned technologies either tried to better balance the generations and loads, or attempted to make the power grid more observable.

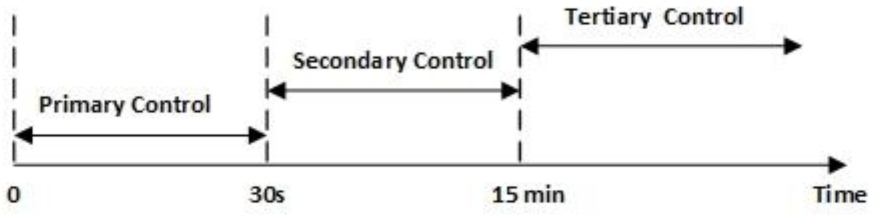

Figure 1-1 Hierarchical control of power grid

As shown in Figure 1-1, the power grid is a hierarchical control system [17]. According to the time that a disturbance is introduced to the system, the control can be generally categorized into primary control, secondary control and tertiary control. The primary control stands for the control that taken action in 0-30s range. The control is automatic which activates in response to the deviation of system set points. Secondary control is activated in the time scale of 30s-15min. It helps the primary controller to restore to new system set points. Accordingly, tertiary control has a longer time step. The hierarchical control of power grid takes into account the different response time of devices, as well as the highly nonlinear nature of power systems. As the primary focus of this dissertation is not the dynamics of devices in short time range, the time step studied in this dissertation is in general greater than 15min.

1.2.2 Vehicle-to-Grid

Interaction of EV with power grid is consist of two separated parts: Grid-to-Vehicle (G2V) and Vehicle-to-Grid (V2G). For G2V, research topics such as smart charging, charging safety and multiplexing of EV Supply Equipment (EVSE) have been extensively studied [18] [19]. The idea of these studies is to understand how EV charging can be better managed to either lower the charging cost [20] or creating less impact to the power grid [21].

On the other hand, by enabling bidirectional power flow with V2G, EV does not merely serve as a load to the grid, but also as distributed storage and generation. The concept of V2G is first proposed by Willet Kempton and Steven Letendre in 1997 [22]. The idea is to use battery in EV as a new source for storing electric energy and send it back to grid at peak loading, which is known as peak shaving. This pioneer research did not acquire much attention at the time it was proposed, as there were not many EVs available on market.

Researchers later found out that the value of ancillary services, i.e. spinning reserves and Voltage Regulation (VR), to be far higher than that of peak power shaving [23]. Spinning reserve refers to additional generation capacity that can provide power quickly, for example within 10 min, upon request from the grid operator [17]. And Automatic Generation Control, is used to fine tune the voltage of the grid by matching generation to load demand [24]. According to [23], the time needed for peak shaving is only a few hundred hours per year. Unlike peak shaving, spinning reserve is paid for the amount of time they are available and ready, not necessarily the amount of energy they produced. And VR is called more often than spinning reserve; say 400 times per day. The combination of spinning reserve and VR has an estimated market value of 12 billion per year in US [24].

1.2.3 Demand Side Management

Conventionally, loads are balanced from the generation side: when load increase/decreases the generation changes accordingly. Demand Side Management (DSM) represents a modern smart grid technology that manages and balance the supply-demand balance from the load side [25] [26]. With the integration of storage devices, the grid operator could shift the peak in load to off-peak time [27]. Battery Energy Storage Systems (BESS) and EVs are examples of such storage devices serving as buffers for shifting the energy usage time.

Previous research on DSM has primarily focused on deterministic controls. Two studies of DSM on a household with one EV and solar generation reported peak shifting with price incentives [28] [29]. Mixed integer linear programming optimization is used in both the papers to achieve minimum operation cost. Chabaud et al. [30] modeled a grid-connected residential building with renewables and battery storage, which confirmed the importance of energy storage device and diversity of renewable generation in cost saving. These researchers assumed perfect knowledge of uncertainty and used deterministic optimization methods for DSM, without considering the loads, EVs and renewable generation's stochastic nature.

Early works have primarily assessed managing the EVs as stationary storages. Extensive studies have been performed assuming the perfect knowledge of EVs' availabilities [31] [32]. However, unlike stationary storages, one of the key features of EVs relies on the uncertainty in their mobility: the EV owners are not committed to pre-defined schedules. The randomness in EV arrival time, leave time and energy demands makes the deterministic DSM less capable of managing stochastically behaved EVs. Though a conceptual incentive program has been designed in [33] for locking down the uncertainty, the urgent need for addressing the uncertainty under established tariff model still widely exists. As an alternative, stochastic behaviors of EVs have been studied using robust optimization [34] and two-stage stochastic programming in [35]. See also [36] for event-based V2G scheduling formulation. These works focused on storage management using a lumped model: the power balance was maintained in one single node, assuming the node to be an isolated from the other nodes on the power system.

1.3 Contributions

Together with many works not cited, the research of EV integration for DSM has been over simplified to isolated deterministic case. The contributions of this dissertation can be summarized as follows:

First of all, EV distinguish itself from other storage device is its stochastic availability and energy demands. This dissertation proposes the first research in which stochastic nature of individual EV is modeled and studied together with other uncertainty elements in a microgrid. A model-free numerical method is applied to make the studied problem tractable. To validate the proposed method, we use real solar generation, building load, EV availabilities and energy demands data to evaluate the performance of the proposed methods.

Secondly, we propose an energy management method that is fully scalable and protects user privacy. The proposed method account for both nodal operational cost and networked optimal over distribution networks. Through tight relaxation, the studied problem is further formulated into convex optimization. A distributed method is applied to solve for the energy management problem. It enables the dispatch of traditional centralized computational burden to distributed nodes. By exchanging Lagrangian variable instead of power/energy information, it protects the privacy of the end users, taking one step closer to practical industrial application. The proposed method is verified numerically on an IEEE benchmark test system using EV data collected on UCLA campus as its inputs.

Thirdly, load sharing, as an important supplementary area of energy management, has a much smaller time step. This dissertation systematically studies load sharing for V2Gs under a microgrid setting. The proposed load sharing takes into account the fact that not only load profile is continuously changing in a microgrid, but also the randomness of the connecting and disconnecting of EVs. The proposed controller takes into account driver preference in which drivers are able to adjust maximum V2G power by setting an upper limit.

Fourthly, most of the researches that studied energy management assumed the perfect knowledge of generation and load profile, which in fact does not exist. This dissertation bridges this gap by proposing a two-tier prediction method. The global-tier utilizes two machine learning algorithms and achieves a comparably high accuracy. In local-tier, unlike most of real-time models, the proposed local-tier prediction is not heuristic. The analytical form local-tier has a clear physical meaning. It can be combined with the global-tier to improve prediction accuracies. The proposed two-tier prediction method is verified using solar generation on UCLA campus.

Lastly, most of existing literatures studies V2G integration through simulations. To the best of the author's knowledge, we prototyped the first V2G system that utilizes commercialized EV and standard communication protocol, which shed light on large scale V2G integration. The implemented platforms have been designed to either drive critical DC load or bidirectional charging. The system is also remotely controllable, allowing it to receive and respond to remote control signals. As a result, the proposed system can be used to test out a lot of ideas mentioned in the literatures.

1.4 Dissertation Organizations

The remainder of this dissertation is organized as follows:

Chapter 2 introduces V2G integration to microgrid. This is a critical area of study, as microgrid owners, such as commercial buildings and university campus, are interested in cutting down the operational cost of the microgrid. Unlike most of the storages, EV distinguish itself from its mobility. The arrival time, departure time and energy demands of EVs are subject to EV owners' behavior, thus are not deterministic. In this chapter, we primarily focus on developing models to capture the uncertainties in EVs. We first describe and model the studied microgrid in a deterministic manner. Then we further develop the modeling of stochastic components in aforementioned deterministic modeling. A model-free method is utilized to capture the stochastic variables in the model. A numerical method is then applied for making the stochastic problem tractable. The proposed methods are verified using real-life building data. This chapter is primarily adapted from [31].

Chapter 3 develops the stochastic model in the previous chapter to account for networked connectivity. Instead of a lumped microgrid, this chapter studies the V2G integration to a distribution network. Unlike the lumped model, the change of a single node in the network more or less impacts the performance of the full network. Therefore, V2G integration needs to be re-evaluated. Furthermore, to account for the increasing EV integration to distribution grid, this chapter studies a distributed method to distribute the once centralized computational burden to distributed nodes. The distributed method could also protect the privacy of the end users. The proposed methods are verified using IEEE benchmark test system.

After studying the energy management in larger time granularity, Chapter 5 studies the control of V2G in a microgrid at much smaller time granularity. The studied problem is crucial in microgrid where loads are shared by generations. We use an EV-connected microgrid to demonstrate the problem and show the challenges and proposed solutions. A physical model is first developed to show the dynamics in the microgrid. Then, a controller with the consideration of driver preference is proposed and analyzed. The difficulty in performing accurate reactive power control is studied. Numerical experiments are performed to demonstrate the merits of the proposed method. This chapter is primarily adapted from [37].

In the previous chapters, when control and optimizations were run for energy management, we assume the perfect knowledge of solar generation and loads in the system. However, in fact they are not known. Chapter 5 studies the uncertainty prediction problem using a solar generation on UCLA campus. A two-tier prediction method is proposed and studied. In the global-tier, two popular machine learning methods are utilized to get offline estimations. In the local-tier, a method to combine the global-tier prediction and real-time measurement is proposed. The studied two-tier prediction method is extensively analyzed and compared. This chapter is primarily adapted from [38].

In Chapter 6, we show the design consideration and implementations of V2G systems. In this chapter, the reasons behind the software and hardware designs are articulated. The prototype systems are documented with implementation details. This chapter is partially adapted from [39]. Finally, conclusions are drawn with projected future research in Chapter 7.

2 V2G Integration to Microgrids

In this chapter, we describe a problem formulation of EV and BESS integration with commercial building, forming a grid connected microgrid. This is a critical area of study, as microgrid owners, such as commercial buildings and university campus, are interested in cutting down the operational cost of the microgrid.

2.1 Introduction

Future smart buildings will incorporate an increasing renewable generation, dispatch units and storage devices, switching from traditional consumptions to distributed and regulated counterparts. With continuous increase EVs and solar penetrations for more than a decade unregulated EV charging together with intermittent solar generation are posing additional challenges on supply-demand balancing in smart buildings [40].

Microgrids represent a vision for distributed generations and consumptions, enhancing the robustness of power grid and creating new ways of utilizing sustainable energy resources [41] [42]. Facilitated by recent advances in DSM, renewable generation and loads are managed in response to variations in the price signal [43] [44]. Coupled with the target of cutting down overall operational cost, DSM collaboratively addresses peak shaving and load shedding with physical and human comfort constrains [45] [46] [47].

The integration of EVs to households and commercial buildings is creating new challenges as well as opportunities [48] [39]. Combined with fluctuations in renewable generation, EVs' randomness in arrival and departure time, State-of-Charge (SoC) and energy demands, all add up to introduce larger uncertainties to the system. The emergence of EVs with V2G capability has also restructured EVs' role from heavy loads to small-sized distributed virtual generators [49]

[37] [50]. Traditional DSM of commercial buildings focuses deterministic modeling methods [51] [52]. It cannot extract the stochastic availabilities and energy demands of EVs. Hence, the DSM design in households and commercial buildings has been a subject of significant ongoing research.

Much of the research in DSM has examined uncertainties caused by renewable generation and EVs with robust optimization. Malysz et al. [53] considered uncertainties in loads and solar generation of a microgrid, and formulated the optimal control of a microgrid as a robust mixed integer linear programming problem. Bai et al. [34] evaluated a robust mixed integer quadratic programming optimization method for large scale V2G for EV aggregator taking into account EV instant power demand uncertainties. Zhang et al. [54] proposed distributed robust optimization algorithms for DSM with intermittent renewable generation in a microgrid. These methods addressed the uncertainties in the systems by estimating the worst case of the uncertainty sets, which might be conservative and resulted in high operational cost.

In [55] [56], the wind generation uncertainties were modeled in a microgrid with probabilistic constrained stochastic programming. The operation cost minimizations were achieved with constraints of utilizing certain percentage of wind generation to meet minimum renewable utilization regulations. These papers considered the load and renewable uncertainties in the power grid, and addressed the stochastic behavior with uncertainty-aware stochastic optimization. However, these researchers did not consider how the randomness of EV’s energy demands, arrival/departure time would interact with the intermittent renewable generation, which if managed improperly, will increase the burden of a microgrid.

Apart from the mixed integer linear programming, mixed integer quadratic programming and convex optimization used in deterministic optimization, robust optimization and stochastic optimization mentioned above, heuristic-based DSM has captured researcher’s attention. Adaptive neuro-fuzzy inference system [57], fuzzy logic [58], and θ-krill herd [59] are some of the examples of heuristic based DSM. Although heuristic based DSM allows operators to achieve multiple optimization goals at the same time, compared to traditional mixed integer linear programming, mixed integer quadratic programming and convex optimization, the heuristic methods cannot be solved with standard solvers and hence may result in longer computational time.

Together with many paper not cited, existing papers have made sound contributions to DSM in households, commercial buildings. However, existing research either failed to consider the effect of EVs’ integration in DSM or did not capture uncertainties in renewable generation, loads and EV modeling. Furthermore, though DSM in households and commercial buildings shares some of the similarities, a commercial building typically has more EVs introducing larger uncertainties on demand side. Hence, DSM of a grid-connected commercial building with renewable generation and EVs needs to be reexamined in details.

This chapter jointly studies DSM in a commercial building microgrid with solar generation, building loads, BESS and EVs. A comprehensive pricing model is proposed which targets at maintaining a low operation cost while utilizing solar generation, stationary BESS and mobile EV storage as much as possible. A deterministic DSM is proposed and then formulated it into a mixed integer linear programming problem. Taking into consideration the stochastic behaviors of solar generation, building loads and EVs, we further develop DSM with two-stage stochastic programming. Sample Average Approximation (SAA) Monte Carlo simulation is used to get numerical results of the proposed DSMs.

The major contributions of this chapter are threefold. Firstly, this chapter describes the first research in which stochastic nature of individual EV is modeled and studied together with other uncertainty elements in a commercial building microgrid setting. Secondly, to validate the proposed DSMs, this chapter uses real solar generation, building load, EV availabilities and EV energy demands data to evaluate the performance of the proposed methods. Finally, this chapter shares detailed comparisons between deterministic DSM and its stochastic counterpart, in terms of price variation, BESS sizing and EV numbers.

The remainder of this chapter is organized as follows: Section 2.2 describes and models the studied system in a deterministic manner. Section 2.3 further develops the stochastic components in deterministic modeling. It is followed by presenting and analyzing numerical results in Section 2.4. Section 2.5 draws conclusions.

2.2 Deterministic Modeling

In this section, we first introduce the system we are studying and show the challenges of DSM under uncertainties. Then, we develop a deterministic model with the estimations on uncertainties. It is followed by modeling the uncertainties in the deterministic model and formulating the DSM into a stochastic model.

2.2.1 System descriptions

This chapter studies a grid-connected commercial building microgrid that a BESS, several EVs and large volume solar generation are integrated to the building. The system architecture of the grid-connected commercial building microgrid is shown in Figure 2-1. As the primary target of this chapter is to analyze how stationary and mobile storage can help in DSM in the context of uncertainties on both supply and demand sides, we intentionally separate EVs and BESS from building load. Other forms of stationary storage exist in commercial buildings such as ice storage unit and heat storage unit [60]. However, BESS allows bidirectional power flow, which adds more flexibility to the DSM design. We evaluate the BESS's impact on DSM, but same modeling technique can be applied for analysis of other stationary storages.

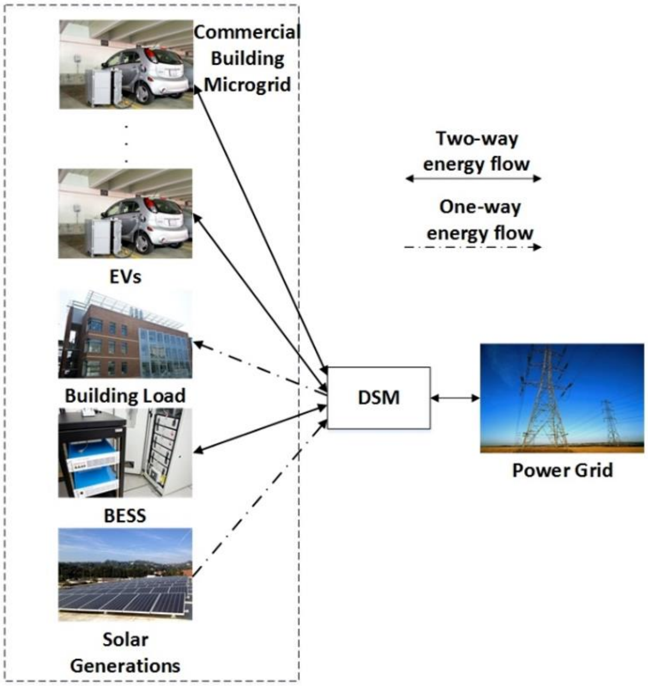

Figure 2-1 Architecture of a grid-connected commercial building microgrid

We take building load data from [61] and 35 kW capacity solar generation data from [62]. The typical weekdays and weekends building loads are shown in Figure 2-2(a) and sunny day solar generation is shown in Figure 2-2(b). Looking at the data we notice that, for the building load, weekday and weekend patterns are distinct. Even though building load in weekdays/weekends follow similar patterns, it is affected by random user behavior, outside temperature, etc., resulting in some fluctuation in load data. Similarly, in Figure 2-2(b), it is shown that in a typical sunny days, solar generations will also have small fluctuations, resulting from cloud shedding and temperature change.

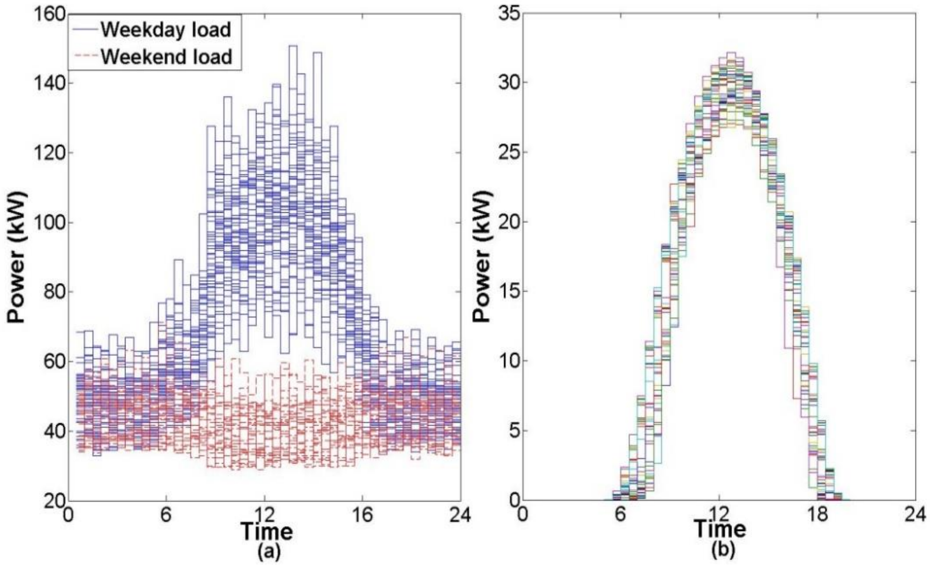

Figure 2-2 Power variations (a) building load on weekdays and weekends (b) solar generation in sunny days

Three anonymous real EV users from UCLA charging networks [63] are studied. They drive a Mistubishi MiEV, a Nissan Leaf and a Nissan Leaf respectively, all with CHAdeMO port for V2G [64]. They come on campus on a daily basis during weekdays and park their car in the parking structure attached to the campus building. The distributions of arrival time, departure time and energy demands shown in Figure 2-3 are extracted from over a year's charging records. And Figure 2-3 is further discussed later on scenario generations. Note that although the data is collected from the UCLA charging networks, these users typically finish their charging long before departure, thus the data is available for the V2G study in the proposed method.

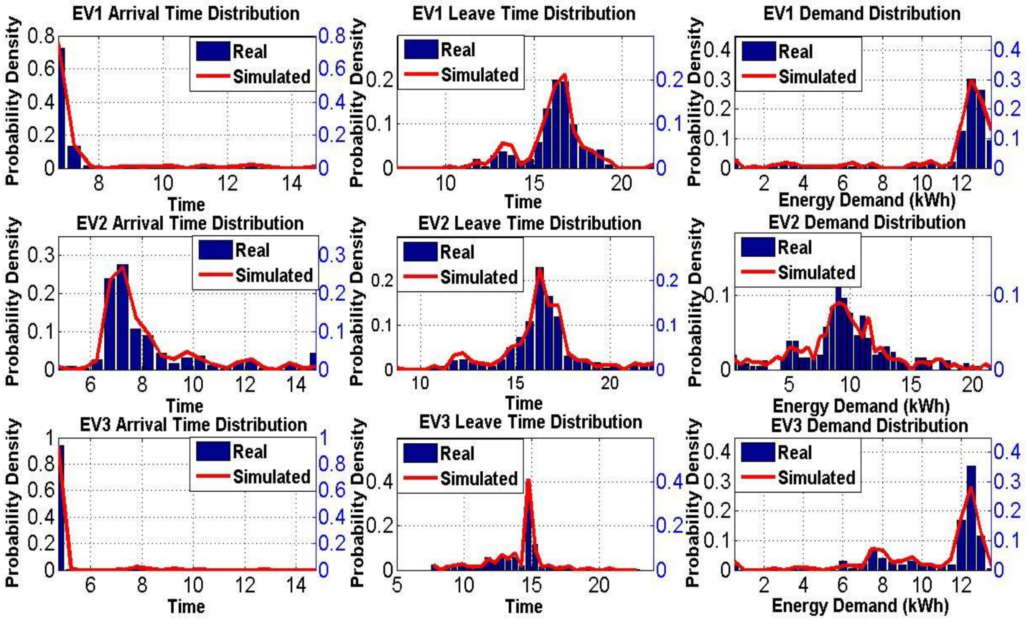

Figure 2-3 Three EV users' distinct behavior

2.2.2 Pricing Model and Cost Function

In this section, we present the detailed modeling of each component shown in Figure 2-1with deterministic models. The inputs to the model are price signals, solar generations, building loads, BESS sizing, EV energy demands and availabilities.

In this chapter, we consider a comprehensive pricing model with day-ahead transactions cost and real-time penalty cost. The commercial building microgrid, needs to provide day-ahead energy purchase/sell decisions before the start of the next day. Furthermore, as the day-ahead buy and sell transactions are based on the estimations of the energy consumption for the next day. A mismatch always exists between the day-ahead predicted energy demands and the real-time consumption, which is compensated with a penalty. The compensated power can be either positive or negative as long as it satisfies the power balance which is discussed later.

The model we use in this chapter is the slotted model, assuming variables stay constant between decision intervals τ. We assume that the price is perfectly known, and the size of the generation and consumption of the commercial building microgrid does not change the price. The economical compensations to EV users for V2G is a very complicated problem including proper business model [65] and battery degrading cost [66], which are not in the scope of this chapter and will be covered in future research. We assume there are H timeslots in a single day. The optimal DSM cost function is formulated as follows:

$$min\ \boldsymbol{c}^{DA}\boldsymbol{p}^{DA}\tau + \boldsymbol{c}^{P}|\boldsymbol{p}^{P}(\boldsymbol{\xi},\boldsymbol{\nu},\boldsymbol{\delta},\boldsymbol{\zeta})|\tau \tag{2.1}$$

where $\boldsymbol{c}^{DA} \in \mathbb{R}^{1\times H}$ is the day-ahead energy sell and buy price, $\boldsymbol{c}^{P} \in \mathbb{R}^{1\times H}$ is the real-time penalty price, τ is the duration of the timeslot, $\boldsymbol{p}^{DA} \in \mathbb{R}^{H}$ is the day-ahead buy and sell power and $\boldsymbol{p}^{P} \in \mathbb{R}^{H}$ is real-time penalty power. The operation cost includes day-ahead buying and selling cost and real-time penalty cost. Given that uncertainties exist in renewable generation, loads, EV availabilities and energy demands, we use estimation of each uncertainty in the deterministic model. The estimation method is discussed in Section 2.3.

2.2.3 Power balancing and grid constraints

At any time instance of the slotted model, the power flowing into the commercial building microgrid should be always equal to the power flowing out, which is modeled as follows:

$$\sum_{i=1}^{M}\boldsymbol{p}_d^{EV,i}(\boldsymbol{\delta_i},\boldsymbol{\zeta_i}) + \boldsymbol{p}^{solar}(\boldsymbol{\xi}) + \boldsymbol{p}_d^{B} + \boldsymbol{p}^{DA} = \sum_{i=1}^{M}\boldsymbol{p}_c^{EV,i}(\boldsymbol{\delta_i},\boldsymbol{\zeta_i}) + \boldsymbol{p}^{load}(\boldsymbol{\nu}) + \boldsymbol{p}_c^{B} + \boldsymbol{p}^{P}(\boldsymbol{\xi},\boldsymbol{\nu},\boldsymbol{\delta},\boldsymbol{\zeta}) \tag{2.2}$$

where M is the number of EV, $\boldsymbol{p}^{solar} \in \mathbb{R}^{H}$ is the solar generation power, $\boldsymbol{p}^{load} \in \mathbb{R}^{H}$ is the building load power, $\boldsymbol{p}_c^{B}/\boldsymbol{p}_d^{B} \in \mathbb{R}^{H}$ denotes BESS charging/discharging power, $\boldsymbol{p}_c^{E,i}/\boldsymbol{p}_d^{E,i} \in \mathbb{R}^{H}$ denotes charging/discharging power of EV i. Note that uncertainties of load and solar generation are represented by $\boldsymbol{p}^{solar}(\boldsymbol{\xi})$ and $\boldsymbol{p}^{load}(\boldsymbol{\nu})$. The uncertainties in EV energy demands and availabilities are represented by $\boldsymbol{\delta_i}, \boldsymbol{\zeta_i}$. $\boldsymbol{p}^{DA}$, $\boldsymbol{p}_d^B$, $\boldsymbol{p}_c^B$ are all decision variables that are needed to be determined day-ahead, while solar generation, building loads and EV availabilities and energy demands will not be exactly known until the next day. In this model, we address the uncertainties in a deterministic perspective, i.e., using estimations for each uncertainty in DSM.

We need further constraints to control the behavior of power injected to the power grid.

$$\underline{P^{grid}} \leq \boldsymbol{p}^{DA} + \boldsymbol{p}^{P} \leq \overline{P^{grid}} \tag{2.3}$$

$$\underline{P_{step}^{DA}} \leq (\boldsymbol{p}^{DA})_j + (\boldsymbol{p}^{DA})_{j+1} \leq \overline{P_{step}^{DA}}, \quad j = 1,2,\dots,H-1 \tag{2.4}$$

where $(\boldsymbol{p}^{DA})_j$ denotes row j of $\boldsymbol{p}^{DA}$. $\underline{P^{grid}}/\overline{P^{grid}} \in \mathbb{R}$ denotes the Minimum/maximum allowed $\boldsymbol{p}^{DA}$, $\underline{P_{step}^{DA}}/\overline{P_{step}^{DA}} \in \mathbb{R}$ denotes minimum/maximum allowed $\boldsymbol{p}^{DA}$ step variation between consecutive timeslots. Eq.2.3 limits the maximum power that the commercial building microgrid can buy from and sell to the grid due to line capacity. Eq.2.4 regulates the variation of power in day-ahead market, so that the shaping of day-ahead power is smoother and more predictable to the utilities.

2.2.4 BESS modeling

The modeling of BESS includes power, energy and state constraints as follows:

$$\boldsymbol{0} \leq \boldsymbol{p}_c^B \leq \overline{P_c^B}\boldsymbol{\sigma}^B \tag{2.5}$$

$$\boldsymbol{0} \leq \boldsymbol{p}_d^B \leq \overline{P_d^B}(\boldsymbol{1} - \boldsymbol{\sigma}^B) \tag{2.6}$$

$$P_{c,lim}^B \boldsymbol{\sigma}_c^B \leq \boldsymbol{p}_c^B \leq P_{c,lim}^B(\boldsymbol{1} - \boldsymbol{\sigma}_c^B) + \overline{P_c^B}\boldsymbol{\sigma}_c^B \tag{2.7}$$

$$P_{d,lim}^B \boldsymbol{\sigma}_d^B \leq \boldsymbol{p}_d^B \leq P_{d,lim}^B\left(\boldsymbol{1} - \boldsymbol{\sigma}_d^B\right) + \overline{P_d^B}\boldsymbol{\sigma}_d^B \tag{2.8}$$

$$(\boldsymbol{\sigma}_c^B)_j + (\boldsymbol{\sigma}_c^B)_{j+1} \leq 1, \quad j = 1,2,\dots,H-1 \tag{2.9}$$

$$(\boldsymbol{\sigma}_d^B)_j + (\boldsymbol{\sigma}_d^B)_{j+1} \leq 1, \quad j = 1,2,\dots,H-1 \tag{2.10}$$

$$\underline{SoC^B}\mathbf{1} \leq SoC_I^B\mathbf{1} + \boldsymbol{h}^B(\boldsymbol{p}_c^B\eta_c^B - \boldsymbol{p}_d^B/\eta_d^B) \leq \overline{SoC^B}\mathbf{1} \tag{2.11}$$

$$SoC_F^B = SoC_I^B + (\boldsymbol{h}^B)_{end}(\boldsymbol{p}_c^B\eta_c^B - \boldsymbol{p}_d^B/\eta_d^B) \tag{2.12}$$

where $\overline{P_c^B}/\overline{P_d^B} \in \mathbb{R}$ is the maximum allowed BESS charging/discharging power. $P_{c,lim}^B/P_{d,lim}^B \in \mathbb{R}$ is the BESS charging/discharging high power region limitation, $\eta_c^B/\eta_d^B \in \mathbb{R}$ is the charging/discharging efficiency of BESS, $\underline{SoC^B}/\overline{SoC^B} \in \mathbb{R}$ denotes the BESS minimum/maximum SoC, $SoC_I^B/SoC_F^B \in \mathbb{R}$ denotes BESS initial/final SoC, $\boldsymbol{\sigma}^B \in \mathbb{Z}^H$ is binary BESS status indicating charging or discharging, and $\boldsymbol{\sigma}_c^B/\boldsymbol{\sigma}_d^B \in \mathbb{Z}^H$ is binary status indicating BESS operating in high power charging/discharging region. We use $\mathbf{1} \in \mathbb{Z}^H$ to denote all 1 column vector. $\boldsymbol{h}^B$ is an ancillary matrix that is used for calculating the SoC at each decision interval τ; $(\boldsymbol{h}^B)_{end}$ denotes the last row of the $\boldsymbol{h}^B$ matrix. Eq.2.5 and Eq.2.6 limit the maximum charging and discharging power for BESS so that it does not exceed physical limitations. It is reported in [53] that BESS can operate in high power charging/discharging region for peak demand, however for only a limited time. Eq.2.7 -Eq.2.10 ensure that the BESS will not consecutively operate in high power charging/discharging region consecutively for more than one time slot. Integer decision variables $\boldsymbol{\sigma}^B, \boldsymbol{\sigma}_c^B, \boldsymbol{\sigma}_d^B$ are introduced in Eq.2.5-Eq.2.10 for regulating the BESS operation status. Taking into consideration that deep discharge will affect the Lithium-ion battery's lifecycle [67], Eq.2.11 constrains the SoC of BESS so that it does not violate physical constraints and operate in deep discharge region. See a detailed study in [68]. In the end, Eq.2.12 defines the final SoC for BESS after a day's operation.

2.2.5 EV modeling

The modeling of EV has to consider the uncertainties in demand, arrival time, and departure time. We develop the model with uncertainties bore in mind using estimation for each uncertainty variable as follows:

$$\underline{P_c^{E,i}}\boldsymbol{\sigma}_c^{E,i} \leq \boldsymbol{p}_c^{E,i} \leq \overline{P_c^{E,i}}\boldsymbol{\sigma}_c^{E,i},\ \ \forall i \tag{2.13}$$

$$\underline{P_d^{E,i}}(\mathbf{1}-\boldsymbol{\sigma}_c^{E,i}) \leq \boldsymbol{p}_d^{E,i} \leq \overline{P_d^{E,i}}(\mathbf{1}-\boldsymbol{\sigma}_c^{E,i}),\ \ \forall i \tag{2.14}$$

$$\mathbf{0} \leq \boldsymbol{\sigma}_c^{E,i} \leq \boldsymbol{\sigma}^{E,i}(\boldsymbol{\delta_i}),\ \ \forall i \tag{2.15}$$

$$\underline{SoC^{E,i}}\mathbf{1} \leq SoC_I^{E,i}(\boldsymbol{\zeta_i})\mathbf{1} + \boldsymbol{h}^{E,i}\left(\boldsymbol{p}_c^{E,i}\eta_c^{E,i} - \boldsymbol{p}_d^{E,i}/\eta_d^{E,i}\right) \leq \overline{SoC^{E,i}}\mathbf{1},\ \ \forall i \tag{2.16}$$

$$SoC_F^{E,i} = SoC_I^{E,i}(\boldsymbol{\zeta_i}) + (\boldsymbol{h}^{E,i})_{end}(\boldsymbol{p}_c^{E,i}\eta_c^{E,i} - \boldsymbol{p}_d^{E,i}/\eta_d^{E,i}),\ \ \forall i \tag{2.17}$$

where $\underline{P_c^{E,i}}/\overline{P_c^{E,i}} \in \mathbb{R}$ is the minimum/maximum charging power of EV i, $\underline{P_d^{E,i}}/\overline{P_d^{E,i}} \in \mathbb{R}$ is minimum/maximum discharging power of EV i, and $\boldsymbol{\sigma}^{E,i} \in \mathbb{Z}^H$ denotes the availability matrix of EV i. We use $\underline{SoC^{E,i}}/\overline{SoC^{E,i}} \in \mathbb{R}$ to denote minimum/maximum allowed SoC of EV i, $\eta_c^{E,i}/\eta_d^{E,i} \in \mathbb{R}$ denotes charging/discharging efficiency of EV i, $SoC_I^{E,i}/SoC_F^{E,i} \in \mathbb{R}$ represents initial/final SoC of EV i and $\boldsymbol{\sigma}_c^{E,i} \in \mathbb{Z}^H$ indicates binary status indicating EV i charging or discharging. Similar to $\boldsymbol{h}^B$, $\boldsymbol{h}^{E,i}$ is ancillary matrix that for calculating the SoC of EV i at each decision interval τ $(\boldsymbol{h}^{E,i})_{end}$ denotes the last row of the $\boldsymbol{h}^{EV,i}$ matrix. Eq.2.13 and Eq.2.14 model the limits of charging and discharging power for each EV. Without loss of generality, integer decision variables are introduced in Eq.2.13 and Eq.2.14 are for modeling the charging and discharging losses in Eq.2.16 and Eq.2.17. Also, integer variables are introduced due to the fact that both charging and discharging need to reach minimum power, making the power output of

EVs discontinuous. The uncertainty of EV availabilities is reflected in $\boldsymbol{\sigma}^{E,i}(\boldsymbol{\delta_i})$ in Eq.2.15, which actually models the stochastic arrival and departure time of each EV. The uncertainty of energy demand for each EV is captured with $SoC_I^{E,i}(\boldsymbol{\zeta_i})$ in both Eq.2.16 and Eq.2.17. As these uncertainties exist in each EV, the corresponding decision variables $\boldsymbol{p}_c^{E,i}$ and $\boldsymbol{p}_d^{E,i}$ are naturally subject to uncertainties, which are linked to Eq.2.2. It is noted that in deterministic model we recognize the existence of EV behavioral uncertainties. We use estimations for each uncertainty, which is discussed in Section 2.3.

2.3 Stochastic DSM

The deterministic model is a favorable solution to DSM in commercial building microgrid however not without problems. Looking at Figure 2-2 and Figure 2-3, building load and solar generation follow some trends, however still present fluctuations due to unpredictable factors such as random user behavior and cloud shedding. On the other hand, EV arrival and departure time and energy demands are subject to the EV owner behaviors, which are hard to predict. In addition, as the EV number increases, the charging/discharging of EVs will become a major load/generation to commercial buildings in the future. How to make decisions on day-ahead energy transactions and BESS operation under the context of larger uncertainties becomes challenging, which gives rise to stochastic DSM.

2.3.1 Stochastic Reformulation

Instead of optimizing cost function under uncertainties with estimation in Eq.2.1, we now optimize the expectation of the cost function. The problem is then formulated into a two-stage stochastic programming problem as follows:

$$min\ \boldsymbol{c}^{DA}\boldsymbol{p}^{DA}\tau + \boldsymbol{c}^{P}\mathbb{E}\{|\boldsymbol{p}^{P}(\boldsymbol{\xi},\boldsymbol{\nu},\boldsymbol{\delta},\boldsymbol{\zeta})|\tau\} \tag{2.18}$$

$\boldsymbol{p}^{DA}$ are first-stage decision variables while $\boldsymbol{p}^{P}$ are second-stage decision variables. We are optimizing first-stage day-ahead transactions in the context of second-stage expectation.

Here we briefly introduce two-stage stochastic linear programming. A typical two-stage stochastic linear programming can be formulated as minimization over expectation [69]:

$$\begin{gathered} min\, c^T x + \mathbb{E}[Q(x,\delta)] \\ s.t. Ax \leq B \\ Cx = D \end{gathered}$$

where x are the first-stage decision variables, δ denotes the uncertainty sets, $\mathbb{E}[Q(x,\delta)]$ is the optimum of the second-stage problem:

$$\begin{gathered} min\, q^T y \\ s.t. Tx + Wy \leq h \end{gathered}$$

where y are the second-stage variables, and uncertainty sets $\delta = \{q, T, W, y\}$. The two-stage problem can be interpreted as optimizing first-stage plus the expectation of the second-stage problem when uncertainties are not known. Second-stage problem on the other hand describes the optimization problem when the uncertainties are revealed.

Given the stochastic nature of renewable generation, loads, and EV availabilities and demands, we may want to extract the distribution of each uncertainty and formulate the expectation in Eq.2.18 analytically. However, even if we may be able to extract the distribution of each random variable, the requirement to know joint distribution of a number of uncertainties in the optimization problem such as Eq.2.1-Eq.2.17 make the problem hard to solve. Instead we seek to use SAA and solve the optimization problem numerically.

2.3.2 Sample Average Approximation

SAA is a Monte Carlo simulation technique that serves as a statistical inference of the original problem (in this case Eq.2.18). The idea behind it is to generate a large pool of samples of uncertainties based on their empirical distributions where each sample is called a scenario. Then solve the second-stage problems with each scenario before averaging them out to approximate the original problem. For a detailed discussion, see [69].

Without loss of generality, it is assumed that we generate N independent scenarios. The method of scenario generation is detailed in Section 2.3.3. Each scenario is one possible realization of the uncertainties, which includes solar generation, building loads, EV availabilities and energy demands. Hence, the power balance and EV constraints, which involve uncertainties, are updated as follows:

$$\sum_{i=1}^{M} \boldsymbol{p}_{d,s}^{EV,i} + \boldsymbol{p}_{s}^{solar} + \boldsymbol{p}_{d}^{B} + \boldsymbol{p}^{DA} = \sum_{i=1}^{M} \boldsymbol{p}_{c,s}^{EV,i} + \boldsymbol{p}_{s}^{load} + \boldsymbol{p}_{c}^{B} + \boldsymbol{p}_{s}^{P}, \ \ \forall s \tag{2.19}$$

$$\underline{P_c^{E,i}}\boldsymbol{\sigma}_{c,s}^{E,i} \le \boldsymbol{p}_{c,s}^{E,i} \le \overline{P_c^{E,i}}\boldsymbol{\sigma}_{c,s}^{E,i}, \ \ \forall i, \forall s \tag{2.20}$$

$$\underline{P_d^{E,i}}(\mathbf{1} - \boldsymbol{\sigma}_{c,s}^{E,i}) \le \boldsymbol{p}_{d,s}^{E,i} \le \overline{P_d^{E,i}}(\mathbf{1} - \boldsymbol{\sigma}_{c,s}^{E,i}), \ \ \forall i, \forall s \tag{2.21}$$

$$\mathbf{0} \le \boldsymbol{\sigma}_{c,s}^{E,i} \le \boldsymbol{\sigma}_{s}^{E,i}, \ \ \forall i, \forall s \tag{2.22}$$

$$\underline{SoC^{E,i}}\mathbf{1} \le SoC_{I,s}^{E,i}\mathbf{1} + \boldsymbol{h}_{s}^{E,i}\left(\boldsymbol{p}_{c,s}^{E,i}\eta_c^{E,i} - \boldsymbol{p}_{d,s}^{E,i}/\eta_d^{E,i}\right) \le \overline{SoC^{E,i}}\mathbf{1}, \ \ \forall i, \forall s \tag{2.23}$$

$$SoC_{F,s}^{E,i} = SoC_{I,s}^{E,i} + \left(\boldsymbol{h}_{s}^{E,i}\right)_{end}(\boldsymbol{p}_{c,s}^{E,i}\eta_c^{E,i} - \boldsymbol{p}_{d,s}^{E,i}/\eta_d^{E,i}), \ \ \forall i, \forall s \tag{2.24}$$

Eq.2.19 shows the power balance within each scenario. The subscript s denotes scenario number s among N generated scenarios. Eq.2.22 presents the realization the EV availabilities uncertainty by generating $\boldsymbol{\sigma}_{s}^{E,i}$ in each scenario. Similarly, Eq.2.23 and Eq.2.24 address EV energy demands uncertainty by $SoC_{I,s}^{E,i}$ and $SoC_{F,s}^{E,i}$. It is noted that Eq.2.19-Eq.2.24 should hold within each generated scenario and for all N scenarios. Consequently, the stochastic DSM is formulated as follows:

$$min\ \boldsymbol{c}^{DA}\boldsymbol{p}^{DA}\tau + \frac{1}{N}\sum_{s=1}^{N}\boldsymbol{c}^{P}|\boldsymbol{p}_{s}^{P}|\tau \tag{2.25}$$

s.t. (3.3)-(3.12), (3.19)-(3.24)

Using Eq.2.25, we approximate the original problem (Eq.2.18) with SAA. It has been reported in [70] that a two-stage stochastic programming with integer first-stage and second-stage variables can be approximated by SAA. Furthermore, SAA exponentially approximates the true problem as scenario size *N* increases.

On feasibility side, the problem is always feasible as long as the EV constraints can be met. The worst case is when an EV user submits an energy demand that needs charging from arrival to departure. However, it is rarely seen for the EV owners we studied. On grid side, there is no upper and lower bounds for $\boldsymbol{p}_s^P$ so that the power balance constraints can always be met in Eq.2.19.

2.3.3 Model-free Probability Density Estimation

In the previous section, we model the EV with stochastic variables, showing the sources of uncertainties in EVs. This section presents the method to model the distribution of stochastic variables, which will be used in numerical approximations in the following section. The method studied in this section can be applied to EVs with different arrival time, departure time and energy demands.

Given an empirical realization of certain stochastic variable, here we present Kernel Density Estimation (KDE) to capture the empirical probability density. The mathematical representation of KDE is described as follows:

$$\rho(x) = \frac{1}{N}\sum_{i=1}^{N} K(\frac{x - x_i}{b}) \tag{2.25}$$

where N is the number of kernels used, x_i is the center of one kernel, b denotes the bandwidth of the kernel, $K(\cdot)$ is the kernel function, and $\rho(\cdot)$ is the probability density function.

Empirical probability density is usually given in histogram. The center of the each kernel naturally falls into the center of each bin. The number of kernels is equal to the number of bins in the histogram. The bandwidth then becomes the only free parameter to be determined. A common way to determine the bandwidth is to use the rule-of-thumb principle described in [71]. After determining each parameters, the discrete histogram can be modeled by continuous KDE. This KDE is then utilize for scenario generation in the following section.

2.3.4 Sample Average Approximation Bounds Estimation

SAA is a statistical inference of the original problem. We generate scenarios before solving the SAA problem. As the scenario is generated based on empirical distribution, naturally, we will have slightly different SAA results if we solve the SAA problem for multiple times. This gives rise to evaluation of the SAA, in which we need to examine how closely the SAA optimum approximates that of the original problem. We follow the methods in [70] to find out the upper and lower bounds for the SAA problem. The algorithm is tabulated in Algorithm 2.1. Before start of iteration, we set *k=1*. Then we generate *N i.i.d.* scenarios based on the scenario generation method described above. We solve the stochastic DSM (Eq.2.25) using the generated *N* samples. Then, we store the first-stage variables $\boldsymbol{p}^{DA}, \boldsymbol{p}_c^B, \boldsymbol{p}_d^B, \boldsymbol{\sigma}^B, \boldsymbol{\sigma}_c^B, \boldsymbol{\sigma}_d^B$ as $\boldsymbol{x}$ and optimum as $opt(k)$. It is followed by generating *N' i.i.d.* scenarios, typically, $N' \gg N$. We solve Eq.2.25 with the fixed stored first-stage variables $\boldsymbol{x}$ minimizing over only second-stage decision variables which includes $\boldsymbol{p}_s^p, \boldsymbol{p}_{c,s}^{E,i}$ and $\boldsymbol{p}_{d,s}^{E,i}$. The optimum for the scenario *N'* is denoted as $\overline{opt}(k)$. We iterate the procedure for K times where K is a predefined number. The optimization gap can be estimated using opt and $\overline{opt}$.

Algorithm 2.1: SAA upper and lower bound estimation

```
for k=1 to K do
    Generate N scenarios, solve (2.25)
        $\boldsymbol{x}$ ← first-stage variables $\boldsymbol{p}^{DA}, \boldsymbol{p}_c^B, \boldsymbol{p}_d^B, \boldsymbol{\sigma}^B, \boldsymbol{\sigma}_c^B, \boldsymbol{\sigma}_d^B$
        $opt(k)$ ← optimum
    Generate N' scenarios, solve (2.25) with fixed $\boldsymbol{x}$
        $\overline{opt}(k)$ ← optimum
end
upper bound $\overline{opt^*}$ ←minimum of $\overline{opt}$
lower bound $\underline{opt^*}$ ←average of $opt$
optimality gap $g \leftarrow (\overline{opt^*} - \underline{opt^*})/\underline{opt^*} \times 100\%$
```

2.4 Results and Analysis

In this section, we validate the proposed DSMs. We first describe how we generate the scenarios based on the collected data. It is followed by a case study of the system and analysis on computational results.

2.4.1 Scenarios generation

We first classify the historical load data into weekdays and weekend, and solar generation data into sunny, cloudy and rainy groups. Solar generation and load behave differently between groups while showing similarity within each group. Before running DSM, we pick corresponding solar generation and load data from historical data based on the forecast/knowledge of the next day. In this chapter, we investigate the performance of the DSM on sunny weekdays. However, the methodology used in this chapter can be also applied to weekdays/weekends with other weather conditions. We capture the distribution of the real data shown in Figure 2-2 and Figure 2-3 with KDE. We use the KDE modeled distribution to generate scenarios and compare them with real distribution of EV user behavior shown in Figure 2-3. The comparison demonstrates a close match between the KDE simulated data and the real distribution.

Table 2-1 summarizes some of the key parameters used in the following computational case study. We use τ=0.5 h. The BESS data is taken from a real BESS in the University of California, Los Angles, laboratory. EV maximum charging power is a typical number for charging in Level II circuits [72]. For EV discharging power, we refer to the industrial product in [73]. In the following case study, EV energy demands are recognized as the energy required to fully charge the corresponding EV from its initial SoC. Moreover, we set initial SoC of BESS equal to its final SoC after a day's operation. Figure 2-4 shows the day-ahead price and real-time penalty price from CAISO. We increase the penalty price by twenty five percent to see the performance of the two DSMs. The penalty price sensitivity is studied in discussion section, showing that the DSMs proposed in this chapter work generally well in a wide range of prices. The proposed DSMs are solved with commercial solver Gurobi [74] on a PC with 3.1GHz CPU and 16 GB RAM.

Table 2-1 Key parameters

Item	Value	Item	Value
BESS battery size	70 kWh	**Mitsubishi MiEV battery size**	16 kWh
BESS initial and final SoC	0.6	**Nissan Leaf battery size**	24 kWh
BESS maximum charging power	40 kW	**EV maximum charging power**	6.6 kW
BESS maximum charging power	20 kW	**EV maximum discharging power**	2.0 kW
Min/max allowed $\boldsymbol{p^{DA}}$	150 kW	**Min/max allowed $\boldsymbol{p^{DA}}$ variation**	15 kW

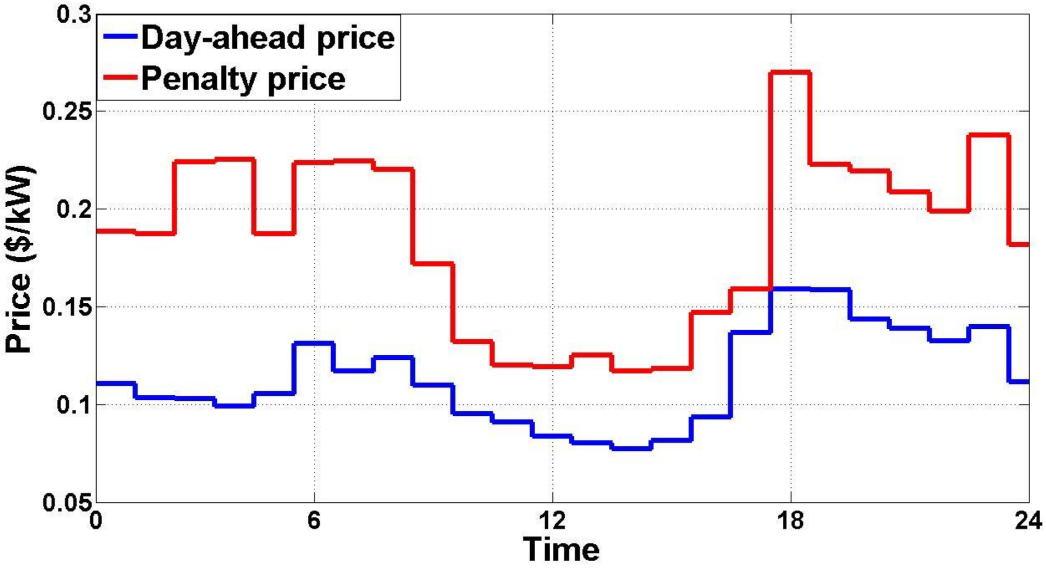

Figure 2-4 Price for a 24 hour period from CAISO

2.4.2 Case study

We apply the proposed stochastic DSM to a microgrid that is made up of a grid-connected commercial building with weekday building load. Figure 2-5 presents computation results of the building profile of a day. From the figure we can see that $\boldsymbol{p}^{DA}$ variation is limited by the maximum step $\underline{P_{step}^{DA}}$ and $\overline{P_{step}^{DA}}$. Consequently day-ahead power is smoother and easier to follow on utility side. Looking at BESS power output, we see the high power region restrictions work correctly so that the BESS will not keep operating in excessive high power regions. Solar generation, $\boldsymbol{p}^{P}$ and loads are plotted for one typically scenario among many of the generated scenarios in Figure 2-5. We observe that the real-time power mismatch between the day-ahead planning and real-time operation, which is compensated by $\boldsymbol{p}^{P}$, is relatively small compared to day-ahead bidding power $\boldsymbol{p}^{DA}$. It allows utilities to better plan generations and reduces real-time uncertainties.

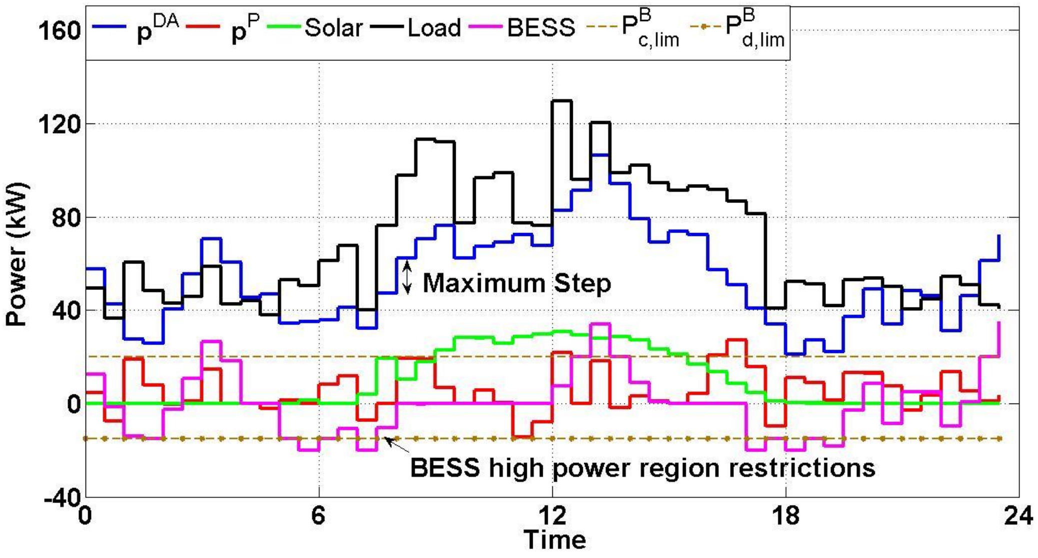

Figure 2-5 Building profile of a day

Figure 2-6 shows the EV profile of the same scenario. We can see that three EVs arrive and depart at different times. They arrive with different SoCs and leave with fully charged batteries. Depending on the energy demand of each EV, they operate in V2G mode to support the building grid. Figure 2-5 together with Figure 2-6 demonstrates the correctness of the proposed stochastic DSM.

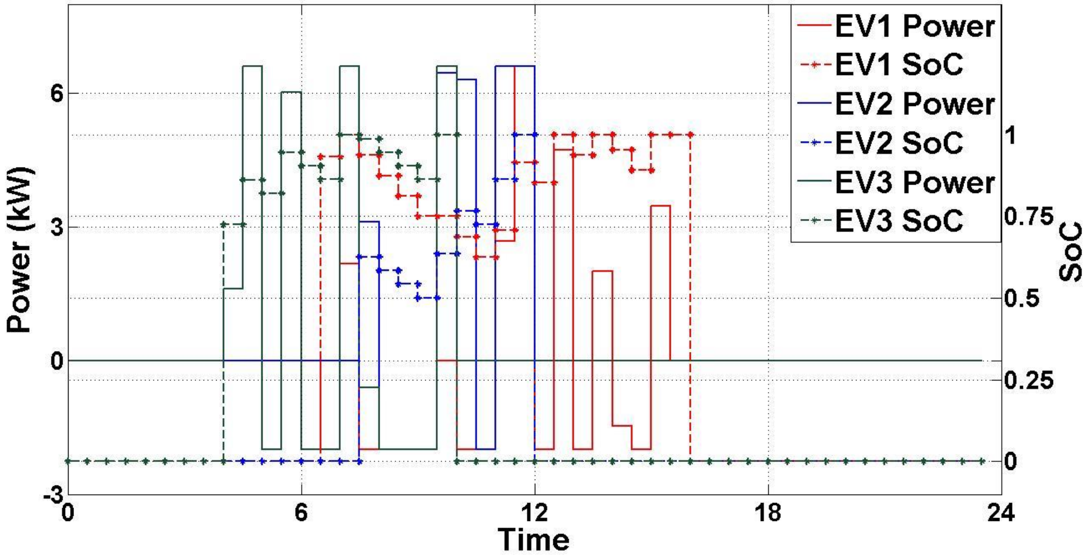

Figure 2-6 EV profile of a day

Besides examining the building and EV profile, we want to find out how closely SAA approaches the original problem. We follow the steps in Algorithm 2.1 and choose *K=10* to test the optimality gap. From the results summarized in Table 2-2, we can find out that in general the problem is tightly bounded. The computational time includes time consumed for both sample size *N* and *N'*, in which time for *N'* is much larger than *N*. Looking at the results we may safely conclude that using the lower bound of *N/N'=50/500*, which is calculated by solving the 50 scenario problem for 10 times, is good enough for producing accurate results. We use the lower bounds estimated with *N=50* in the following simulations of stochastic DSM. It consumes much less time compared with the estimation using the upper bound.

Table 2-2 Optimality gaps estimations of SAA

N/N'	Upper bound	Lower bound	Optimality Gap	Computational Time (s)
20/200	171.53	170.51	0.60%	1088.7
30/300	171.52	170.38	0.67%	2297.1
50/500	171.74	171.02	0.427%	5607.8

2.4.3 Discussions

1) *Deterministic vs. stochastic.* It is interesting to examine the difference between the proposed deterministic DSM and stochastic DSM. In the proposed deterministic DSM, we use average value of each uncertainty variables as their estimations. We verify the performance of both deterministic and stochastic DSMs with 50 generated scenarios for 10 times. We compare how different load can affect the performance of the two studied DSMs by using the weekdays and weekends building load previously plotted in Figure 2-2. The simulation settings are kept the

same as it is in Section 2.3 except for building load. The comparison results are tabulated in Table 2-3. It demonstrates that the proposed stochastic DSM outperforms its deterministic counterpart no matter under weekdays or weekend building load. In weekday cases, stochastic DSM shows (179.44-171.09)/171.09=4.88% outperformance, while (113.34-107.25)/107.25=5.67% outperformance in weekends. The outperformance in operation cost saving is at the expense of higher computational time. For a DSM that handles day-ahead planning, a longer time is tolerable.

Table 2-3 Comparisons of deterministic DSM and stochastic DSM

	Deterministic DSM cost	**Stochastic DSM cost**	**Deterministic DSM computational time**	**Stochastic DSM computational time**
Weekdays	$179.44	$171.09	4.23 s	248.83 s
Weekends	$113.34	$107.25	5.14 s	316.88 s

In order to determine the solar capacity’s influence on the proposed DSMs, we study the performance of two DSMs under wide solar power generation variation. We run numerical experiment with exactly same setting as it is in Section 2.3, except for varying the solar capacity. The results are presented in Figure 2-7. The same solar generation data is used for the solar power generation, however, it is multiplied by a scaling factor ranging from 0.75 to 4 for each studied case. With the current setting, a scaling factor of 4 makes the peak solar generation slightly larger than the peak building load. Simulation results in Figure 2-7 demonstrate that the stochastic DSM outperforms deterministic DSM in a wide range of solar generation capacity. Relative performance in Figure 2-7 is defined as the operational cost reduction of the stochastic DSM compared to its deterministic counterpart, divided by the operational cost of stochastic

DSM. The relative performance curve shows a constantly increasing spread over the scaling factor. This is an expected result stemming from the larger uncertainty growing solar generation introduces to the system, which the deterministic DSM fails to capture. On the computational cost side, the time for the two DSMs is similar to the weekday results tabulated in Table 2-3. In terms of cost analysis, [75] reported the latest averaged solar installation costs of $4.40/W in California. Using this data, the 35 kW solar installation studied in this chapter requires an investment of more than $1.5 million. Without strong government subsidy, solar integration to the smart building is still very expensive.

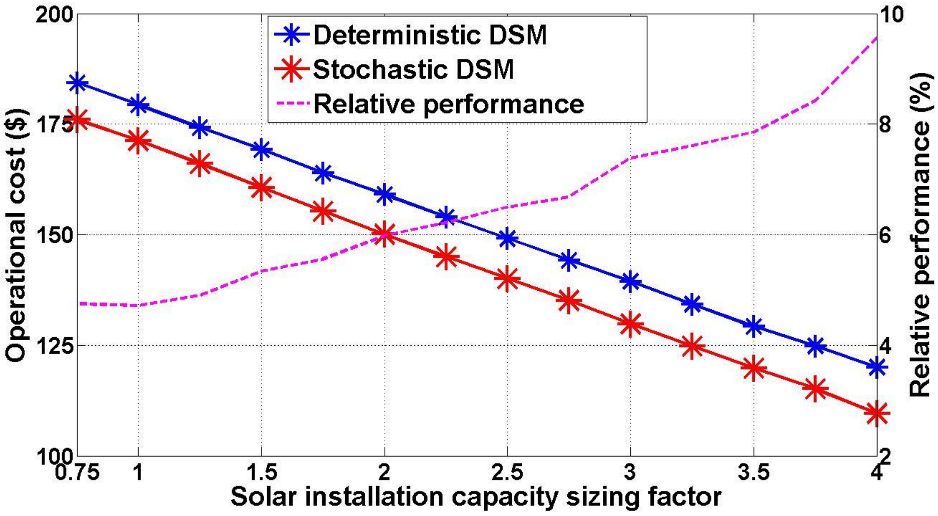

Figure 2-7 Comparisons of deterministic DSM and stochastic DSM with changing solar installation sizing

2) *Price sensitivity*. We further analyze the DSMs sensitivities when price is changed. We fixed the day-ahead price and add variations to the real-time penalty price. Table 2-4 shows the comparisons of operational cost change of both deterministic and stochastic DSM given ±25% $\boldsymbol{c}^P$ variations. There are several interesting observations: a) Compared to the 25% change in penalty price, the operational cost in either deterministic or stochastic DSM stays relatively stable. This is expected as the majority of the power supplied to the building microgrid is

from $\boldsymbol{c}^{DA}$. b) Stochastic DSM generally outperforms its deterministic counterpart, especially when the penalty price is lower than current level. The better performance with lower penalty price results from the fact that the DSM tends to buy more power from real-time penalty market when $\boldsymbol{c}^{P}$ is lower. And as DSMs buy more power from the real-time penalty market, stochastic DSM has a better estimation on power should be purchased from real-time penalty market compared to its deterministic counterpart. In general, it can be projected that in reality when $\boldsymbol{c}^{P}$ varies in a small range (less than 10%), the stochastic DSM will continue to outperform its deterministic counterpart with steady performance.

Table 2-4 Comparisons of operational cost under price variations

	75% $\boldsymbol{c}^{P}$	**100% $\boldsymbol{c}^{P}$**	**125% $\boldsymbol{c}^{P}$**
Deterministic DSM	170.98	179.44	185.99
Stochastic DSM	161.17	171.09	178.65
Improvements	9.81	8.35	7.33

3) *Impact of stationary storage*. Stationary BESS is an investment that integrates to the commercial building microgrid for cost savings. We investigate how the change in capacity and power of BESS affect the overall performance of a stochastic DSM and the preliminary results are shown in Figure 2-8. The blue asterisks show the impacts of BESS capacity changes alone where the capacity is multiplied with a sizing coefficient. The blue line is a linear regression curve fitting of the blue asterisks which shows a close match. Similarly, red asterisks show the impacts when power and capacity of BESS are sized together, and red line is its corresponding curve fitting. The slight mismatch at sizing coefficient equals to one between the blue and red asterisk is a natural result from SAA computational error. Experimental results show that cost is

cut down with BESS capacity increase, and the cost is further reduced with the help of sizing up the BESS power. However, an increase in BESS power means investing larger power inverters which will add up to the cost. Study in [76] showed that though Li-ion battery price is decreasing rapidly, it still costs \$0.55/Wh. And study in [77] reported \$0.65/W averaged cost in power electronics. Looking at the results presenting in Figure 2-8, a 100% increase in BESS capacity and power results in a 171.27-167.57= \$3.70 cost saving per day. At the current capacity and power of BESS, such an increase indicates \$64,500 additional investment in hardware only, not to mention the neglected installation and software costs. Without subsidy and other incentives, such an investment seems not fruitful.

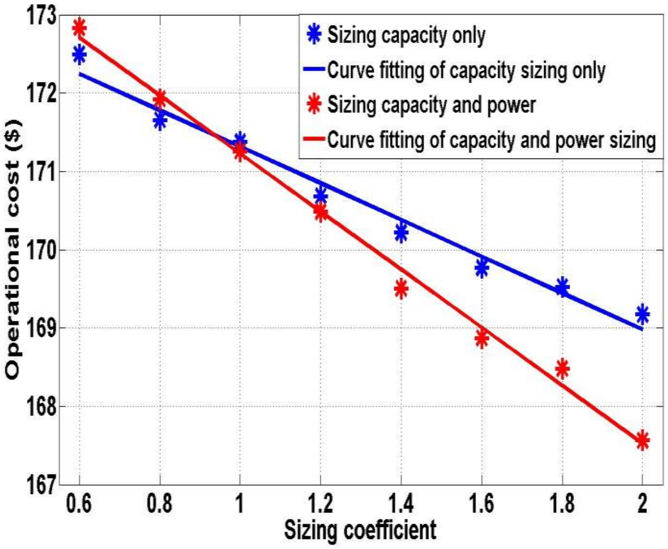

Figure 2-8 Sizing of BESS and its impacts

4) *Impact of mobile storage*. We further study the impact of change in the number of EVs on the operational cost. We duplicate the three EV profiles and create identically independent scenarios from 0 EV to 15 EVs. The computational results of the stochastic DSM are presented in Figure 2-9. We simulate a case with the original settings and a case with discharging power increased by 200%. Surprisingly, the overall operational cost first goes down with increasing number of

EVs after which the operation cost increases again. It can be explained as follow: with small number of EVs, they first help the commercial building microgrid to shave peak demands. However, as EV number continues to increase, the peak shaving cost reduction cannot compensate for the additional EV energy demands and therefore the cost rebounds. On the other hand, the cost reduction of increasing the discharging power from 2 kW to 6 kW requires an increase in power of the bidirectional off-board EV chargers. According to the $0.65/W power electronics cost reported in [77], the incremental cost of power electronics to upgrade for a 2 kW to 6 kW capacity is roughly $2,600, a number much smaller compared to the cost of increasing the capacity and power rating of BESS. Compared to BESS, the batteries in EVs do not require additional investment from the building operator, the investment in increasing EV charger power capacity seems a smarter decision. The fast increase in computational time as a result of increased EV number stems from the additional EV related decision variables and constraints. Consequently, instead of the individual EV models currently used, we may need to develop lumped EV models, to reduce the computational time when EV number is large.

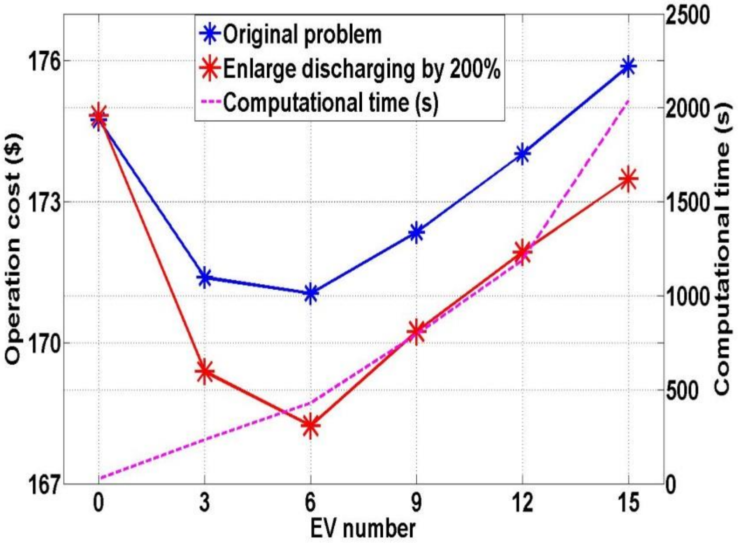

Figure 2-9 EV number variation and its impacts

2.5 Summary

Several interesting observations are made based on the case studies presented in this chapter. Firstly, the proposed stochastic DSM outperformances its deterministic counterpart for different load patterns, wide ranges of solar installation capacity and electricity prices. Although the computational time for the stochastic DSM is higher, it is still practical for the offline applications studied in this chapter. Secondly, even solar installation saves electricity bill and decrease the building's dependence on traditional centralized generations, the cost is still very expensive. Thirdly, an increase in the capacity and power of BESS generally helps to cut down the operational cost of the commercial building microgrid. However, compared to the cost reduction, the additional hardware investments do not show a good return if there are no rebate incentives. Finally, an increase in the number of EVs in a commercial building microgrid surprisingly helps to cut down the operation cost at first after which the cost starts to increase. The additional cost reduction imposed by larger discharge power helps the building manager to decide the power rating of off-board bidirectional chargers.

The numerical analysis in this chapter conforms that the moderate number of gridable EV integration is beneficial to cost reduction of commercial building microgrids. Stationary BESS as an optional energy storage system is economically expensive and part of its cost reduction functionality can be achieved by properly managed mobile storage (EVs). Furthermore, the deterministic DSM developed in this chapter is a powerful tool for building managers to further cutting down operational cost when the commercial building microgrid is integrated with solar generation and EVs. In general, the methodology used in stochastic DSM can be applied to other commercial building microgrids that integrate a variety of other storage systems and renewable generation for better management under the context of uncertainty.

A number of problems need to be studied in the future. Firstly, the lumped commercial building load used in this chapter can be decomposed into individual loads. It is projected to have a better performance at the expense of higher computational cost. Secondly, some uncertainties in the system may need to be re-examined. One example of such reevaluations is the variation in EV numbers when system continuous to scale up. Finally, when EV number continues to increase, a lumped EV model needs to be developed to avoid excessive computational time increase resulting from additionally introduced decision variables and constraints.

3 V2G Integration to Distribution Grids

In this chapter, V2G integration to distribution grids is studied. Compared with the previous chapter, the modeling and control of V2G is under the context of a connected network, i.e. distribution grids. This is an important area of study of V2G as Distribution System Operator (DSO) is generally interested in knowing the impacts of V2G integration to distribution grids.

3.1 Introduction

Facilitated by recent advances in DSM, chemical [78], thermal [79] and mechanical [80] storage systems are optimally managed in response to electricity price incentives. Combined the with the target of cutting down the overall operation cost, DSM collaboratively addresses peak shaving and power quality improvements with cyber physical constraints [81] [82].

The increasing number of EVs integrated to distribution grids introduces new challenges as well as opportunities. On one hand, unregulated charging creates sharp peaks in addition to the original load profile [83] [84]. On the other hand, with the introduction of V2G, EV switches its role from heavy load to distributed virtual generator [85] [86]. Therefore, DSM in distribution grids that jointly considers the potentials of both traditional stationary storage and EVs has been a subject of significant ongoing research.

Turning attention to the distribution grids, buses are connected by power line and interact with each other under power flow constraints. The isolated lumped model may turn out to either violate the bus voltage limits or result in excessive power losses in the power lines. Consequently, VR and Optimal Power Flow (OPF) are the two important topics capturing researchers' interests in distribution grids. A number of centralized methods have been proposed including particle swarm optimization [87], genetic algorithm [88], mixed integer non-linear programming [89], Neural Networks (NNs) [90] and fuzzy logic [91]. These methods require expensive computational power especially when the system grows large. Furthermore, when taking EV management into account, the DSM needs to know the availabilities of EVs in order to achieve the optimal performance of the system, raising privacy concerns from the EV owners [92].

When dealing with fast growing controllable distributed generations and storages in distribution grids, it is natural to apply distributed algorithms. A number of recent studies have explored the applications of distributed algorithms in DSM. [93], [94] are formulated based on dual decomposition of a convex problem formulation. However, they either treated the DSM as a lumped model or linearized the non-convex OPF problem into DC power flow model. In order to guarantee the dual decomposition converges to its original optimum, the formulation of problem has to be convex [95]. Researchers in [96] [97] [98] have taken into account the OPF problem in a distributed way, however, did not capture the uncertainties lied in the system.

In this context, this chapter presents the DSM in distribution grids under both deterministically and stochastically available resources. Battery Energy Management System (BESS) is chosen as the representative of the existing controllable load/resource that has full availability throughout the entire day. On the other hand, EVs as mobile storage devices, represent the widely existing power system uncertainties. The objective is to minimize the nodal operational cost and entire power losses in distribution grids while satisfying bus voltage and power flow constraints. Specifically, we formulate the OPF problem by convex relaxation for radial distribution grids. See [99] [100] for second-order cone programing based relaxation and [101] for semidefinite programing based relaxation. Sufficient condition for the tightness of the convex relaxation holds under three restrictions: the network has to be radial; the power injection to each bus cannot be too large; and bus voltages are kept around nominal values. These restrictions hold for most of the real-life distribution grids. On the other hand, stochastic optimization is applied to model the uncertainties in EVs, which exists in arrival time, departure time and energy demands. A model-free SAA method [69] is employed to make the stochastic modeling tractable. Furthermore, to manage the distribution grids in distributed fashion, Alternating Direction Method of Multipliers (ADMM) [95] is used to solve the problem. As the ADMM based DSM does not need to have the knowledge of end-user, their privacies are also preserved.

The technical contribution of this chapter is three-fold: 1) the proposed DSM accounts for both the nodal operational cost and OPF over the distribution network. Through tight relaxation, the original problem is further formulated into convex optimization, which can be effectively solved with solvers for guaranteed convergence.2) The uncertainties rely in EV arrival time, departure time and energy demands are modeled with stochastic programming and model-free approximation, which are later verified by real-life data collected from 19 EV users on UCLA campus over one year period. 3) An ADMM based distributed method is applied to solve for the proposed DSM. It makes the DSM scalable and end-user privacy-preserving, taking one step closer to practical industrial application. The distributed DSM is verified numerically on an IEEE 13-bus benchmark test system, followed by comprehensive discussions on the observations.

The remaining of this chapter is organized as follows: Section 3.2 introduces the formulation of the DSM problem in distribution grids. Section 3.3 develops the stochastic modeling of EVs. Subsequently, Section 3.4 explains the convex relaxation of the original problem and distributed algorithm. Numerical verifications are performed in Section 3.5 and conclusions are drawn in Section 3.6.

3.2 System Modeling

In this section, we describe the overall system architecture, and the modeling of the deterministic elements in the system, bearing the uncertainty elements in mind (in Section 3.3). The deterministic elements include DSM model, BESS model, and distribution grids model.

3.2.1 System Architecture

As shown in Figure 3-1, the studied system is in distribution grids connected to a substation at the root node. Without loss of generality, under each bus, it connects a set of BESSs, a number of EVs and uncontrollable loads. There are two major players in the distribution grids, namely DSO and Sub-Distribution System Operator (SDSO). The DSO is in charge of managing the whole distribution grids and the SDSO is managing the BESSs, EVs and loads under each bus. There exists two-way communication links between DSO and SDSO. In this chapter, we consider a slotted model and slice the timeframe of a day into H equal time slots. The time is represent as t, and $t \in \{1,2, \dots, H\}$. The set of $\{t | t \in \{1,2, \dots, H\}\}$ is denoted as $\boldsymbol{T}$**.** As the target of this chapter is to manage the distribution grids under steady-state, we assume the power flow stays the same between each time slot.

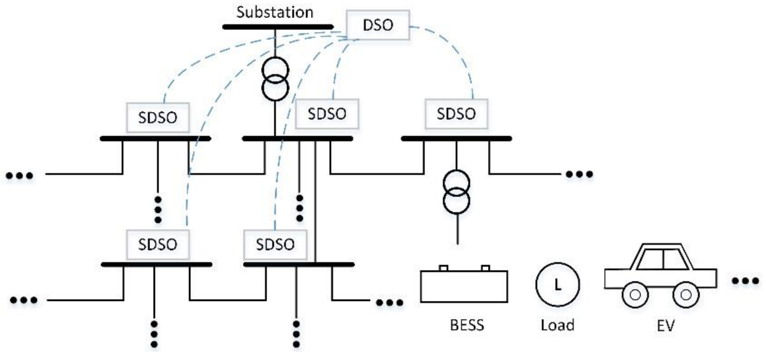

Figure 3-1 Studied distribution grids architecture

3.2.2 DSM Model

For notation: $\overline{(\cdot)}$ represents the upper limit of a scaler and similarly $\underline{(\cdot)}$ represents the lower limit. $(\cdot)^*$ stands for the conjugate of a scaler. For the same variable, capital letter is used to denote real variables, small letter is used to denote complex variables. The imaginary unit is denoted as $\boldsymbol{j}$. Other bold symbols represent sets. Finally, the expectation is denoted by $\mathbb{E}[\cdot]$.

The objective of the DSM proposed in this chapter is to minimize the overall nodal operation cost and power losses in distribution line while keeping the bus voltages regulated in the acceptable range. The distribution grids are represented as a connected graph $G = (\boldsymbol{N}, \boldsymbol{\xi})$. Let $i \in \boldsymbol{N} = \{1,2,\dots,N\}$ denote the node (bus) of the distribution grids, and $\boldsymbol{\xi}$ denote the lines. We use bus 1 to represent the root node shown in Figure 3-1. If there is a line $(i,j) \in \boldsymbol{\xi}$ connecting bus i and bus j, let $z_{ij} = R_{ij} + \boldsymbol{j}X_{ij}$ be the line impedance, and $i_{ij}(t)$ be the line current from i to j at time t, $P^i(t)$ and $Q^i(t)$ are the active and reactive power drawn at bus i at time t, and the apparent power drawn at bus $i \in \boldsymbol{N}$ is represented as $s^i(t) = P^i(t) + \boldsymbol{j}Q^i(t)$. The positive sign for $s^i(t)$ represents power drawn from bus i. For each bus i, there exists a set of BESSs, denoted $\boldsymbol{M}_b^i$, and a set of EVs, denoted $\boldsymbol{M}_e^i$. Let $\Pi(t) \in \Re^{1+}$ be the energy price for a studied day, the DSM objective function is then presented as follows:

$$\min \sum_{t} \Pi(\mathrm{t}) \sum_{i \in \boldsymbol{N} \backslash \{1\}} P^i(t) + \gamma \sum_{t=H} \sum_{(i,j) \in \boldsymbol{\xi}} R_{ij} \left| i_{ij}(t) \right|^2 \tag{3.1}$$

The DSM objective is the summation of two parts: the first part minimizes the nodal operational cost, and the second part minimizes the power losses over distribution line. The two parts are connected by a weighting factor γ. For simplicity, the time constant for each time slot is neglected, which does not affect the optimum of the system.

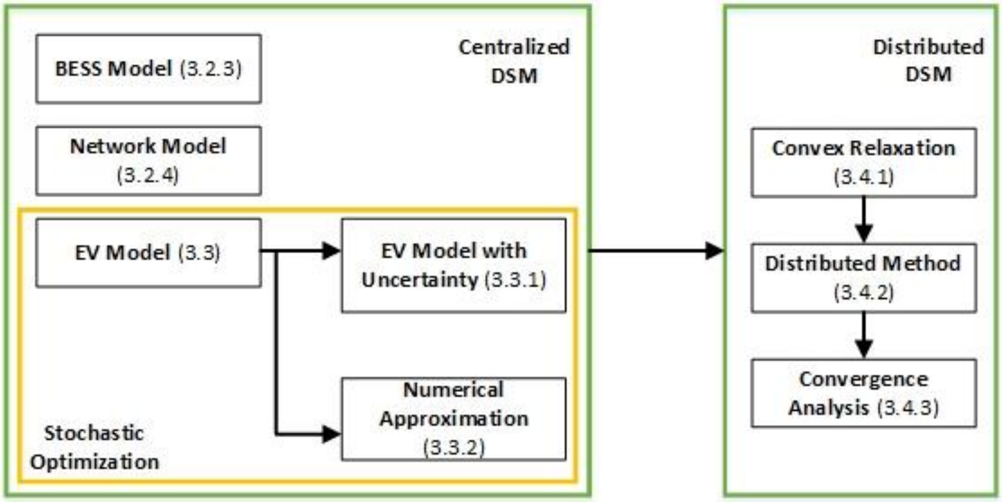

Figure 3-2 Overall architecture of the proposed DSM

We present the overall architecture of the proposed DSM in Figure 3-2. We first model the BESS and power propagation in Section 3.2.3 and 3.2.4. EVs are modeled taking into consideration of their stochastic nature. The development of EV modeling, together with PDF estimation and numerical approximation is detailed in Section 3.3, known as stochastic optimization. The combination of BESS, network and EV model becomes the centralized DSM. Its distributed counterpart is developed in Section 3.4. To ensure the convergence of distributed DSM, a tight convex relaxation is made in Section 3.4.1. Then, a distributed method is developed in Section 3.4.2 to dispatch the centralized computational burden to distributed computational nodes. The convergence and method to speed up the convergence is discussed in Section 3.4.3.

3.2.3 BESS Model

Let $P_b^{i,m}(t)$ and $Q_b^{i,m}(t)$ denote the active power and the reactive power output of the BESS m under bus i in time slot t. And $S_b^{i,m}(t)$ denote the apparent power limit of a physical inverter interfaced with the BESS. The power constraint of the BESS for $\forall i \in \boldsymbol{N}\backslash\{1\}, \forall m \in \boldsymbol{M}_b^i$ can be represented as follows:

$$P_b^{i,m^2}(t) + Q_b^{i,m^2}(t) \leq S_b^{i,m^2}(t) \tag{3.2.a}$$

This constraint models the maximum power rating of an inverter. The energy constraint of the BESS for $\forall i \in \boldsymbol{N}\backslash\{1\}, \forall m \in \boldsymbol{M}_b^i$ is modeled as:

$$\underline{E_b^{i,m}} \leq ES_b^{i,m} + \sum_{t \in \boldsymbol{T}} P_b^{i,m}(t) \leq \overline{E_b^{i,m}} \tag{3.2.b}$$

where $ES_b^{i,m}$ represents the initial State-of-Energy (SoE) of the BESS m under bus i at time $t = 0$. $\overline{E_b^{i,m}}$ and $\underline{E_b^{i,m}}$ represent the upper and lower limit of the BESS, respectively. The lower bound for is a positive real scaler to prevent the BESS from deep discharge, which is known to exponentially decrease the lifespan of a battery [102]. After a full day's operation, we would like the SoE of BESS for $\forall i \in \boldsymbol{N}\backslash\{1\}, \forall m \in \boldsymbol{M}_b^i$ to be some pre-defined final value:

$$ES_b^{i,m} + \sum_{t=H} P_b^{i,m}(t) = EF_b^{i,m} \tag{3.2.c}$$

where $EF_b^{i,m}$ is the final SoE of the BESS after a full day's operation.

3.2.4 Network Model

Following the notation in Section 3.2.2 and 3.2.3, for $\forall(i,j) \in \boldsymbol{\xi}, j \neq 1$ we can derive the power flow of the distribution grids using the following equations:

$$v_i(t) - v_j(t) = z_{ij} i_{ij}(t) \tag{3.3.a}$$

$$s_{ij}(t) = v_i(t) i_{ij}^*(t) \tag{3.3.b}$$

$$s_{ij}(t) - z_{ij}\left|i_{ij}(t)\right|^2 - \sum_{(j,k) \in \xi} s_{jk}(t) = s_j(t) \tag{3.3.c}$$

where the bus *i* voltage is denoted as v_i, and $s_{ij}(t) = P_{ij}(t) + \boldsymbol{j} Q_{ij}(t)$ denote the apparent power flowing from bus *i* to bus j. The positive sign for s_{ij} is defined as power flowing from *i* to j.

Eq.3.3.a is the Ohm's law, Eq.3.3.b and Eq.3.3.c are the definitions for apparent power and power flow, respectively. Substituting Eq.3.3.a and Eq.3.3.b into Eq.3.3.c we will have for $\forall (i,j) \in \boldsymbol{\xi}, j \neq 1$:

$$P^j(t) = P_{ij}(t) - R_{ij}\left|i_{ij}(t)\right|^2 - \sum_{(j,k)\in\xi} P_{jk}(t) \tag{3.4.a}$$

$$Q^j(t) = Q_{ij}(t) - X_{ij}\left|i_{ij}(t)\right|^2 - \sum_{(j,k)\in\xi} Q_{jk}(t) \tag{3.4.b}$$

$$|v_i(t)|^2 - \left|v_j(t)\right|^2 = 2\left(R_{ij}P_{ij}(t) + X_{ij}Q_{ij}(t)\right) - (R_{ij}^2 + X_{ij}^2)\left|i_{ij}(t)\right|^2 \tag{3.4.c}$$

$$|v_i(t)|^2\left|i_{ij}(t)\right|^2 = P_{ij}^2(t) + Q_{ij}^2(t) \tag{3.4.d}$$

Eq.3.4.a-Eq.3.4.d define the power flow of the distribution grids. In an attempt to model VR, we put the following constraints at each buses:

$$\underline{V} \leq |v_i| \leq \overline{V}, \forall i \in \boldsymbol{N} \backslash \{1\}; |v_1| = V_c \tag{3.5.a}$$

$\underline{V}$ and $\overline{V}$ are the lower and upper voltage magnitude limits. The bus voltage at root node 1 is assumed to be constant V_c, which results from the fact that it is connected to the transmission system and be modeled as an infinite bus. The active and reactive power drawn at the root node is defined as:

$$P^1(t) = \sum_{j:(1,j)\in\xi} P_{1j}(t) \tag{3.5.b}$$

$$Q^1(t) = \sum_{j:(1,j)\in\xi} Q_{1j}(t) \tag{3.5.c}$$

Putting additional physical capacity constraints on the rating of the substation we have:

$$|P^1(t) + jQ^1(t)| \leq \overline{S^1} \tag{3.5.d}$$

The power under each bus for $\forall i \in \boldsymbol{N} \backslash \{1\}$ is defined as follows:

$$P^i(t) = P_l^i(t) + \sum_{m \in \boldsymbol{M}_e^i} P_b^{i,m}(t) + \mathbb{E}[\sum_{m \in \boldsymbol{M}_e^i} P_e^{i,m}(\delta^{i,m}, \nu^{i,m}, \chi^{i,m}, t)] \tag{3.5.e}$$

$$Q^i(t) = Q_l^i(t) + \sum_{m \in M_e^i} Q_b^{i,m}(t) + \mathbb{E}[\sum_{m \in M_e^i} Q_e^{i,m}(\delta^{i,m}, \nu^{i,m}, \chi^{i,m}, t)] \tag{3.5.f}$$

where $P_l^i(t)$ and $Q_l^i(t)$ are the active and reactive power uncontrollable load at time t. $P_e^{i,m}(t)$ and $Q_e^{i,m}(t)$ are the active and reactive power EV m under bus i absorbs. $\delta^{i,m}, \nu^{i,m}, \chi^{i,m}$ denote the uncertainties in the EV arrival time, departure time and energy demand, respectively. $\mathbb{E}[\cdot]$ denotes the expectation. The value of $P_e^{i,m}$ and $Q_e^{i,m}$ are subject to the uncertainty in EV. We will develop the EV model in the following section, showing how the uncertainties are modeled in EVs.

3.3 Stochastic EV Modeling

In this section, we have a slightly different model of EVs. The charging and discharging current of EVs are no longer discrete. The reasoning behind it is to formulate the problem into convex optimization.

3.3.1 EV model

One major difference between EV and BESS is the uncertainties in EV's availability and energy demand. An EV owner may arrive at parking facility at random time. Similarly, very likely the owner will not be committed to any schedule without additional incentives, therefore may leave at random time. In addition to the uncertain in availability, the energy demand of an EV highly depends on the travel distance of the owner. All these factors add up to the difficulty of DSM with EV integrations. Let $\underline{P_e^{i,m}}$ and $\overline{P_e^{i,m}}$ be the maximum discharge power and charging power of

EV i under bus m, with $\underline{P_e^{i,m}} \in \Re^{1-}$ representing the effect of V2G. For each $\forall i \in \boldsymbol{N} \backslash \{1\}, \forall m \in \boldsymbol{M}_e^i$, we have power constrains:

$$\underline{P_e^{i,m}} A_e^{i,m}(\delta^{i,m}, \nu^{i,m}, t) \leq \ P_e^{i,m}(t) \leq \overline{P_e^{i,m}} A_e^{i,m}(\delta^{i,m}, \nu^{i,m}, t) \tag{3.6.a}$$

where $A_e^{i,m}(\delta^{i,m}, \nu^{i,m}, t) \in \Re^1$ stands for the availability of EV i under bus m at time t. $\delta^{i,m}$ and $\nu^{i,m}$ stand for the uncertainty in EV availability. The reactive power of EV bidirectional charging is not considered. The reasons behind this modeling is, in practice, EV bidirectional chargers usually has much smaller power ratings compared to BESS, making the converter more economic at the price of two-quadrant controllability [39]. So we modeled it as a constant power factor load. $A_e^{i,m}(\delta^{i,m}, \nu^{i,m}, t)$ is defined as

$$A_e^{i,m}(\delta^{i,m}, \nu^{i,m}, t) = \begin{cases} 1, & EV\ i\ available\ at\ t \\ 0, & otherwise \end{cases} \tag{3.6.b}$$

For each $\forall i \in \boldsymbol{N} \backslash \{1\}, \forall m \in \boldsymbol{M}_e^i$, the energy constraints, we have:

$$\underline{E_e^{i,m}} \leq ES_{e,t_s}^{i,m}(\chi^{i,m}) + \sum_{t=\,t_a^{i,m}}^{t \in \boldsymbol{T}_{i,m}} A_{\mathrm{e}}^{i,m}(\delta^{i,m}, \nu^{i,m}, t) P_e^{i,m}(t) \leq \overline{E_e^{i,m}} \tag{3.6.c}$$

$\underline{E_e^{i,m}}$ and $\overline{E_e^{i,m}}$ are the battery capacity limits of the EVs. $t_a^{i,m}$ denotes the arrival time of EV m and $\boldsymbol{T}_{i,m}$is the set of time slots that EV m is available. The initial SoE is represented as $ES_e^{i,m}$. $\chi^{i,m}$ is used to show the uncertainty in initial SoE of the EV. Similar to BESS modeling $\underline{E_e^{i,m}}$ is set to prevent deep discharge of the battery.

Finally, we will have the energy constraints after the whole day's operation valid for $\forall i \in \boldsymbol{N} \backslash \{1\}, \forall m \in \boldsymbol{M}_e^i$ as:

$$ES_e^{i,m}(\chi^{i,m}) + \sum_{t=t_l^{i,m}} A_e^{i,m}(\delta^{i,m}, \nu^{i,m}, t) P_e^{i,m}(t) = EF_e^{i,m}(\chi^{i,m}) \tag{3.6.d}$$

$EF_e^{i,m}$ stands for the final SoE of the EV and $t = t_l^{i,m}$ stands for the leave time of EV m. It is clear that for an arbitrary distribution of random variables $\delta^{i,m}, \nu^{i,m}, \chi^{i,m}$, it is difficult to represent Eq.3.5.e-Eq.3.5.f, Eq.3.6.a-Eq.3.6.d analytically, making even more drag when solving the entire DSM. We need to use the SAA and KDE method described in the previous chapter, to make the problem formulation numerically tractable.

3.3.2 Numerical Approximation

Following the same methodology as the previous chapter, we present the modeling of EV using SAA and KDE in this section without deduction. An efficient approximation of Eq.3.5.e-Eq.3.5.f are offered by generating NS *i.i.d.* samples of $\boldsymbol{\psi} = \{\delta_s^{i,m}, \nu_s^{i,m}, \chi_s^{i,m}\}_{s=1}^{NS}$:

$$P^i(t) = P_l^i(t) + \sum_{m \in \boldsymbol{M}_b^i} P_b^{i,m}(t) + \frac{1}{NS} \sum_{s \in \boldsymbol{\psi}} \sum_{m \in \boldsymbol{M}_e^i} P_{e,s}^{i,m}(t) \tag{3.7.a}$$

$$Q^i(t) = Q_l^i(t) + \sum_{m \in \boldsymbol{M}_b^i} Q_b^{i,m}(t) + \frac{1}{NS} \sum_{s \in \boldsymbol{\psi}} \sum_{m \in \boldsymbol{M}_e^i} Q_{e,s}^{i,m}(t) \tag{3.7.b}$$

where we use a subscript s for each random variable to denote the generated scenario. The assumption here is $\delta_s^{i,m}, \nu_s^{i,m}, \chi_s^{i,m}$ are i.i.d, we will justify this assumption in the studied case Section 3.5. Accordingly, for each generated scenario $s \in \boldsymbol{\psi}$, the constraints for EV should still hold for each generated scenario. Therefore, Eq.3.6.a-Eq.3.6.d are updated as the following:

$$\underline{P_e^{i,m}} A_{e,s}^{i,m}(t) \leq P_{e,s}^{i,m}(t) \leq \overline{P_e^{i,m}} A_{e,s}^{i,m}(t) \tag{3.8.a}$$

$$A_{e,s}^{i,m}(t) = \begin{cases} 1, & EV\ i\ available\ at\ t\ in\ s \\ 0, & otherwise \end{cases} \tag{3.8.b}$$

$$\underline{E_e^{i,m}} \le ES_{e,s}^{i,m} + \sum_{t=t_{a,s}^{i,m}}^{t\in \boldsymbol{T}_{i,m}^{s}} \mathrm{A}_{\mathrm{e,s}}^{i,m}(t) P_{e,s}^{i,m}(t) \le \overline{E_e^{i,m}} \tag{3.8.c}$$

$$ES_{e,s}^{i,m} + \sum_{t=t_{l,s}^{i,m}} A_{\mathrm{e}}^{i,m}(t) P_{e}^{i,m}(t) = EF_{e,s}^{i,m} \tag{3.8.d}$$

where following the naming convention, $t_{a,s}^{i,m}$ and $t_{l,s}^{i,m}$ respectively stands for the arrival and leave time of EV m in scenario *s*. Similarly, $\boldsymbol{T}_{i,m}^{s}$is the set of time slots that EV m is available in scenario *s*. Note the above constraints hold for $\forall s \in \boldsymbol{\psi}, \forall i \in \boldsymbol{N}\backslash\{1\}, \forall m \in \boldsymbol{M}_e^i$. We also describe how to capture the distribution of the uncertainty variables, i.e. $\delta^{i,m}, \nu^{i,m}, \chi^{i,m},$ in Section 3.5. After the SAA numerical approximation, the optimization problem is tractable. We define the decision variable set to be $\boldsymbol{\Omega} = \{P^i(t), Q^i(t), P_b^{i,m}(t), Q_b^{i,m}(t), P_{e,s}^{i,m}(t), Q_{e,s}^{i,m}(t) | t \in \boldsymbol{T}\}$. The DSM problem now can be presented as:

$$\min_{\boldsymbol{\Omega}} \sum_{t} \Pi(\mathrm{t}) \sum_{i\in \boldsymbol{N}\backslash\{1\}} P^i(t) + \gamma \sum_{t=H} \sum_{(i,j)\in \xi} R_{ij} \left| i_{ij}(t) \right|^2$$

$$subject\ to. (3.2), (3.4), (3.5.a) - (3.5.d), (3.7), (3.8)$$

However, Eq.3.4.d is non-convex, making the problem impossible to solve with convex optimization solvers. Non-convex solvers require much stronger computational power and the solutions are not guaranteed to be global optimum. As a result, we seek to convexify the DSM problem and solve it in a distributed manner using ADMM in the following section.

3.4 Distributed Optimization

In this chapter, we target to develop a scalable and privacy-preserving DSM. To this end, we use a distributed algorithm ADMM to distribute centralized computational burden of DSO to each SDSO. The distributed algorithm also protects the end-user's privacy by getting only the "aggregated" information under a bus. To guarantee convergence, we relax the original non-convex problem and show conditions for a tight relaxation.

3.4.1 Convex Relaxation

According to [100] and [99], the non-convexity constraint in Eq.3.4.d can be relaxed to a convex second-order cone as follows:

$$|v_i(t)|^2 \left|i_{ij}(t)\right|^2 \geq P_{ij}^2(t) + Q_{ij}^2(t), \forall (i,j) \in \boldsymbol{\xi}, j \neq 1 \tag{3.9}$$

For a tight relaxation, there are three sufficient conditions, namely (a) the network has to be radial; (b) the power injection to each bus cannot be too large; and (c) bus voltages are kept around nominal values. The method to check the exactness of a relaxation is to solve for Eq.3.9 and compare the left-hand-side in the equality to the right-hand-side. We define the decision variable set to be $\boldsymbol{\Omega} = \{P^i(t), Q^i(t), P_b^{i,m}(t), Q_b^{i,m}(t), P_{e,s}^{i,m}(t), Q_{e,s}^{i,m}(t) | t \in \boldsymbol{T}\}$. With the convex relaxation, the relaxed DSM can be described as follows:

$$\min_{\boldsymbol{\Omega}} \sum_t \Pi(\mathrm{t}) \sum_{i \in \boldsymbol{N} \setminus \{1\}} P^i(t) + \gamma \sum_{t=H} \sum_{(i,j) \in \boldsymbol{\xi}} R_{ij} \left|i_{ij}(t)\right|^2$$

$$subject\ to\ (3.2), (3.4.a) - (3.4.c), (3.5.a) - (3.5.d), (3.7) - (3.9)$$

Given a tight convex relaxation, the DSM is in a centralized manner and therefore the DSO still has to collect the information on each buses, raising privacy concerns to EV owners. Furthermore, with a growing size of BESSs, EVs and perhaps other controllable devices not included in this chapter, the DSO has a heavy computational burden for the system to scale up. These motivates us to develop a distributed DSM that is scalable and privacy-preserving.

3.4.2 Distributed Algorithm

We develop the distributed DSM using the ADMM method. We first give a brief introduction to ADMM. The ADMM solves problems in the following form:

$$\begin{gathered} min\ \ f(x) + g(z) \\ subject\ to\ Ax + Bz = c \end{gathered}$$

where $x \in \Re^n$ and $z \in \Re^m$ are decision variables. $A \in \Re^{p\times n}$, $B \in \Re^{p\times m}$ and $c \in \Re^p$. Assuming $f(\cdot)$ and $g(\cdot)$ are convex and constraints form convex set. The augmented Lagrangian of this problem is presented as:

$$L_\rho(x, z, y) = f(x) + g(z) + y(Ax + Bz - c) + \frac{\rho}{2}||Ax + Bz - c||^2$$

Choosing a random initial value for x, z and y, ADMM is then formulated as the following iterations:

$$(x)_{k+1} = argmin_x\ L_\rho(x, (z)_k, (y)_k)$$

$$(z)_{k+1} = argmin_y\ L_\rho((x)_{k+1}, z, (y)_k)$$

$$(y)_{k+1} = (y)_k + \rho(A(x)_{k+1} + B(z)_{k+1} - c)$$

where ρ is a positive number stands for step size. Through the sequential update of x and z the searching direction of the optimum is alternating. Substituting $y = \rho u$, we derive the scaler form for the ADMM as following iterations:

$$(x)_{k+1} = argmin_x\ \left(f(x) + \frac{\rho}{2}\left||Ax + B(z)_{k+1} - c + (u)_k\right||^2\right)$$

$$(z)_{k+1} = argmin_z\ \left(g(z) + \frac{\rho}{2}\left||A(x)_{k+1} + Bz - c + (u)_k\right||^2\right)$$

$$(u)_{k+1} = (u)_k + A(x)_{k+1} + B(z)_{k+1} - c$$

The iteration stops until it converges. If the $f(\cdot)$ and $g(\cdot)$ are convex and constraints form convex set, the distributed solution is guaranteed to converge to the centralized counterpart.

The key for ADMM is for a convex problem can be decomposed into global and local sub-problems. The ADMM method actually turns out to be natural fit to DSM problem in this chapter. We decompose the original DSM problem into a global problem that solves for the OPF and VR at DSO, and local problems that solve for energy cost minimization at SDSOs.

Before start of the ADMM iterations, we first initialize the problem with random numbers: for the first iteration, DSO sets random values to P^i and Q^i, for $\forall i \in \boldsymbol{N}\backslash\{1\}$. For simplicity of notation, we neglect *time t* in each variable. We introduce two sets of dual variables for each bus $i \in \boldsymbol{N}\backslash\{1\}$, namely $\alpha_i(t) \in \Re^1$ and $\beta_i(t) \in \Re^1$.And SDSO randomly choose $P_b^{m,i}$, $Q_b^{m,i}$ for $\forall i \in \boldsymbol{N}\backslash\{1\}, \forall m \in \boldsymbol{M}_b^i$, and $P_{e,s}^{m,i}$ and $Q_{e,s}^{m,i}$ for $\forall s \in \boldsymbol{\psi}, \forall i \in \boldsymbol{N}\backslash\{1\}, \forall m \in \boldsymbol{M}_e^i$.

Define $\boldsymbol{\Omega}_1 = \{P_b^{i,m}(t), Q_b^{i,m}(t), P_{e,s}^{i,m}(t), Q_{e,s}^{i,m}(t) | t \in \boldsymbol{T}\}$For each iteration $k+1$, the SDSO at bus $i \in \boldsymbol{N}\backslash\{1\}$, get the iteration k update $(P^i)_k$, $(Q^i)_k$, $(\alpha_i)_k$ and $(\beta_i)_k$ from SDO and first solve a local DSM problem based on iteration k as follows:

$$\begin{gathered}
\min_{\boldsymbol{\Omega}_1} \sum_t \Pi(\mathrm{t}) \sum_{i \in \boldsymbol{N}\backslash\{1\}} P^i(t) \\
+\frac{\rho_1}{2} \sum_{t=H} (-\left(P^i(t)\right)_k + P_l^i(t) + \sum_{m \in \boldsymbol{M}_b^i} P_b^{i,m}(t) + \frac{1}{NS} \sum_{s \in \boldsymbol{\psi}} \sum_{m \in \boldsymbol{M}_e^i} P_{e,s}^{i,m}(t) + (\alpha_i(t))_k\ )^2 \\
+\frac{\rho_2}{2} \sum_{t=H} (-\left(Q^i(t)\right)_k + Q_l^i(t) + \sum_{m \in \boldsymbol{M}_b^i} Q_b^{i,m}(t) + \frac{1}{NS} \sum_{s \in \boldsymbol{\psi}} \sum_{m \in \boldsymbol{M}_e^i} Q_{e,s}^{i,m}\ (t) + (\beta_i(t))_k\ )^2 \\
subject\ to\ (3.2), (3.8)
\end{gathered} \tag{3.10}$$

where ρ_1, ρ_2 are the step size. The local DSM at each bus solve for the optimal schedule for BESS and EV in iteration $k+1$, denoted as $(P_b^{i,m})_{k+1}$, $(P_{e,s}^{i,m})_{k+1}$, $(Q_b^{i,m})_{k+1}$ and $(Q_{e,s}^{i,m})_{k+1}$. Then the SDSO communicate the aggregated bus load $(P_a^i)_{k+1}$ and $(Q_a^i)_{k+1}$ defined as follows to DSO.:

$$(P_a^i)_{k+1} = P_l^i(t) + \sum_{m\in \boldsymbol{M}_b^i} (P_b^{i,m}(t))_{k+1} + \frac{1}{NS}\sum_{s\in\boldsymbol{\psi}}\sum_{m\in \boldsymbol{M}_e^i} (P_{e,s}^{i,m}(t))_{k+1}$$

$$(Q_a^i)_{k+1} = Q_l^i(t) + \sum_{m\in \boldsymbol{M}_b^i} (Q_b^{i,m}(t))_{k+1} + \frac{1}{NS}\sum_{s\in\boldsymbol{\psi}}\sum_{m\in \boldsymbol{M}_e^i} (Q_{e,s}^{i,m}(t))_{k+1}$$

After receiving all the information for iteration $k+1$ from SDSO, DSO solve a global DSM problem by every time step as follows:

$$\min_{P^i(t),Q^i(t)} \gamma \sum_{(i,j)\in\boldsymbol{\xi}} R_{ij}\left|i_{ij}(t)\right|^2 + \frac{\rho_1}{2}\sum_{i\in\boldsymbol{N}\backslash\{1\}} (-P^i(t) + (P_a^i(t))_{k+1} + \left(\alpha_i(t)\right)_k)^2$$
$$+\frac{\rho_2}{2}\sum_{i\in\boldsymbol{N}\backslash\{1\}} (-Q^i(t) + (Q_a^i(t))_{k+1} + \left(\beta_i(t)\right)_k)^2$$

$$subject\ to\ (3.4.a) - (3.4.c), (3.5.a) - (3.5.d), (3.9)$$

(3.11)

In this dissertation, the decomposition of the problem is based on the aggregated active and reactive load. In ADMM, the centralized problem can be made distributed if the two sets of decision variables are constrained by an equality constraint *Ax+Bz=c*. This decomposition does not hold in general for all power system optimization problems, however, the proposed method could be applied in scenarios where the overall objective function is composed of a sum of local costs, and a global cost. After solving for each time step of a day, the global DSM, the DSO updates the two sets of dual variables for each bus $i \in N\backslash\{1\}$ as follows:

$$(\alpha_i(t))_{k+1} = (\alpha_i(t))_k - (P^i(t))_{k+1} + (P_a^i(t))_{k+1} \tag{3.12.a}$$

$$(\beta_i(t))_{k+1} = (\beta_i(t)\,)_k - (Q^i(t))_{k+1} + (Q_a^i(t))_{k+1} \tag{3.12.b}$$

The updates of the dual variables signals the end of iteration $k+1$. The updated $(P^i)_{k+1}$, $(Q^i)_{k+1}$, $(\alpha_i)_{k+1}$ and $(\beta_i)_{k+1}$ are broadcasted to each SDSO for the next iteration. The iteration ends when the problem converges (discussed in Section 3.4.3). The ADMM based algorithm can distribute the computational burden at the DSO to SDSO. At the same time, for each iteration, the DSO only has to know the aggregated load at each bus, preserving the privacy by hiding the individual information in the aggregated information.

3.4.3 Convergence and Over Relaxation

It has been proved in [95] that if the centralized problem is convex, the ADMM is to converge to the same optimum with tolerable errors. For the proposed ADMM based DSM, the stopping criteria is when the distributed algorithm converges. Define the primal residuals of the two dual variables at iteration k for each bus i to be:

$$r_p^i = \sum_{t=H} (-(P^i(t))_k + (P_a^i(t))_k)^{\mathbf{2}} \tag{3.13.a}$$

$$r_q^i = \sum_{t=H} (-(Q^i(t))_k + (Q_a^i(t))_k)^{\mathbf{2}} \tag{3.13.b}$$

The stopping criteria for the distributed DSM is to make sure the two primal residuals to be sufficiently small:

$$r_p^i \le \epsilon, r_q^i \le \epsilon, \forall i \in \boldsymbol{N} \backslash \{1\} \tag{3.13.c}$$

where ϵ is a predefined error boundary. The summary of the ADMM based distributed DSM is tabulated in Algorithm 3.1.

Algorithm 3.1. ADMM based distributed DSM

```
1: Initialize the problem. Set $k = 1$. DSO randomly choose $P^i$, $Q^i, \alpha_i$ and $\beta_i$*. SDSO at bus $i$ randomly choose $P_b^{m,i}$, $Q_b^{m,i}$, and $P_{e,s}^{m,i}$ and $Q_{e,s}^{m,i}$.
2: Repeat for $k = 2,3,\ldots$
3:     Solve the local DSM in (3.10) at each SDSO using $(P^i)_k$, $(Q^i)_k$, $(\alpha_i)_k$ and $(\beta_i)_k$ broadcasted by DSO
4:     Solve the global DSM in (3.11) at DSO by collecting $(P_a^i)_{k+1}$ and $(Q_a^i)_{k+1}$ from each SDSO
5:     Update dual variables in (3.12) and broadcast $(P^i)_{k+1}$, $(Q^i)_{k+1}$, $(\alpha_i)_{k+1}$ and $(\beta_i)_{k+1}$
6: Until convergence in (3.13)
```

* for simplicity of notation, time t is neglected for each variable

To accelerate the convergence speed, an over relaxation technique is proposed in [103]. Basically, it is to substitute the $(P_a^i)_{k+1}$ and $(Q_a^i)_{k+1}$ in each iteration $k + 1$ (line 5 in Algorithm 3.1) as follows:

$$(P_a^i(t))_{k+1} = \theta(P_a^i(t))_{k+1} - (1-\theta)(-(P^i(t))_k) \tag{3.14.a}$$

$$(Q_a^i(t))_{k+1} = \theta(Q_a^i(t))_{k+1} - (1-\theta)(-(Q^i(t))_k) \tag{3.14.b}$$

where θ is a relaxation parameter. [103] suggested that $\theta \in [1.5,1.8]$ can improve the convergence speed. We will provide numerical verifications and comparisons to the original ADMM based DSM in the following section.

3.5 Results and Analysis

This section demonstrates the correctness of the proposed DSM and its performance. We first introduce the simulation setup. It is followed by case studies to verify the correctness, and extensive discussions on understanding the numerical results.

3.5.1 Simulation Setup

We use a modified IEEE 13-bus radial test feeders [104] for demonstration of the proposed DSM. As the primary focus of this chapter is not on dynamics or electromagnetic transient, we made some minor modification to the original IEEE 13-bus radial test feeders to study the steady-state DSM: the in-line transformer between bus 633 and 634 is removed; the breaker between bus 671 and 692 is closed. Because of the extreme short line length between bus 633 and 634, the two buses are treated as one single bus, i.e. bus 5 in Figure 3-3. For similar reason, bus 692 and 675 are treated as bus 9 in Figure 3-3. The root node is a 115 kV substation and it is connected with an 115 kV/4.16 kV transformer. We do not consider the three-phase imbalance in the distribution system, the three-phase diagram is therefore drawn as a one-line diagram. At each distribution bus, it is connected to several 4.16 kV/0.12 kV distribution transformers. The transformers are directly connected to the load, BESSs and EVs.

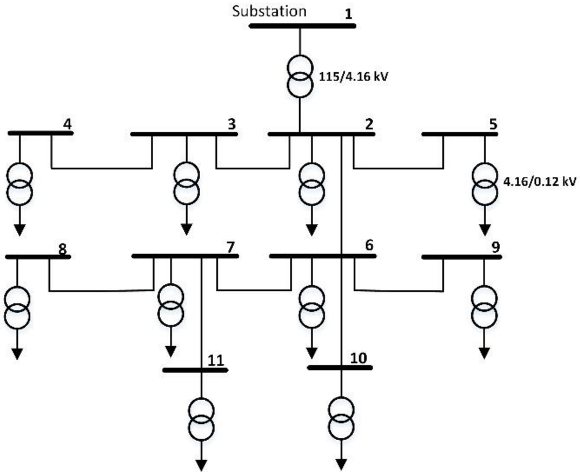

Figure 3-3 Modified IEEE 13-bus radial test feeders

The DSM studied in this chapter uses one hour as time step. We use the day-ahead price from [105], which is shown in Figure 3-4. Fixed load profile at each bus is obtained from [106] and plotted in Figure 3-5. We place one BESS at each buses in Figure 3-3 except for the root bus. The key parameters of three studied types of batteries are documented in Table 3-1.

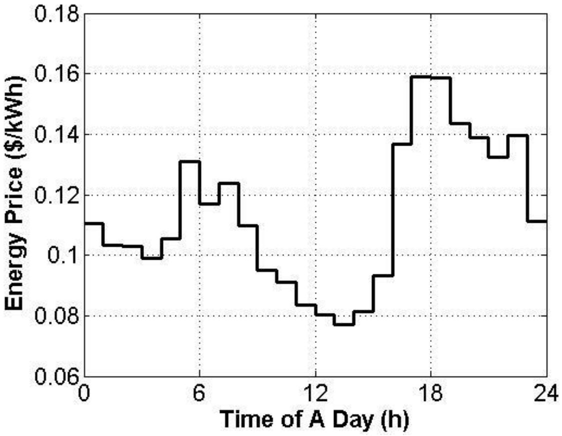

Figure 3-4 Day-ahead price

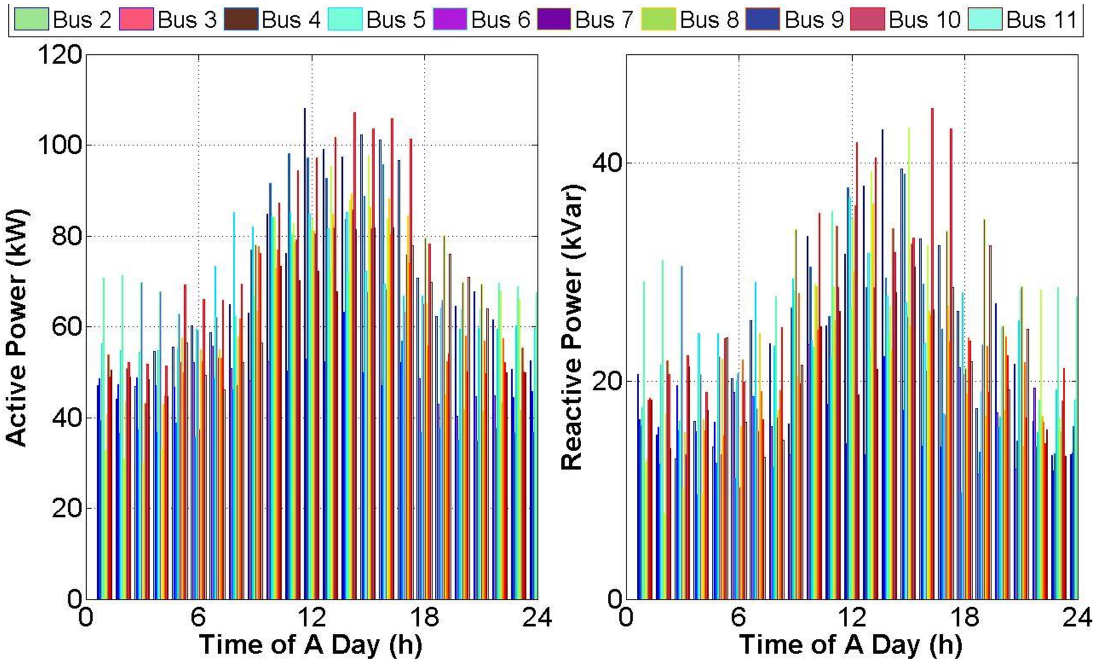

Figure 3-5 A typical day load pattern

We collected 19 EV driver's records for a whole year on UCLA campus in order to accomplish this study. The recorded EVs fall into three popular models in the market, i.e. Nissan Leaf, Tesla Model S and Mitsubishi MiEV. Their arrival time, leaving time, and energy demands are recorded for generating a close to real-life study. Apart from filtering out data with communication failures, we made the following assumptions to the original data in order to verify the proposed DSM: 1) *V2G capability*. Very few charging stations supports V2G nowadays, partly resulting from different interfacing protocols, see two different protocols used in the three mentioned EV models in [107] and [64]. The records we have collected are EV charging data, however, it reveals the V2G potential: An EV is usually fully charged before it is unplugged and therefore can perform V2G in spare time. Following this reasoning, we assume EVs are V2G capable once connected to the grid, however they need to meet their energy demands before leave. 2) *SoE acquisition*. The SoE data is also hard to obtain and therefore it is impossible to tell the starting SoE after EV connects. As we have data in EV energy demands, we will assume EVs get fully charged every time. In this way, it will be tractable to calculate the starting SoE using the collected energy demands data. Table 3-1 summarizes the key parameters used for three different EV models and BESS models in this chapter. Table 3-2 summarizes the key parameters used for distribution network simulation. All EV related parameters comes from real-life EV manufacturers. BESS related parameters are chosen as these are the typical size of the BESS in distribution systems. And finally, distribution network related parameters are from IEEE benchmark test system and real-life regulations in U.S power systems.

Table 3-1 Key Parameters Used for BESS and EV

Device	Power Rating (Min, Max)	Capacity
Type A BESS	[-20,20] kVA	25 kWh
Type B BESS	[-15,15] kVA	20 kWh
Type C BESS	[-10,10] kVA	15 kWh
Tesla Model S	[-3.3,6.6] kW	65 kWh

Nissan Leaf	[-3.3,6.6] kW	24 kWh
Mitsubishi MiEV	[-3.3,6.6] kW	16 kWh

Table 3-2 Key Parameters Used for Distribution Networks

Parameters	**Rating**
Voltage Magnitude Limit	[0.95 1.05] p.u.
Substation Power Limit	5 MVA
Substation Secondary Voltage	4.16 kV

In observance of the large number of EV owners, we only show three EV owner profiles in Figure 3-6 as the representatives of the 19 EV owners. The three owners drive a Tesla Model S, Nissan Leaf and Mitsubishi MiEV respectively. We capture the distribution of the real-life data using KDE described in Section 2.3.3. Figure 3-6 compares the real-life data and distribution generated by KDE, showing a close match between the two. The KDE is then applied to generate the scenarios in SAA. We duplicate 1 out of the 19 EVs to make the total EV number 20, and we evenly distribute the two EVs at each distribution bus except for the root node. For the distributed DSM, We set weighting factor $\gamma = 1$, step size $\rho_1 = 1, \rho_2 = 2$ and predefined error boundary $\epsilon = 10^{-3}$. The over relaxation parameter is set to $\theta = 1.75$. The proposed DSMs are solved with Gurobi on a PC with 2.67GHz CPU and 8 GB RAM.

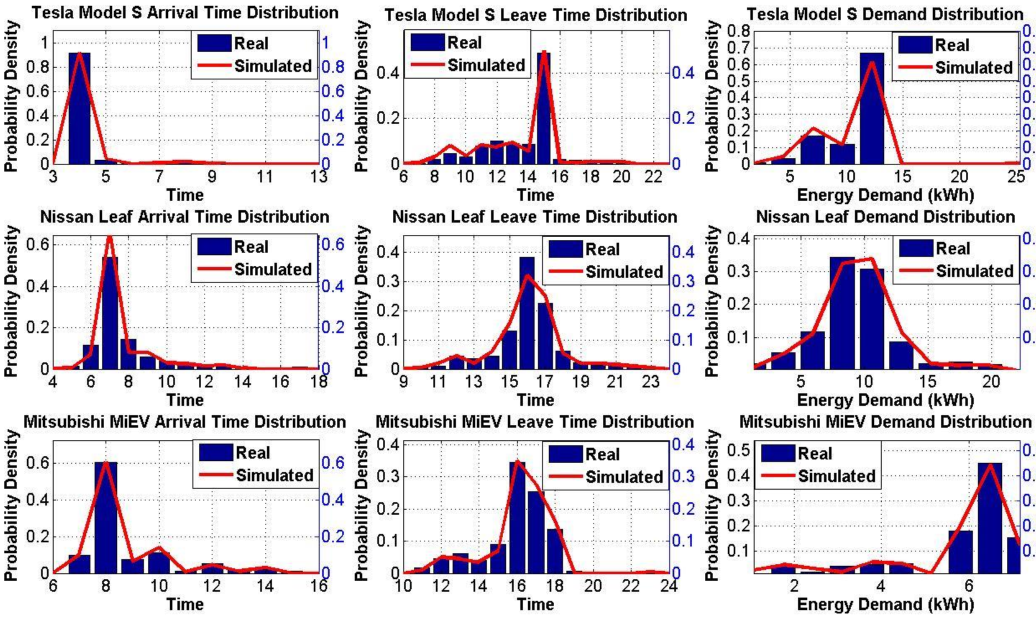

Figure 3-6 Three typical patterns of EV users

3.5.2 Case Study

We generate 200 scenarios using the SAA and the convergence of the proposed DSM is presented in Figure 3-7. Figure 3-7(a) shows the convergence of objective function for both over-relaxed ADMM (o-ADMM) DSM and regular ADMM DSM. Both DSMs converges to the optimum solved in a centralized manner. After the DSMs converge, the performance of both DSMs are stable. Furthermore, we pick the slowest converging bus, bus 11, to take a closer look at the convergence defined by Eq.3.13 in Figure 3-7(b). It shows the primal dual residuals of the o-ADMM DSM and ADMM DSM at bus 11 for both active (P) and reactive power (Q) corresponding to Eq.3.13. It is observed that the over relaxation speeds up the convergence: the o-ADMM DSM converges in 36 iterations while the ADMM DSM takes 70. After 80 iterations, the o-ADMM DSM hits its performance limitation: the residuals stop to decline and stay in an acceptable range. Moreover, we keep tracking the convex relaxation in Eq.3.9 and found it to be tight for all iterations. In a word, the o-ADMM based DSM converges relatively fast.

In the proposed DSM, SAA numerically approaches the stochastic optimization problem. To further validate the performance of SAA, we vary the size of the generated scenario size to examine the impact of scenario size on the DSM. As shown in Table 3-3, we vary the scenario size for 100, 200 and 300, and run the numerical experiment using the same setting for 10 times. We obtain the mean and standard deviation of the 10 experiments for each scenario size. Comparing the results of different scenario size, the mean of the three sets of experiments are close. As expected, the 300 set has a smaller standard deviation. The scenarios size is directly related to the size of the optimization problem, and a large scenario size requires a lot of computational resources. As a conclusion, using 200 scenarios is a safe approach to approximate the EV randomness in the studied setting. For cases requiring medium accuracy, 100 generated scenarios can satisfy the requirements.

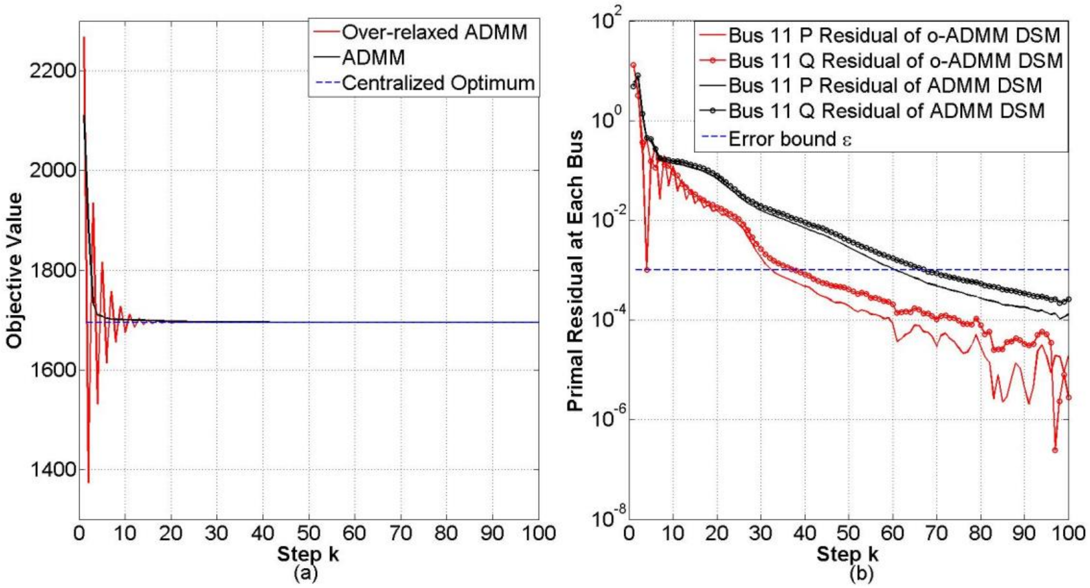

Figure 3-7 (a) Convergence of the Distributed DSMs and (b) primal residuals of bus 11

Table 3-3 Mean and Standard Deviation of Objective Value vs. Scenario Size

Scenarios	**100**	**200**	**300**
Mean	1695.33	1695.29	1696.32
STD	0.1522	0.1199	0.0892

To demonstrate the correctness of the numerical experiments, we also present load profile under bus 11. Bus 11 is picked for analysis as it is the bus most distanced from the root node. As voltage drop is most significant for the buses far away from the root node, we would like to make sure all the constraints are met at bus 11. Firstly, we examined the load profile under bus 11, the battery's active and reactive power together with two EV profiles are shown in Figure 3-8(a). Note that the EV profile is one generated scenario out of 200 total scenarios. It is shown that the battery is most of the time supporting reactive power, which is expected for compensate for the voltage drop in distribution system. Furthermore, in Figure 3-8(b), we align the time axis and present the State-of-Charges (SoCs) for batteries and EVs in the same scenario. For easy representation, we normalized the SoE used in Section 3.3 to SoC in figures. By comparing Figure 3-8(a) and Figure 3-8(b), it is clearly shown that the EV1 arrives at 5am and leave at 1pm while EV2 arrives in 8am and leaves at 9pm. There are some V2G operations for both of the EVs. In Figure 3-8(b), we can also find out prevention of deep discharge of the battery when it hits the SoC lower limit. It needs to be point out that the info of battery, EV1 and EV2 in Figure 3-8 are only accessible by SDSO using the proposed o-ADMM DSM, therefore persevering individual privacy from DSO.

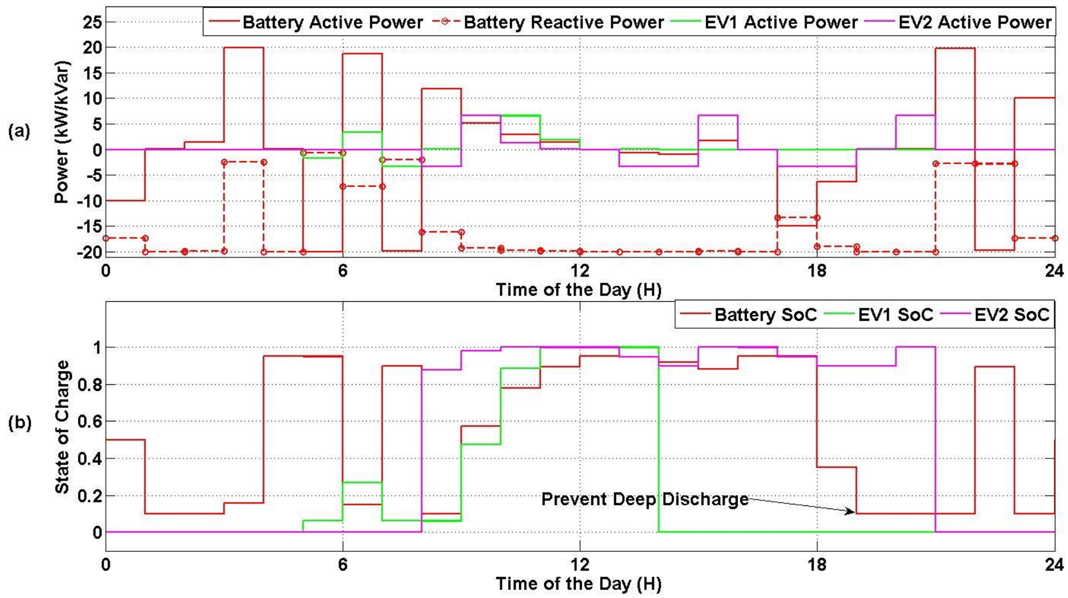

Figure 3-8 SDSO accessible: (a) Load profile under bus 11, (b) SoC of batteries and EVs

Besides checking the load profiles and SoCs, we further presents the bus aggregated load and voltage profile from a DSO's point of view. The aggregated active load, reactive load and voltage profile for the same bus (bus 11) is shown in Figure 3-9. We notice that VR is performed during 10am and 5pm, a time window when system has heavy active load and voltage profile decays accordingly. By comparing Figure 3-9 with Figure 3-8(a), we find out that battery is under reactive power compensation mode in the same time period. Figure 3-8 and Figure 3-9 mutually verify the correctness of the proposed DSM.

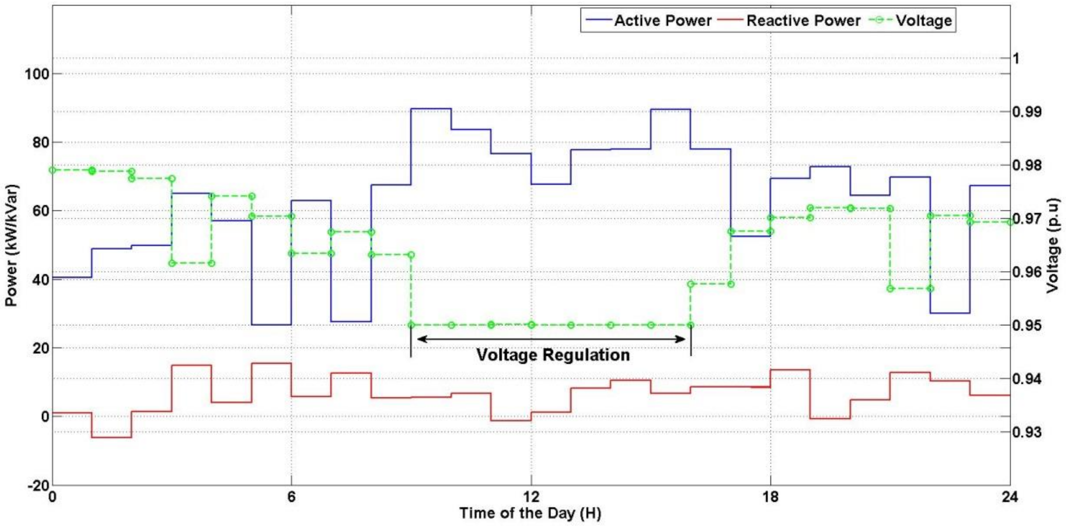

Figure 3-9 DSO accessible: Bus 11 aggregated load profile and bus voltage

3.5.3 Discussions

1) *Scalability*. Figure 3-10 shows the scalability of the proposed DSM under different size of the EV number. We change the number of EVs in the distribution network, from 20 EVs in the original setting to 40 EVs and 60 EVs. Given the limitation of actual EV user profile we have collected, we duplicate the number of EVs under each bus to increase the EV number. We run the numerical experiment by keeping all the other settings the same. In Figure 3-10, it can be clearly seen that as the EV number increases, the problem size scale up linearly with the EV number. However, as the stochastic optimization needs to generate a large number of scenarios for each EV (in this case 200), the problem size actually grows very fast. By integrating 60 EVs, it is already extremely slow to solve the DSM in a centralized way. On the other hand, if we solve it in a distributed manner, the computational burdens are distributed to SDSO. In Figure 3-10, we show three cases of numerical results, namely unstable termination, stable termination and termination with reduced line length. a) the unstable termination refers to the case whose

termination criteria is met according to Eq.3.13 in certain iterations. However, if the algorithm continues to run for one more iteration, the termination criteria is violated. A good example of this case is shown in Figure 3-7(b): at iteration 5, the oscillation introduced by the relaxed term in Eq.3.14 has reduced the error below the pre-set error bound. However, such oscillation has enlarged the error above the error bound in the next iteration. b) the stable termination stands for termination where error continues to stay below error bound. An illustrative example is Figure 3-7(b) at iteration 36. After this iteration, the error continuously stays below error bound. c) we also show the scalability of the same problem with a reduced distribution line length. The line length in this case is reduced to one fifth of the original length.

There are three observations for this numerical experiment: a) by comparing the unstable termination under different size of EV integration, we see a good chance that the o-ADMM based DSM terminates in 10s of iterations. The number of iterations does not grow much as the problem size grows. b) by comparing the stable terminations, we find it scales as the problem scales up. By fitting a first order polynomial between the number of stable iterations and the problem size, it is found out that the distributed method needs to increase one iteration with every increment of 2000 decision variables. There is a chance where the introduced oscillation terminates the algorithm in early stage, however, such termination is not guaranteed. However, in order to obtain guaranteed (stable) termination, the iteration scales up with the problem size. In other words, the distributed DSM reduce the computational burden for the central controller at the expense of longer computational time. c) by comparing the termination with reduced line length case, we further find out that the increase in stable termination actually results from a harder problem: the increase in EV numbers (and hence in energy demand) in the system has made the VR constraints hard to be met. However, if we reduce the line length of the distribution system, the constraints are more easily met and hence iterations do not increase with the problem size.

In general, the large size of scenario that SAA has created combines well with the distributed method. Iterations for convergence increase linearly with the problem size. Although there will be communication delays between SDSO and DSOs, the dispatch of computational burden to distributed controllers parallels processing and therefore potentially decreases the overall computational time. More importantly, by solving the problem in a distributed manner, it makes the problem solvable when it is oversized. It can be also projected that the distributed method proposed in this dissertation works well with deterministic modeling in which the problem size is usually much smaller than its stochastic counterparts.

If the EV size continuous to grow, it can be projected that the problem is harder to solve. With the introduction of more EVs, it not only increases the number of decision variables, at the same time, the EV charging demands also make the voltage and power flow constraints harder to be met. If the EV size is over several hundred, the model used in this chapter may need further adjustments: instead of modeling the stochastic behavior of each individual EV, stochastic modeling should be performed for aggregated EV load under each bus.

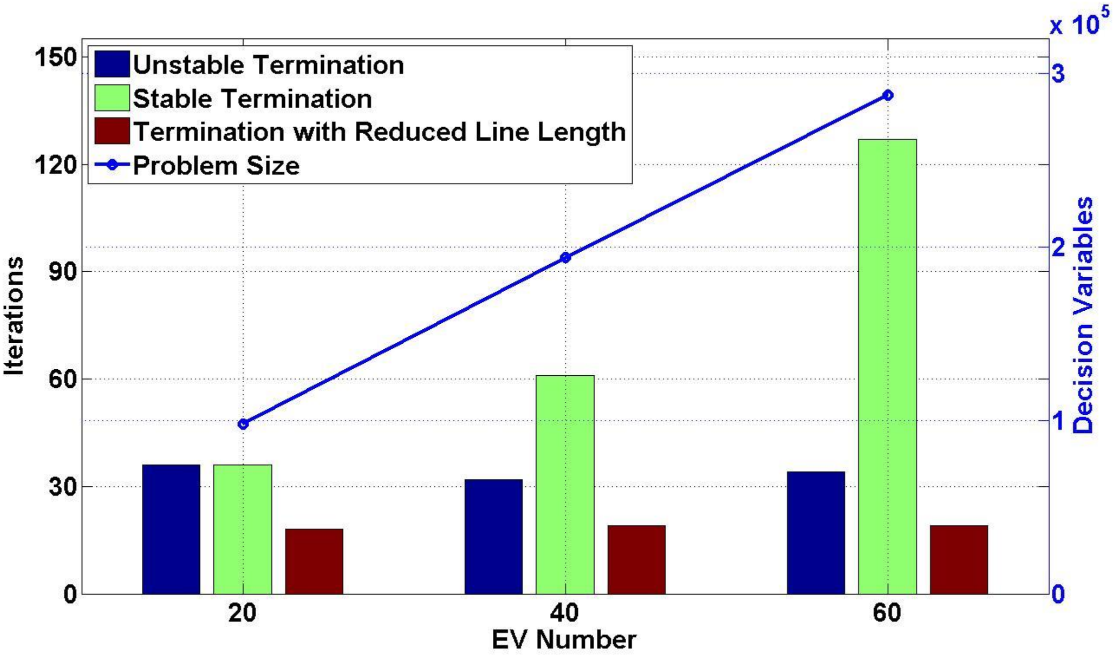

Figure 3-10 DSM scalability and convergence vs. the size of the problem

2) *Stochastic vs. Deterministic*. We use stochastic optimization in the proposed DSM to address the stochastic behavior of the EVs. We show the advantage of using stochastic DSM over deterministic DSM in Figure 3-11. To evaluate the performance of the stochastic DSM and its deterministic counterpart, we have created two test cases using each DSM. The stochastic DSM is created as using the proposed method in this chapter. The deterministic DSM is constructed with the best estimation of EV user behavior, i.e. using the average value of arrival time, departure time and energy demand for each EV user. Then 200 scenarios are generated out of the 60 studied EVs. Averaged EV load mismatch are calculated, which is defined as average mismatch between the estimated EV load at each bus and the generated scenarios, to study the performance of the two DSMs. As the stochastic DSM in this chapter is an unbiased estimation of the averaged EV load at each bus, the mismatch is zero. The averaged mismatch at each bus for deterministic DSM is shown in Figure 3-11. The mismatches are in the day time when EVs

are available to SDSO. One phenomenon mismatch by using deterministic method is at 9am on bus 9. The averaged active power mismatch is 24.4 kW while at the same time the bus 9 base active load is 77.3 kW, which is roughly 31.6% of the overall uncontrollable load. Together with other mismatches in other time under various buses, traditional deterministic method creates problems for DSO to operate the distribution grid.

Two remarks on the numerical results: a) the deterministic DSM using the averaged value for each EV uncertainties still creates considerable power mismatch. There is no guarantee, for the stochastic DSM to outperform its deterministic counterpart in every scenario. However, in a long run (corresponding to larger scenarios), the stochastic DSM will outperform. b) The mismatch may continue to grow when EV number continues to scale up. Therefore, the stochastic DSM is critical for the DSO to estimate the average load under each bus with uncertainty.

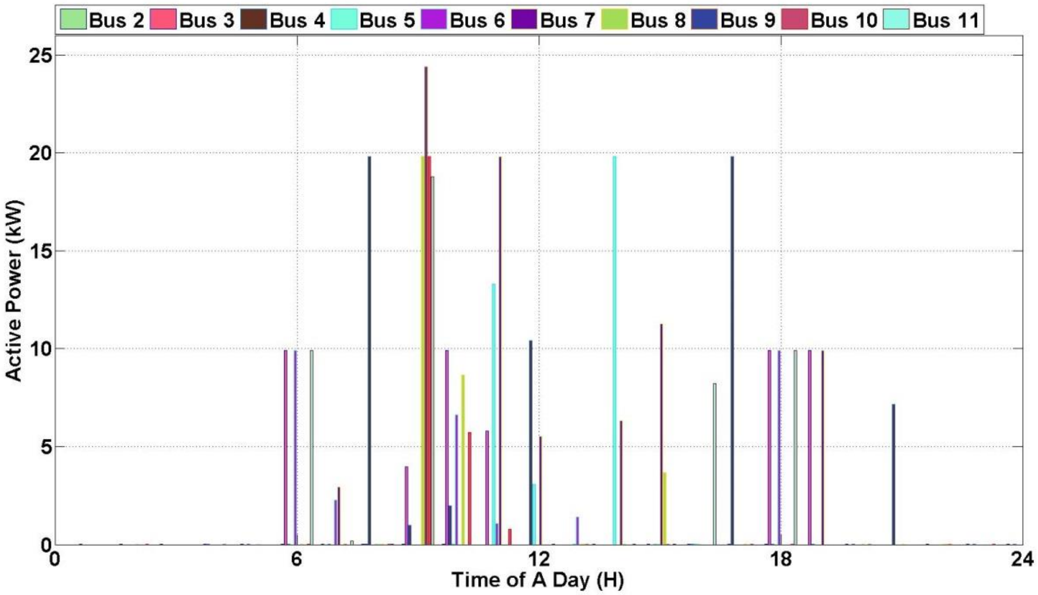

Figure 3-11 Average EV load mismatch for each bus using deterministic method

3) *Lumped Model vs. Networked Model*. We further study the traditional DSM which only accounts for the local effects (LDSM), i.e. minimizing the operational cost under each bus. We

compare the traditional LDSM with the DSM developed in this chapter in Figure 3-12. The two cases are created under same simulation setup with only difference in LDSM not accounting for the network and power flow constraint. As shown in Figure 3-12, we plot the aggregated power losses for the whole network at each time step for both DSMs. Moreover, the maximum and minimum voltage in the whole network at each time step for the two DSMs are also potted for comparisons. It is observed that the LDSM creates a much larger power loss over the distribution line. The total distribution loss is 353.9 kWh for the studied distribution grid by using the proposed DSM for operation. On the other hand, if the traditional lumped model based DSM is applied, the total distribution losses for the load profile will be 719.8 kWh, a loss twice the size of the proposed method. Furthermore, it is also observed that the minimum voltage in the system drops to 0.92 p.u by using lumped model based DSM, while the minimum voltage in the proposed networked based model is regulated at 0.95 p.u.. The numerical results demonstrate the importance of switching from traditional LDSM to the proposed DSM which accounts for the network topology.

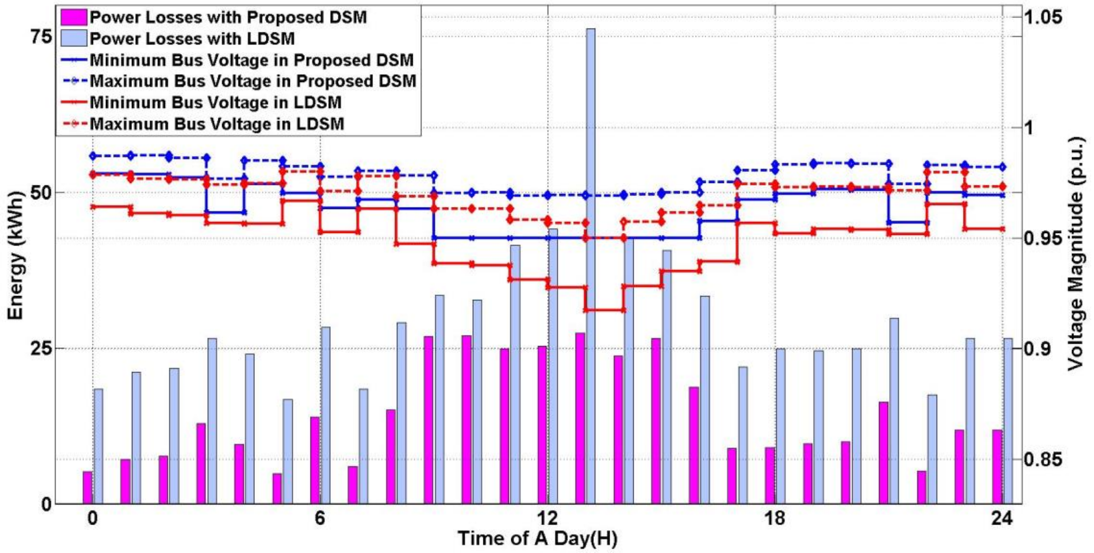

Figure 3-12 Comparisons of power losses and voltage regulation for DSM and LDSM

3.6 Summary

In this chapter, we have proposed a DSM that targets at minimizing the operational cost and distribution losses over distribution networks. It accounts for the stochastic resources in the system, the scalability of increasing controllable devices, and power network physical constraints. For modeling uncertainties of stochastic resources, EVs in this chapter, stochastic optimization is applied. The distribution of the arrival time, departure time and energy demands in EVs are captured using KDE. The stochastic optimization problem is numerically approximated with the help of SAA. Note that other sources of uncertainties in the system (such as solar, load and etc) can be modeled using the same approach proposed in this dissertation, as long as the distribution of the stochastic variables are known. Therefore, the proposed method can be also used for modeling power system integrated with distributed resources such as solar and wind following the same modeling framework. When EV usage pattern for the studied day is outside the scope of its historical records, it can be projected that the proposed DSM will not perform well. This is a problem that all data-driven methods encounter. The degradation of the performance depends on the sensitivity of the model. There is no guarantee that the proposed stochastic DSM performs well in one specific day, however, it outperforms its deterministic counterpart in a long run. On the other hand, distributed DSM proposed in this chapter resolves the scalability issue. As SAA quickly scales up the problem size with the increase integrations of EVs, o-ADMM based DSM dispatches the computational burden originally at DSO to distributed SDSO. Moreover, as a 'side effect', instead of directly communicating the power consumption to DSO, the proposed distributed DSM protects privacy of the end-users by only communicating their dual variables. In the end, we also shows the necessity of switching from a traditional lumped based LDSM to the

DSM that accounts for network topology: the proposed DSM helps to save power losses over the distribution line and regulate the bus voltages within an acceptable range. Apart from cost and power losses minimization studied in this chapter, it must be pointed out that there exists other services that BESS and EV could potentially provide and create greater values. It remains an open question and is to be addressed in future studies. In conclusion, the methods proposed and observations made shed light on future large scale load dispatch and EV/renewable integrations to distribution grids.

4 V2G Integration for Load Sharing

This chapter studies a problem that has smaller time granularity. The studied problem is crucial in microgrid where loads are shared by generations. We use an EV-connected microgrid to demonstrate the problem and show the challenges and proposed solutions.

4.1 Introduction

V2G has received tremendous attention recently in power system stability by using V2G to supply load in power system. Wang et al. focused on peak shaving and valley filling with V2G. The authors proximate desired load curve by convex optimizations, taking into account practical constrains of available EVs and SoC of each EV [108]. Apart from peak shaving, Wu et al. showed frequency deviation and voltage drops caused by active and reactive power imbalance can be regulated by benefiting the relative fast response of V2G [109]. Han et al. estimated the available power capacity of V2G for frequency regulation with normal approximation. Aggregator has to acquire mean and covariance of all EVs with statistics data [110]. Yang et al. solved this problem by finding the optimal incentives using prior knowledge of statistical distribution of EVs' preference [111].

As discussed above, there exists literature discussing research work to enable V2G for load support from top level control and algorithms. However, all of the high level algorithms, including the ones that use stochastic modeling or convex optimizations, inevitably require centralized controls or global information about the EVs in the network. It is hard for aggregators to build realistic models to accommodate the highly distributed and randomized EV driving pattern. More importantly this easily gives rise to privacy concerns from the EV owners [112].

Therefore, for V2G supporting the load, a decentralized approaches is more practical than centralized manners.

This chapter proposes and studies an automatic load sharing approach for V2Gs to share the both active and reactive loads among EVs in a microgrid. The above mentioned V2G load support applications need the global information of the power network and EVs. This chapter accounts for the case when information of other EVs, such as voltage profile and power, in the same microgrid is not available or it is hard to access. Thus, it is necessary to have a localized distributed controller that reacts quickly and makes the global load sharing based merely on each EV's information. The contribution of the chapter is three-fold: First of all, the load sharing is systematically studied for V2Gs. The proposed load sharing takes into account the fact that not only load profile is continuously changing in microgrids, but also the randomness of the connecting and disconnecting of EVs. Second, the proposed control scheme is analyzed and simulated in a microgrid for validation. It sheds light on how V2G for automatic load sharing can be done in large scale. It also analyzes the difficulty in controlling reactive power flow in the proposed control algorithm. Third, the proposed controller takes into account driver preference. Drivers are able to adjust maximum V2G power by setting an upper limit.

The remainder of the chapter is organized as follows: Section 4.2 derives the mathematical model, and Section 4.3 presents the control strategies. To verify the performance of the control, simulation is carried out and results are analyzed in Section 4.4. Finally, conclusion is drawn and future work is discussed in Section 4.5.

4.2 Modeling Methodology

In this section, the problem formulation of V2G automatic load sharing in microgrid is introduced. Then the distributed control algorithm is developed. It is followed by an analysis of system dynamics and active and reactive power sharing. And finally, a load sharing mechanism taking into account driver preference is proposed.

4.2.1 V2G Automatic Load Sharing without Control

The study of automatic load sharing with V2G is carried out in a microgrid with limited communication between vehicles. V2G EVs have only local information and the voltage profiles of other nodes are not known. The target is to achieve load sharing among V2G EVs with limited knowledge of the microgrid. An analysis of load flow in a microgrid reveals many of the general principles useful in load sharing for more complicated cases. The studied system is shown in Figure 4-1. Three V2G EVs are connected to a constant load which has fixed active and reactive power consumption. The EV's DC battery packs are converted to AC with a DC/AC inverter. According to [113], the interface impedance of EV $z_i, i = \{1,2,3\}$ is much larger than the line impedance $z_{ij}, (i,j) = \{(1,2),(2,3),(3,4)\}$. Therefore, it is reasonable to neglect the line impedance. Each V2G EV is represented as a voltage source with an amplitude V_i, and phase angle θi while the load is modeled as a $P + jQ$ constant PQ load. The amplitude and phase angle of a V2G EV can be independently adjusted. In this chapter we assume the V2G EVs response fast and there are no stator transients [114].

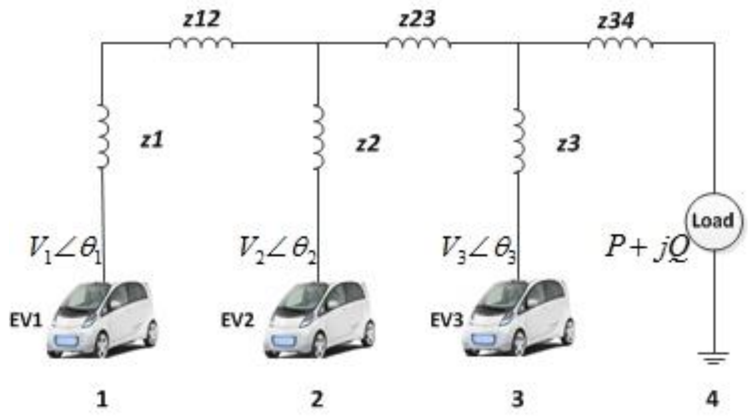

Figure 4-1 Studied V2G automatic load sharing system

Without any additional control, the load cannot be shared proportionally among V2G EVs. In this study, at first the load is *-3-j1.6 pu*, which is shared evenly among the three EVs. However in reality, the load is not constant. A change in load profile, for example the load is changed to *-4-j2 pu*, the additional load will not be shared proportionally among three EVs if these EVs maintain the same voltage profile. Given the fact that each EV has its own maximum allowable V2G power, it is entirely possible that due to the additional load one of the EVs exceeds its maximum allowable V2G power and causing battery damage and safety hazard. Therefore, it needs a closed loop control algorithm to accommodate the load change as well as generation change in the network.

4.2.2 V2G Automatic Load Sharing with Droop Controller

A droop controller for V2G automatic sharing is presented for proportionally sharing the load within one microgrid. Several droop control algorithms for distributed generation are studied in [115] [116]. In this chapter, a conventional droop controller will be considered first and later a revised algorithm better suit to V2G applications will be presented. The droop controller used in this chapter is presented as follows, for active power control:

$$\dot{\delta}_i = -kp_i\left(P_i^m - P_i^0\right) \tag{4.1}$$

And the reactive power control

$$\Delta V_i = -kq_i(Q_i^m - Q_i^0) \tag{4.2}$$

for i = *1,2,3*, where δ_i denotes the phase angle of *i^th^* V2G EV, ΔV_i is the voltage difference between the instant voltage and the initial voltage. Control parameters kp_i and kq_i are active and reactive power droop coefficients for the *i*th EV, respectively. P_i^0 and Q_i^0 represent the reference active power and reactive power. P_i^m and Q_i^m are the measured active and reactive power. The controller works like a droop, i.e., when the measured active power is larger than the reference value; it decreases its phase angle.

The sensors for measuring the active and reactive power can be modelled as first order systems; the time-constant of the system models the sensing delay:

$$\frac{P_i^m(s)}{P_i(s)} = -\frac{\omega_f}{s + \omega_f} \tag{4.3}$$

and

$$\frac{Q_i^m(s)}{Q_i(s)} = -\frac{\omega_f}{s + \omega_f} \tag{4.4}$$

where $P_i(s)$ and $Q_i(s)$ represents the instant active and reactive power of *i*th V2G EV and ω_f is the time constant.

4.2.3 System Dynamics of the Microgrid

The power flow of each bus shown in Figure 4-1 can be expressed as follows:

$$P_i = \sum_{j=1}^{4} V_i V_j (G_{ij} \cos \delta_{ij} + B_{ij} \sin \delta_{ij}) \tag{4.5}$$

$$Q_i = \sum_{j=1}^{4} V_i V_j (G_{ij} \sin \delta_{ij} - B_{ij} \cos \delta_{ij}) \qquad (4.6)$$

for $i=1,2,3,4$, where $\delta_{ij} = \delta_i - \delta_j$, and G_{ij} and B_{ij} can be extracted from admittance matrix.

Following controller described in Eq.5.1 and Eq.5.2 and the sensor dynamics in Eq.5.3 and Eq.5.4, the dynamics of the system is described as follows:

$$\dot{\delta_\imath} = -kp_i \Delta P_i^m \qquad (4.7)$$

$$\Delta \dot{P_i^m} = -\omega_f (\Delta P_i^m - \Delta P_i) \qquad (4.8)$$

$$\Delta \dot{Q_i^m} = -\omega_f (\Delta Q_i^m - \Delta Q_i) \qquad (4.9)$$

i = 1,2,3, where

$$\Delta P_i = \sum_{j=1}^{4} \Delta P_{i\delta_j}^0 \Delta \delta_j \qquad (4.10)$$

$$\Delta Q_i = \sum_{j=1}^{4} \Delta Q_{i\delta_j}^0 \Delta \delta_j \qquad (4.11)$$

and $\Delta P_i^m = P_i^m - P_i^0$, $\Delta Q_i^m = Q_i^m - Q_i^0$, $\Delta P_{i\delta_j}^0$ and $\Delta Q_{i\delta_j}^0$ can be obtained from Eq.5.5 and Eq.5.6 with partial differentials around equilibrium points:

$$\Delta P_{i\delta_j}^0 = \left. \frac{\partial P_i}{\partial \delta_j} \right|_{P_i^0} \qquad (4.12.a)$$

$$\Delta Q_{i\delta_j}^0 = \left. \frac{\partial Q_i}{\partial \delta_j} \right|_{Q_i^0} \qquad (4.12.b)$$

Expressions for Eq.5.12 can be obtained from Eq.5.5 and Eq.5.6. The dynamics of the system is linearized with Eq.5.12 and can be modeled with the above differential equations.

4.3 V2G Automatic Load Sharing

With the physical model derived above, we are ready to present the V2G automatic sharing control strategy considering driver preference.

4.3.1 Active and Reactive Power Sharing with V2G

For active power, the system will reach a steady state, when the following equations hold:

$$\dot{\delta_1} = \dot{\delta_2} = \dot{\delta_3} \tag{4.13}$$

The system will falls into steady state when the changing rates of δ_i are the same. In steady state, $P_i^m = P_i$. Therefore, the active power of the microgrid is shared proportionally as follows:

$$kp_1(P_1 - P_1^0) = kp_2(P_2 - P_2^0) = kp_3(P_3 - P_3^0) \tag{4.14}$$

On the other hand, reactive power sharing is a much complicated problem that requires further discussion. In the following analysis, it is assumed that the microgrid has a low *R/X* ration and we assume there is no sensor delay in Eq.5.4. Then Eq.5.6 can be rewrite as:

$$Q_i = -V_i V_4 B_{i4} \cos \delta_{i4} - V_i^2 B_{ii} \tag{4.15}$$

for *i=1,2,3,* where $B_{i4} = -B_{ii}$. Supposedly there is a change in node 4. For simplicity without losing generality, the relative angles δ_{i4} stay exactly the same in active power steady state. Then Eq.5.15 can be reformulated as:

$$\Delta Q_i = kq_i \Delta Q_i V_4 B_{i4} \cos \delta_{i4} - V_i \Delta V_4 B_{i4} \cos \delta_{i4} - 2kq_i \Delta Q_i V_i B_{i4} \tag{4.16}$$

Following Eq.5.16, the reactive power is shared as follows

$$\frac{\Delta Q_i}{\Delta Q_j} = \frac{V_i kq_j \cos \delta_{i4} \,(V_4 B_{j4} \cos \delta_{j4} - 2V_j)}{V_j kq_i \cos \delta_{j4} \,(V_4 B_{i4} \cos \delta_{i4} - 2V_i)} \tag{4.17}$$

for *i,j =1,2,3*. It is clearly shown that the reactive power sharing is highly coupled. The proportion depends on a number of parameters besides the reactive power sharing coefficients.

4.3.2 V2G Automatic Load Sharing with Driver Preference

From the previous derivation and analysis, it is shown though reactive power cannot be easily shared among V2G EVs, active power is shared proportionally. Inspired by this fact, this chapter proposes a droop based active power sharing with driver preference. The driver of each EV is able to choose an upper limit that prevents active power shared beyond the limit. It corresponds to different maximum V2G power allowed for different EV models in practice. The controller is described as follows:

$$\begin{cases} \dot{\delta}_\iota = -kp_i(P_i^m - P_i^0) & P_i^l > P_i^m \\ \dot{\delta}_\iota = -kp_i(1 + P_i^m - P_i^l)(P_i^m - P_i^0) & P_i^l \le P_i^m \end{cases} \tag{4.17}$$

where P_i^l is the maximum allowable active power sharing for *ith* EV. The active load sharing works as conventional droop controller when the measured power does not exceed the maximum allowable power. However, when the measured power exceeds the limit, the local droop based controller dynamically adjusts its sharing coefficient based on the feedback of how much power it exceeds the limit. The more V2G power it exceeds its limit, the faster its active power sharing coefficient increases, consequently the lower active power the EV is sharing. It is noted that there is a possibility when the supply of the grid cannot meets its demand, which may result in oscillation of the microgrid. It will be discussed in the following section.

4.4 Results and Analysis

Based on the analysis of the previous section, this section simulates three practical scenarios of using V2G for automatic load sharing, including a case when an EV is connected to the network with constant load, a case when EVs are connected but load changes and a case when load stays the same while an EV is disconnected from the network. All other application scenarios of V2G automatic load sharing in microgrid level is a combination of these three fundamental scenarios. Thus, it is important to understand these three fundamental application scenarios.

4.4.1 V2G Load Sharing with Additional EV Be Connected

In the first simulation, a fundamental V2G automatic load sharing scenario is studied. Following the topology described in Figure 4-1, originally EV1 and EV2 are connected to a constant PQ load and reach a steady state. Then EV3 is connected to the original network while the load stays constant. The target of this simulation is to verify the controller as well as study its dynamic behavior and stability. The system parameters of the microgrid are specified in Table 4-1. The microgrid is modelled as a lossy network with a low *R/X* ration.

Table 4-1 System Description of the microgrid

Parameter	**Value**
kp	*[0.1 0.3 0.2]*
kq	*[0.001 0.003 0.002]*
z_1 *(p.u.)*	*0.01+j0.05*
z_2 *(p.u.)*	*0.01+j0.10*
z_3 *(p.u.)*	*0.005+j0.15*
load (*p.u.*)	*-3-j1.6*
ω_f*(rad/s)*	*10*

Figure 4-2 shows the automatic load sharing of the described scenario. EV3 is not connected to the microgrid at first with both active and reactive power at *0pu*. The load is shared by EV1 and EV2. At *t=1s*, EV3 is connected to the original network and additional generation is introduced to the microgrid. Active and reactive power of the load is shared by EV3. Thus, P1 and P2 drops while P3 increase. It is noted that the reference active power used in this simulation for EV3 is $2p.u.$ As shown in the figure, $\Delta P_1 = 1.10p.u.$, $\Delta P_2 = 0.37p.u.$, $\Delta P_3 = 0.56p.u.$ and $kp_1 \Delta P_1 = kp_2 \Delta P_2 = kp_3 \Delta P_3$ within acceptable errors. The errors result from two major reasons: first, the sensing delay of sensors; and second, the microgrid studied in this simulation is not a non-lossy network. Some shared active power is compensated in the lossy network.

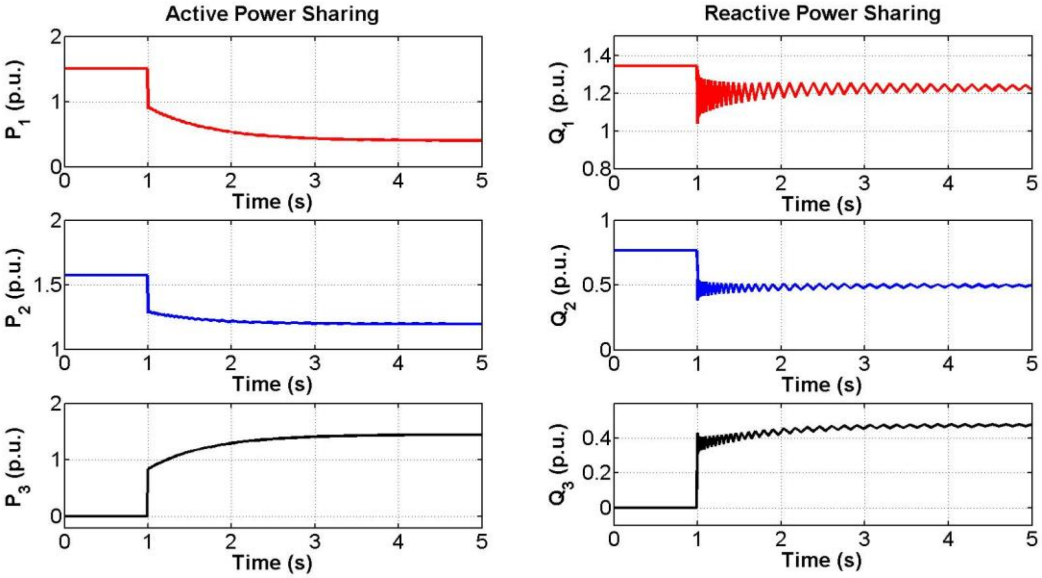

Figure 4-2 Automatic load sharing with V2G when an EV is connected to the original microgrid

On the other hand, reactive power sharing is much more complicated. It is observed that $\Delta Q1 = 0.13p.u.$, $\Delta Q2 = 0.37p.u.$, $\Delta Q3 = 0.02p.u.$ As shown in Figure 4-2, reactive power sharing has oscillations at each EV. This is expected, as shown in Eq.5.16, $cos\delta_{i4}$ does not equal to a constant number before it reaches steady state. As presented in Eq.5.17, the reactive power sharing is related to a number of factors besides the reactive sharing coefficients, not to mention Eq.5.17 is a simplification for non-lossy networks. To the best of authors' knowledge, compared to active power sharing, the problem of reactive power sharing has not yet reached a universal and decent solution [117]. More efforts are needed to understand the reactive power flow and resonance in power network.

Figure 4-3 presents the phase angle and voltage amplitude change over time of the studied scenario. As indicated in the figure starting from $1s$, EV3 is connected to the network, which introduces dynamic response to the system. The phase angle differences $\delta_i - \delta_j$ $(i \neq j, i, j = 1,2,3)$ stay the same after the changing rates δ_i $(i = 1,2,3)$ are synchronized. It is shown in Figure 4-3 that after *3s*, the three curves of phase angle are almost parallel. It matches Figure 4-2 which shows a steady state of active power sharing has reached after *3s*. It also verifies the stability analysis in Eq.5.13 and Eq.5.14.

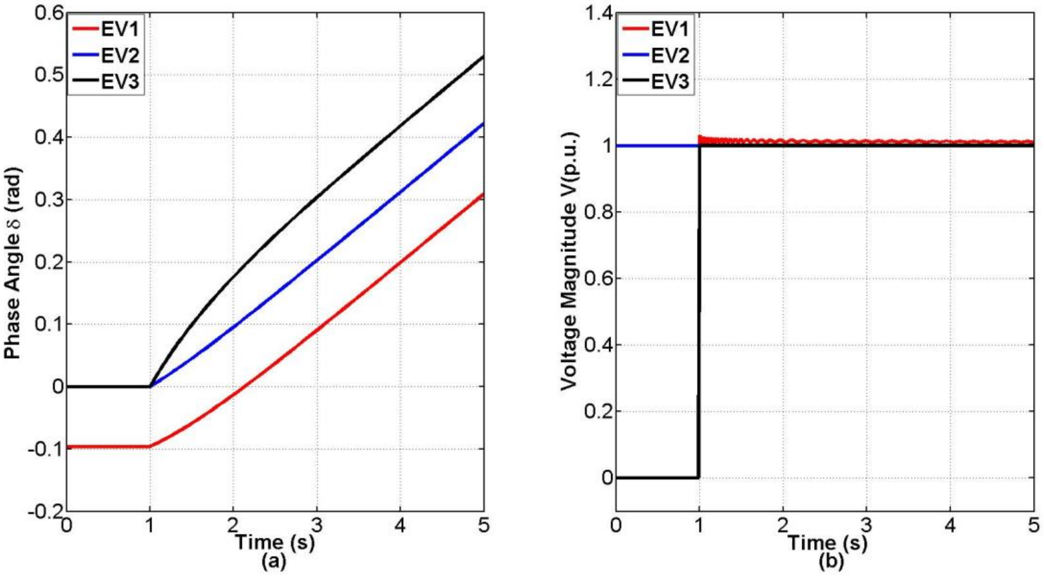

Figure 4-3 Phase angle (a) and voltage (b) amplitude change over time of automatic load sharing with V2G

4.4.2 V2G Load Sharing with Load Change and Driver Preference

Apart from studying how an EV connection introduces dynamics to the microgrid level V2G load sharing, it is essential to understand how power is shared when there are no EV connections and disconnections dynamics, but rather a load change in microgrid. A simulation is run with EV1, EV2 and EV3 connected to the microgrid supporting load through V2G. Load change both in active and reactive then happens and V2G EVs react to this change. This simulation shows how driver preference affects automatic load sharing in microgrid.

As for preference, it corresponds to the upper limit of V2G active power for each EV, i.e. P_i^l, mentioned in Eq.5.18. In this simulation, a case which one of the EVs has a lower allowable V2G power is simulated: $P_1^l = 1.5p.u., P_2^l = P_3^l = 2.5p.u.$ This is a reasonable assumption because in practice, different EV models allow different maximum V2G power.

Figure 4-4 presents the simulation results of load change with driver preference in solid line and without driver preference with dash line for 3 V2G EVs. At first, EV1, EV2 and EV3 are sharing active and reactive power at steady state. At *t=1s*, the load changes from *-3-j1.6p.u.* to *-5-j2p.u.* The additional load will be shared among three V2G capable EVs. As shown in the figure, after the load increases, EV1's active power sharing increases to *2p.u.* which exceeds its maximum allowed V2G active power. The controller in Eq.5.18 detects the overflow, and then dynamically decreases EV1's active power sharing according to the feedback of how much it exceeds the limit. As shown in Figure 4-4, the active power sharing of EV1 is constrained to *1.5p.u.* versus if sharing *2.1p.u.* if no driver preference is implemented. The observed delay time before P_1 decreases from *2p.u.* is due to sensing delay. An overshoot is observed at *t=1.3s*, which is desired: in practice, power electronics can only sustain overcurrent for a short time. Thus, an under-damped system with overshoot decreases its time working in overcurrent operations.

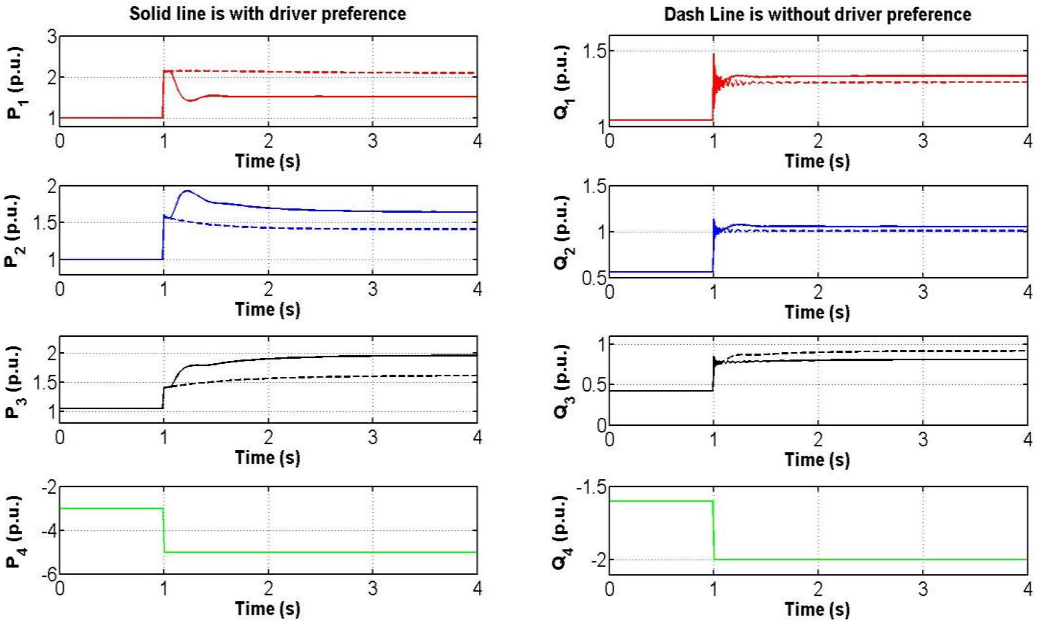

Figure 4-4 Automatic load sharing with V2G when load changes

It is noted that there is a possibility when the three EVs' maximum allowed V2G active power combined cannot meet the demand of the load. In that case, the droop based driver preference controller can never reach a steady state. However, this is something not expected as automatic load sharing only make sense when generation meets the demand. Figure 4-4 also presents the reactive power sharing under driver preference. Though the driver preference controller is implemented for active power sharing, it slightly affects relative power sharing. This is expected, because Eq.5.17 shows reactive power sharing is related to δ_{i4} which is affected by active power sharing.

4.4.3 V2G Load Sharing with EV Be Disconnected

In the end, it is necessary to study how EV's disconnection affects the power sharing of connected EVs while the load stays constant. Combined with the previous two simulations, it accounts for all fundamental V2G automatic load sharing dynamics in a microgrid.

During this simulation, the load is constant. As shown in Figure 4-5, at first, three EVs are sharing active and reactive power through V2G at steady state. At *t=1s*, EV3 is disconnected to the microgrid. It is observed that $\Delta P_1 = -0.79 p.u.$, $\Delta P_2 = -0.28 p.u.$, which correspond to the active power sharing control $kp_1 \Delta P_1 = kp_2 \Delta P_2$. It is also observed $\Delta Q_1 = -0.17 p.u., \Delta Q_2 = -0.31 p.u.$ Similar to analysis in the previous section, the reactive power is not shared according to reactive power sharing coefficient. This simulation also shows that even for a simple case when only load is shared between two V2G EVs, reactive power sharing is hard to control. It needs more effort before researchers can proportionally share reactive power as its counterpart.

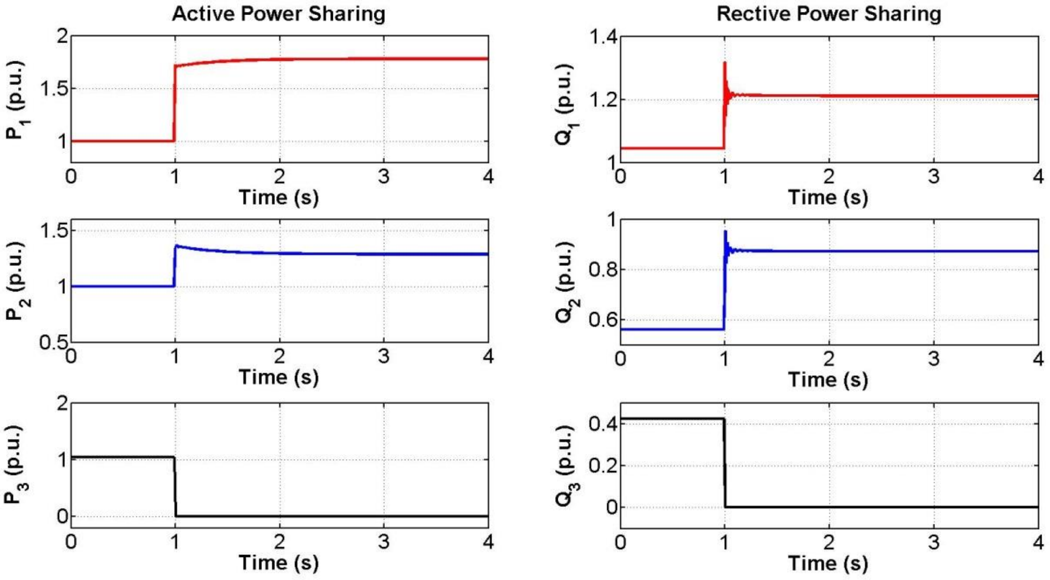

Figure 4-5 Automatic load sharing with V2G when an EV is disconnected to the network

4.5 Summary

This chapter presents a droop based automatic load sharing with driver preference using V2G capable EVs in a microgrid. Unlike conventional centralized control methods, this chapter studies a scenario when communication is limited, and V2G EVs have to adjust active and reactive power sharing based on their own information. A microgrid with connected EVs is modeled as a lossy network with low *R/X* ration without loss of generality. The power flow and load sharing among EVs are carefully analyzed with reasonable simplifications. A droop based controller taking into account driver preference is proposed in this chapter. It limits the V2G active power sharing to the driver's preset maximum value, which models the maximum allowable V2G power in practice. Stability of the controller is studied to understand the robustness of the studied system. The analysis of the active and reactive power sharing in a microgrid level sheds light on large scale V2G load sharing in distribution networks. Three practical application scenarios of V2G load sharing are simulated, which include a case when an EV is connected to the microgrid with constant load, a case when load changes while EVs are connected and a case when an EV disconnects to the microgrid with constant load. All other application scenarios of V2G automatic load sharing in microgrid level is a combination of these three fundamental scenarios. Simulation results show that the proposed controller constrained the active power sharing to the EV driver's preference. Simulation results also demonstrate the stability of the system and proportional active power sharing among V2G EVs. However, reactive power cannot be shared proportionally as active power, due to the fact that it is highly coupled. More efforts on understanding and decoupling the reactive power sharing are needed in the future.

5 System Uncertainty Predictions

In the previous chapters, when control and optimizations were run for energy management, we assume the perfect knowledge of solar generation and loads in the system. However, in fact they are not known. This chapter studies the uncertainty prediction problem using a solar generation on UCLA campus. Study shows the predictions of solar with the combination of global-tier and local-tier can be quite accurate. The same prediction framework can be used to predict load in the system.

5.1 Introduction

The prediction of solar power generation can be generally classified into two categories, i.e., model based predictions and model-free predictions. In model based predictions, disturbance source and factors that impact in the solar generations are taken into consider. These factors are finally plugged into the famous I-V curve for prediction of the solar power [118]. Huang et al. studied the short term solar irradiance change based on cloud motion image processing [119]. While Capizzi et al. looked at environmental parameters such as humidity and temperature to estimate their correlation with solar generation [120]. These methods give precise predictions of solar generation relying on excessive prior knowledge of the environmental conditions. It costs additional expense in installing sensing and communication facilities, which is applicable to utility solar farms with aggregated solar generation at MW level. However, in distributed solar generations of smaller sizes, it is common that the solar panels are operating without temperature, irradiation and humidity sensors.

The majority of solar power prediction relies on high computation power. Solar power generations are sampled and stored for researchers to extract the time-domain or frequency-domain characteristic. Based on the correlation of historical data, the predictions are made with methods widely used in time sequence analysis and machine learning. Huang et al. made prediction of the solar irradiance based on Auto-Regressive Moving Average (ARMA) model [121]. Given the order of ARMA cannot be too high, they are perfect for real-time predictions but for day ahead prediction, its performance is limited. Negash et al. studied the same problem with NARX model [122]. Deng et al. solve the problem with support vector machine [123]. The performance of this method is highly dependent on long term data collection. The longer the data collection period lasts, the more likely future generation may fall into historical patterns. As these methods do not consider using additional sensor for detecting environmental variation, the prediction accuracy can be limited if the weather changes abruptly or absence of long term data collection

This chapter studies a typical scenario of roof-top solar power generation at residential homes and commercial buildings, which real-time temperature, irradiation and humidity information is not available. We propose a two-tier adaptive method for solar power generation prediction using historical power data along and verifies with 35kW capacity solar generations in UCLA microgrid. To study how different global-tier predictions may affect the overall performance of the two-tier prediction, global-tier day-ahead predictions are performed with two heuristic methods, i.e., weighted k-Nearest Neighbors (k-NN) and NN. In local-tier, adaptive real-time corrections based on residual analysis is applied for further improvement of the day-ahead prediction results. We present extensive analysis and comparisons on the performance of the proposed method. The contribution of the chapter is three-fold: first, compared with traditional day-ahead predictions, the proposed method achieves higher accuracy. Second, unlike most of real-time models, the proposed local-tier prediction is not heuristic. The analytical form local-tier has a clear physical meaning. It can be combined with other day-ahead prediction methods to improve prediction accuracies. Finally, reasons for why NN-based two-tier adaptive prediction method in general outperforms weighted k-NN based counterpart are discussed, which sheds light on principles to design global-tier method.

The remainder of this chapter is organized as follows: Section 5.2 articulates global day-ahead prediction methods. Both weighted k-NN and NN model are used for prediction. It is followed by presenting the local real-time residual analysis based correction method in Section 5.3. Section 5.4 discussed the experimental setup and results analysis. Finally, conclusions are drawn in Section 5.5.

5.2 Global-Tier Day-Ahead Predictions

The proposed adaptive prediction method has two tiers, i.e., global-tier day-ahead prediction and local-tier real-time correction. Assume that solar power data are sampled with a sampling interval of Ts for N days, we have a sequence of measured solar power data P:

$$P = \{P_1(0), P_1(T_s), \dots, P_i(mT_s), \dots, P_N(MT_s)\} \tag{5.1}$$

where $m \in \{0,1,\dots,M\}$, $i \in \{1,2,\dots,N\}$, $P_i(mT_s)$ denotes the measured power of ith day at time instant mT_s , and M is maximum samples per day.

The goal is to provide day-ahead prediction of solar power generation as precise as possible. Two popular heuristic methods are investigated: weighted k-NN and NN. Both models need to be trained before prediction. For both models we assume that collected data is arranged in chronical order and first rN days of data is used for training purpose with $r \in (0,1)$. The $(1-r)N$ days of the remaining data is used for evaluation of the performance of the models. We use

x_t and y_t as the training input and output sets for the models, and x_v and y_v as the verification input and verification output sets. Then we will have:

$$x_t, y_t \in \{P_1(0), P_1(T_s), \ldots, P_1(MT_s), P_2(0), \ldots, P_{rN}(MT_s)\} \tag{5.2}$$

We assume that $\widetilde{P_g}(mT_s) \in y_v$, $g > rN$ where $\widetilde{P_g}(mT_s)$ is the predicted solar generation power in day g at time mT_s,then we have:

$$x_v \in \{P_i(mT_s) | 0 < i < g, 0 \leq m \leq M\} \tag{5.3}$$

Also assume that

$$x_t^p \in x_t, y_t^p \in y_t, x_v^q \in x_v, y_v^q \in y_v \tag{5.4}$$

where x_t^p and x_v^q, y_t^p and y_v^q are respectively pth and qth elements in their own sets. The day-ahead prediction method problem is to predict the solar generation of the next day based on the historical data, and is formulized as follows:

$$\tilde{y}_t^p = f(x_t^p), \tilde{y}_v^q = f(x_v^q) \tag{5.5}$$

where f denotes the mapping from historical values to predicted values and $\tilde{y}_t^p$, $\tilde{y}_v^q$ are the prediction of y_t^p and y_v^q . The problem is subsequently formulated as how to map historical data to day-ahead predictions.

To evaluation the performance of the prediction, we use Root Mean Squared Error (RMSE) defined as follows:

$$RMSE = \sqrt{\frac{1}{M} \sum_{m=0}^{M} \left(\widetilde{P_g}(mT_s) - P_g(mT_s)\right)^2} \tag{5.6}$$

To demonstrate that the proposed local-tier adaptive prediction method works with general global-tier prediction methods and study how different global-tier predictions affect the performance of two-tier prediction, weighted k-NN and NN are studied in global-tier day-ahead prediction.

5.2.1 Weighted k-NN Model

Weighted k-NN is an evolution of the machine learning algorithm k-NN [124]. The idea of weighted k-NN is to search for the k-nearest most similar patterns and combined them with higher weight to more similar ones for prediction.

The weighted k-NN algorithm is shown in Algorithm 5.1, the data for training the weighted k-NN model is following:

$$x_t^i = \{P_{i-D}(0), \dots, P_{i-D}(MT_s), P_{i-D+1}(0), \dots, P_{i-1}(MT_s)\} \tag{5.7.a}$$

$$y_t^i = \{P_i(0), P_i(T_s), \dots, P_i(MT_s)\} \tag{5.7.b}$$

Note that the initiative behind the algorithm is it relates the specific day's prediction with the observed *D* previous days.

Algorithm 5.1. Day-ahead Prediction with Weighted k-NN

```
Data: $x_t, y_t$
Input: $x_v$
Output: $\tilde{y}_v$
for each $x_v^j \in x_v$ do
    for each $x_t^i \in x_t$ do
        $dst(i,j) = ||x_v^j - x_t^i||$
    end
    $idx(l) = i$, where $dst(i,j)$ is the $l^{th}$ smallest element
    for each $l \in \{1,2,\dots,k\}$ do
```

```
        $w(l) = \frac{dst(idx(k+1),j)-dst(idx(l),j)}{dst(idx(k+1),j)-dst(idx(1),j)}$
    end
    $\tilde{y}_v^j = \frac{1}{\sum w(l)} \sum_{l=1}^{k} w(l) y_t^{idx(l)}$
end
```

It also needs to point out that the distance we are using in the weighted k-NN is Euclidian distance. It reveals the similarity between data sets. Furthermore, the weighted k-NN algorithm differs from traditional k-NN in a way that it gives more weight to more similar patterns. Typically, weighted k-NN gives better prediction results compared to k-NN.

5.2.2 NN Model

NN is an effective model for predictions and pattern recognitions. The essential idea behind the model is to use multi-layer NNs in capturing the high dimensional nonlinear mapping between inputs and outputs. The structure of the NN used in this prediction is shown in Figure 5-1.

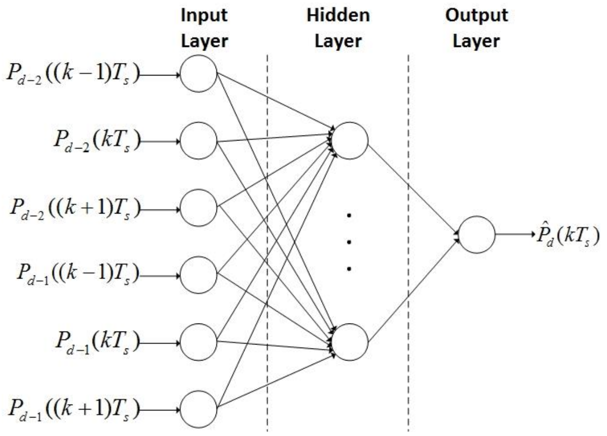

Figure 5-1 Topological structure of the NNs

As shown in Figure 5-1, the output power at time instance kT_s of d^{th} day is related to the previous two days. The NN model uses three layers with a hidden layer in between the input and output layer. For hidden layer neuron number, there are a lot of discussions, one of a data driven methods is documented in [125]. We will discuss the hidden layer neuron number in Section 5.4.

5.3 Local-Tier Real-Time Correction

The global-tier day-ahead solar power prediction is made with the two methods discussed in the previous section. However, the accuracy must be limited as we are making day-ahead prediction without the knowledge of solar generation in the predicted day. With the real-time solar generation of the predicted day, prediction results can get substantial improvements. Assume at time instance mT_s of i^{th} day, we have measured data $P_i(mT_s)$ and day-ahead predicted data $\tilde{P}_i(mT_s)$. The residual $R(m)$ is defined as:

$$R(m) = \tilde{P}_i\,(mT_s) - P_i(mT_s) \tag{5.8}$$

The index for ith day is in $R(m)$ omitted as we are making real-time correction.

The underlining idea of local real-time correction is to extract the low frequency components in residual sequence. See [126] for a detailed discussion on residual analysis. We define the sequence of residual to be

$$S_n^m = \{R(m - n + 1), R(m - n + 2), \dots, R(m)\} \tag{5.9}$$

where $m \geq n - 1$ and S_n^m is the residual sequence at time instant mT_s with length n. We use Discrete Fourier Series (DFS) to extract the low frequency component of the residual sequence. The DFS of the S_n^m is represented as:

$$S_n^m(k) = \sum_{i=0}^{L}\left(a_i \cos\left(k\frac{2\pi i}{T_s}\right) + b_i\ \sin\left(k\frac{2\pi i}{T_s}\right)\right) \tag{5.10}$$

where $k = [1,2, \dots, n]$. $S_n^m(k)$ is the k^{th} component of S_n^m. a_i and b_i are the DFS coefficients representing the ith frequency components. The sampling frequency T_s determines the bandwidth of signal and sampling point n determines the resolution of discrete frequency components [127]. L represents the maximum allowable frequency component. We construct matrices as follows:

$$S = [S_n^m(1)\; S_n^m(2) \dots S_n^m(n)]^T \tag{5.11}$$

$$C = [a_0\; b_0\; a_1 \dots b_L]^T \tag{5.12}$$

$$F_{uv} = \begin{cases} \cos \dfrac{2\pi(\frac{\overline{u}}{2} - 1)}{T_s} v & mod(u, 2) = 0 \\ \sin \dfrac{2\pi(\frac{\overline{u}}{2} - 1)}{T_s} v & mod(u, 2) = 1 \end{cases} \tag{5.13}$$

where $u = [1,2, \dots, 2L], v = [1,2, \dots, n]$. Then the coefficient can be estimated with least-square methods as follows:

$$C = (F^T F)^{-1} F^T S \tag{5.14}$$

Given an estimation of coefficient matrix, we can compute $S_n^m(k)$ according to Eq.5.10 and use it for correction of the future day-ahead predictions. Using the computed low frequency components in Eq.5.10, we dynamically update the day-ahead prediction as follows:

$$\tilde{P}_i^c(lT_s) = \tilde{P}_i(lT_s) + S_n^m(mod(l - k, k) + 1) \tag{5.15}$$

where $l\ [m + 1, m + 2, \dots, M]$ and $\tilde{P}_i^c(lT_s)$ is the corrected prediction of ith day at time lT_s and $\tilde{P}_i(lT_s)$ is the global-tier estimation result. The local-tier correction takes into account the real-time trend and adaptively updates the day-ahead estimated value. In the following sections we will see how lower frequency components of residual sequence contribute to better solar power predictions.

5.4 Results and Analysis

In this section, UCLA microgrid is used as the testbed for evaluation of the proposed algorithms. Solar generation data is collected from 35kW capacity solar panels. For further information about solar generation at UCLA, online access can be found [62]. 50 days of solar data was collected from Feburary for training and verification of the algorithm. 60% of the data is used for training purposes, 20% for model tuning, and the remaining 20% is used for testing and analysis. Data are collected with $T_s = 15$min.

5.4.1 Model Tuning

For weighted k-NN day-ahead prediction, parameters D and k need to be tuned and determined. The comparisons of D and k are carried out with 20% of collected data Table 5-1 shows how the average RMSE varies over D. D is tested varying from 1 to 8 with each RMSE representing the daily average RMSE of the verification data. Noted that test on the parameter k has also been carried out and tested from 2 to 4 (if k = 1 then weighted k-NN decays to k-NN) with k = 2 the smallest. Comparison results show that the weighted k-NN day-ahead prediction works best with k = 2 and D = 5. It means that combining only the two closest neighbors, the solar power generation falls into very different patterns. And D = 5 shows that when predict solar generation data with five previous day generates best results.

Table 5-1Comparisons of RMSE over D

D	**1**	**2**	**3**	**4**
RMSE*	0.669	0.572	0.649	0.420
D	**5**	**6**	**7**	**8**
RMSE	0.405	1	0.939	0.865

*RMSE4943.6 is normalized to 1

For NN based day-ahead prediction, the number of hidden layer neurons needs to be determined. Same 20% of collected data is used for determination of the hidden layer neuron number. However, as is well known that training results of NN is determined by the random initial value, and sometimes bad initial values may drag the NN into local optimum. Taking the randomness into account, we trained the NN for 10 times with Levenberg-Marquardt method and get the average value of RMSE. From the results shown in Table 5-2, we found out NN with 6 hidden layer neurons gives the best prediction results. When the hidden layer neurons are greater than 6, there is no significant improvement on accuracy resulting from the problem of over-fitting.

Table 5-2 Comparisons of RMSE over hidden layer neurons

N	**3**	**4**	**5**
RMSE*	1	0.959	0.943
N	**6**	**7**	**8**
RMSE	0.907	0.940	0.956

*RMSE 2499.5 is normalized to 1

Though we have determined the optimal parameters for the day-ahead predictions, the optimal parameters are not acquired with analytical methods. It implies that the optimal parameters are perhaps data-dependent. Therefore, with longer period of data collection, we may finally reach to a set of stable data driven optimal parameters for day-ahead predictions. On local real-time correction side, the sequence length n is chosen to be 8, i.e., a two-hour observation. The length n determines the resolution in its frequency spectrum. Parameter L is selected as 2, which only accept the first two frequency component of the residual sequence. Increasing L means adding additional higher frequency variation into the correction signal. Noted that L cannot be larger than $n/2$ otherwise the problem of least-square becomes overdetermined.

5.4.2 Results Analysis

Figure 5-2 shows the overall prediction accuracy for all test days. The four curves indicate the RMSE of predicting using weighted k-NN along, NN along, two-tier prediction with weighted k-NN as the global-tier prediction and two-tier prediction with NN as the global-tier prediction respectively. The averaged RMSE over test days of each curve is also plotted. It is observed from the results that weighted k-NN and NN based day-ahead prediction gives similar prediction accuracy. However, when combined with the local-tier correction, weighted k-NN and NN based two-tier predictions shows improvements of 28.02% and 40.36% respectively comparing with using day-ahead prediction along.

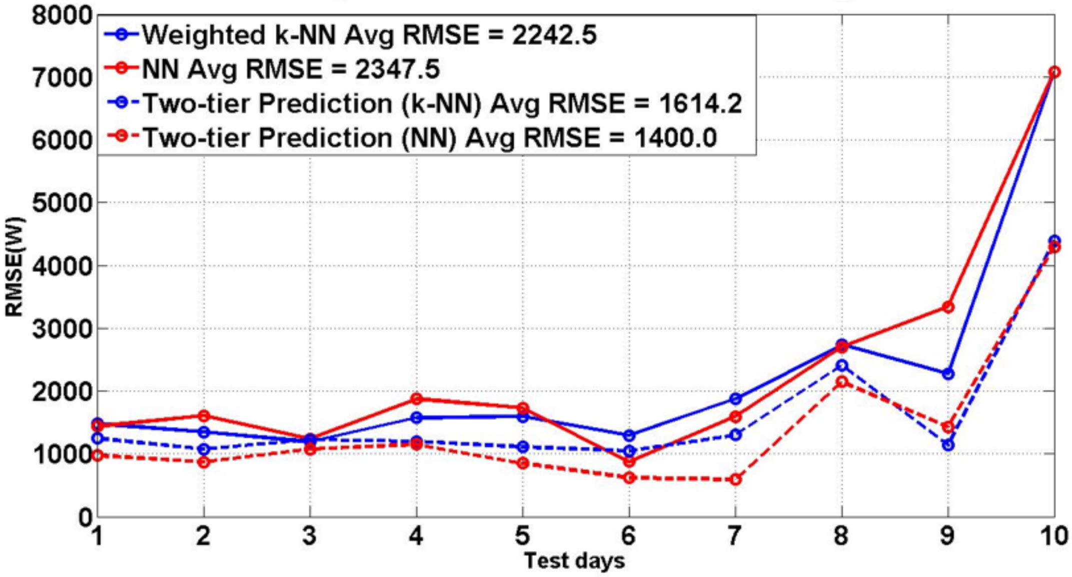

Figure 5-2 RMSE comparison between different forecast algorithms

Besides the overall performance of the prediction, it is desirable to have a closer look on how the prediction methods work in one particular test day. Figure 5-3 shows the comparison results of different prediction methods in a sunny day. The results are separated into two figures, each of which makes the comparison of using day-ahead prediction only with its corresponding two-tier prediction. It is observed that the day-ahead prediction of no matter weighted k-NN or NN aligns with the real power measurement pretty well. However, two-tier prediction further approaches the real measurement with some low frequency noise. Noted that as the sampling frequency is low and we are filtering out the high frequency component within the bandwidth of half of the sampling frequency, some observable overshoots are in the two-tier prediction method. Theoretically, the prediction results can be further improved with by increasing the sampling frequency. Improvements of 30.34% and 51.96% are made respectively with the two-tier prediction.

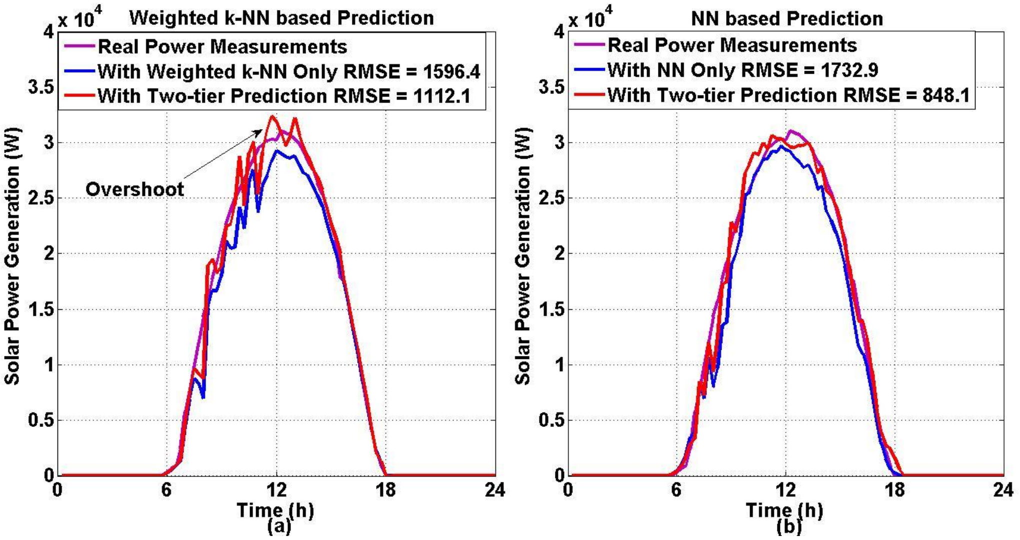

Figure 5-3 RMSE comparisons in a sunny day. (a) comparisons with the day-ahead forecast using weighted k-NN, (b) comparisons with day-ahead forecast using NN

Apart from the observation of prediction results on a sunny day, it is also interesting to see how different prediction methods work on a cloudy day. Figure 5-4 plotted the comparison in a cloudy day. The day-ahead prediction of weighted k-NN and NN are poor as cloudy days introduces more random behaviors. However, with the proposed two-tier prediction method, the predicted value actually approaches the real measurements well. It picks up the low frequency residual of the real measurements and day-ahead predictions. Noted that it still exists undershoot in the prediction partly resulted in the limited bandwidth. The overshoot part below zero is set to zero in the two-tier prediction methods, so there is a sharp drop in two-tier prediction curve when it is close to zero. Figure 5-4 shows two-tier predictions achieves 37.87% and 39.37% relative improvements and 2679.2 and 2788.7 absolute improvements on RMSE over the day-ahead prediction along.

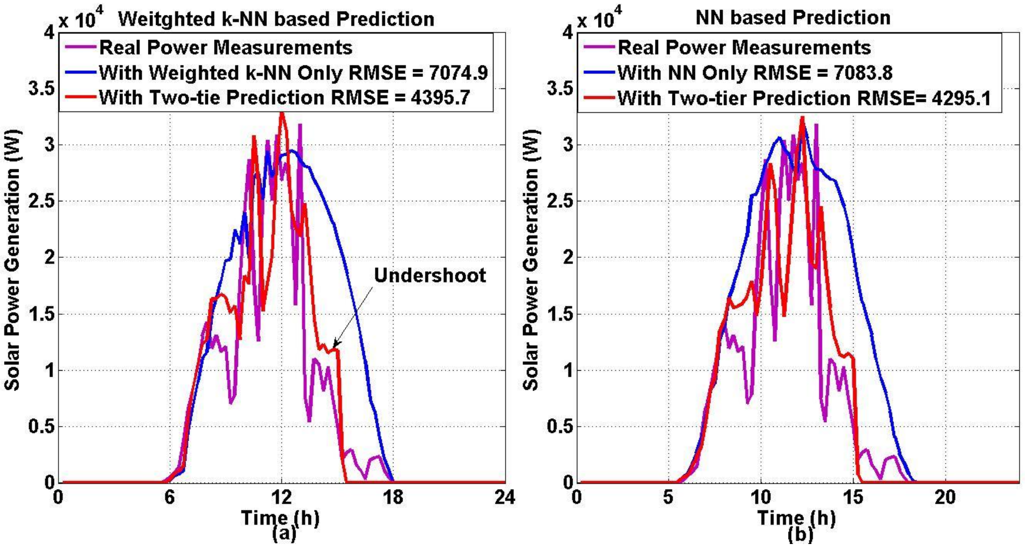

Figure 5-4 RMSE comparisons in a cloudy day. (a) comparisons with the day-ahead forecast using weighted k-NN, (b) comparisons with day-ahead forecast using NN

It is observed that the local-tier prediction works with both global-tier prediction methods. Using global-tier day-ahead prediction along, the weighted k-NN and NN generates similar prediction accuracy. However, NN based two-tier prediction generally outperforms its weighted k-NN counterpart no matter for test-day average or specific sunny/cloudy day. The difference between the two may result from the nature of the two algorithms: NN nonlinearly approximates solar generation curve while weighted k-NN is a linear combination of historical data. Tough they generates same level of error in global-tier, NN introduces less high frequency error compared with weighted k-NN. Given that the local-tier correction filters out high frequency error and is essentially a low frequency compensator, then it explains NN based two-tier prediction's better performance.

5.5 Summary

In this chapter, the problem of solar power prediction with limited sensing resource is described and analyzed. We propose a two-tier adaptive prediction that combines the global-tier day-ahead predictions with local real-time residual analysis. Two heuristic day-ahead prediction methods, weighted k-NN and NN, are investigated in global-tier. In local-tier prediction, it adaptively updates the global-tier prediction with low frequency residual components. The proposed method is evaluated with solar generations in UCLA microgrid testbed. Experimental results demonstrate the effectiveness of the proposed two-tier adaptive solar prediction. Furthermore, case studies in typical sunny and cloudy days are carried out, which shows that the proposed method is particularly effective in days when solar generation is unstable. Finally, it is observed that though weighted k-NN and NN achieve similar accuracy in global-tier, NN based two-tier prediction generally outperforms its weighted k-NN based counterpart. Comparisons and analysis of the differences shed light on global-tier algorithm design: select algorithms that have smaller high frequency errors.

6 Implementations and Demonstrations

This chapter introduces the implementation of two V2G prototypes. The platform is of significance importance as it distinguished from most of V2G research and demonstrates the concept of V2G using commercial a commercial EV.

6.1 Introduction

Researchers have long found the value of V2G in supporting the power grid. Examples of such applications include reactive power compensation, integration with renewable energy and VRs. Among these researchers, Kisacikoglu et al proposed bidirectional V2G charger architecture that utilizes the dc-link capacitor for reactive power compensation. Simulation results showed that the proposed V2G charger has better performance in harmonics and less demand in dc-link capacitors [128]. Lam et al studied replacing traditional VR services with V2G. Simulation was carried out to estimate the appropriate V2G capacity for regulation services [129]. Soares et al simulated a 2000 V2G in IEEE 33 bus distribution network to study the resource scheduling with particle swarm optimization [130]. However, none of the above researchers built real V2G platform for test and verification. Taking into account some unexpected problems, for example long response time, limited output power and V2G dynamics, the proposed ideas may fail to work. Therefore, it is of primary importance to design and implement a V2G capable platform.

Apart from V2G, Vehicle-to-Home (V2H) is another research area within the domain of bidirectional power flow that addresses the problem of AC load support. V2H describes a scenario that output electrical power of EV is not synchronized to the power grid, but instead it provides backup power for islanded AC load [131]. Tuttle et al simulated a household setup of photovoltaic (PV) generation and V2H, which is capable of creating an off-grid microgrid that has sufficient energy support, safety disconnects and VR [132]. Turker et al proposed a strategy targeting at minimizing the energy cost for a household taking into account the V2H and driving pattern of the EV [133]. It would be more solid if the proposed high level control strategies be tested in a cost efficient V2H platform.

Most of existing literatures on V2H and V2G verified proposed ideas with simulation, a few other literatures attempted to setup platforms which replace EVs with battery packs for verification. Ota et al are among those a few researchers who implemented an off-board charger for V2G using battery packs [134]. The work is of great pioneer value but improvements could be made on remote smart control, V2H capability, DC load support, etc. Some of the pilot V2G projects carried out in the United States use highly customized EVs [135] [136]. But when implementing V2H/V2G, especially on large scale, commercialized EVs are the best candidates for such purpose. As most of the EVs on the road are commercialized models, using highly customized EVs or battery backs to verify V2H/V2G ideas cannot reveal the real difficulties sit on the road of future large scale V2H/V2G.

This chapter is concerned with design and implementation of a hybrid V2H/V2G platform and a V2G/G2V bidirectional charging system, primarily for Demand Response (DR) in distribution network. The proposed platforms aim at utilizing commercialized EV model as testbeds. Widely accepted industrial standards, i.e. CHAdeMO and SunSpec are used to achieve remote smart control of V2G. The contribution of the chapter is three-fold: first, to the best of the author's knowledge, we prototyped the first V2G systems that utilizes commercialized EV and standard communication protocol, which shed light on how V2G needs to be performed on a large scale. Second, the V2H/V2G platform has been designed to drive critical DC load, which increases the versatility of the testbed. Finally, the system is remotely controllable, allowing it to receive and respond to remote control signals. As a result, the proposed system can be used to test out a lot of ideas mentioned in the above literatures.

The remainder of this chapter is organized as follows: Section 6.2 articulate the system design, in which system architecture, CHAdeMO communication, and SunSpec communication are discussed. Section 6.3 presents the V2G/G2V bidirectional charging system design. It is followed by prototyping implementation in Section 6.4. The simulation and implementation results are presented and further analyzed in the same section. Finally, conclusions are drawn in Section 6.5.

6.2 V2H/V2G System Architecture

This section describes and analyzes the design of the proposed hybrid V2H/V2G system from both hardware and software aspects. It further introduced the communication protocols, i.e. CHAdeMO and SunSpec, used in the hybrid system.

6.2.1 High Level Hardware Architecture

The design of the V2H/V2G hardware system includes the following three objectives:

- The hybrid system targets to use commercially available EV as testbed to perform V2H/V2G.
- The designed system could support critical DC load such as DC motors. It not only increases the diversity of the system, but also takes into account the real application in household scenario where some appliances are on DC.
- Remote control and can be performed and the system is able to respond to DR signals sent from an aggregator.

With these design considerations in mind, the hybrid system hardware architecture is shown in Figure 6-1. Mitsubishi MiEV is chosen as the EV testbed for this testbed, because it is a popular commercialized EV model which allows DC charging/discharging through CHAdeMO port, which will be explored in further detail later. The system is a combination of both power flow and signal flow. For power flow, the electrical energy stored inside the Mitsubishi MiEV is converted to AC through a DC/AC Converter. This is the V2H part of the system. This port can drive local islanded AC load. It is followed by an AC/DC converter in the second level. The output of this level is designed to drive critical DC load. Finally, the energy goes through a grid-tie inverter and is synchronized to power grid, which is the V2G part of the hybrid system.

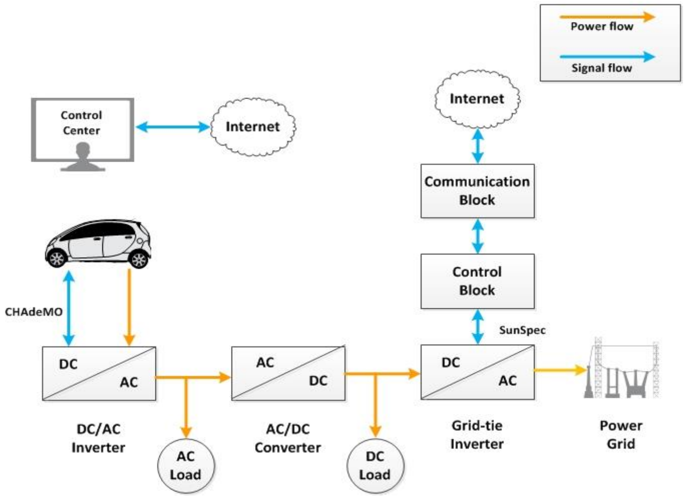

Figure 6-1 Proposed V2H/V2G hybrid system hardware architecture

Unlike power flow which is one-way, the signal flow of the system is all bidirectional. It is consists of two separated parts: information exchange between EV and the first level DC/AC inverter and control between control center and the third level DC/AC inverter. The corresponding communication protocols are CHAdeMO and SunSpec respectively. The details of the two mentioned protocols will be discussed in the following two sections.

6.2.2 High Level Software Architecture

On software side, hierarchical structure is a preferred architecture. It provides more design freedom within each level. Figure 6-2 shows software architecture for the same system. The software has three-layer architecture with user/aggregator layer as the upper layer, power control layer as the lower layer and application layer sits in the middle. The upper two layers are located in the control center which may have a long physical distance from the V2H/V2G hardware field. The lower power control layer is to be implemented on the hardware. The hierarchical design will provide the upper layers with interfaces and each layer may be written in different programming languages or run under different environments. The benefits of this design also allow programmers to focus on each layer rather than handling the whole design flow.

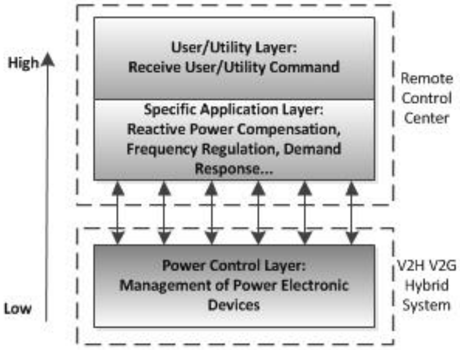

Figure 6-2 Proposed V2H/V2G hybrid system software architecture

Three layers of the system handle entirely different functions. The highest user/aggregator layer receives commands from utility and decides if V2H/V2G needs to be activated. In case multiple EVs are available for V2H/V2G, this layer will decide which EV will perform V2H/V2G based on the information of SoC, user incentives, etc. After the system decides V2H/V2G needs to be performed, the user/aggregator layer will call the functions provided by application layer. Some important applications can be performed such as reactive power compensation, frequency regulation and DR. According to the application the system chooses, it will need to adjust the output voltage profile of the last level inverter. Finally, functions in power controlled layer are called by its upper layer to change the control signals of each transistor in the circuit. On the other hand, when the system needs to read or monitor voltage or current profile of V2H/V2G, the process is still calling a function with needed return values from the highest layer.

6.2.3 CHAdeMO Communication

Communication between EVSE and EV has always been an obstacle in the implementation of V2H/V2G, which partly explains why little literature uses commercialized EV models for V2H/V2G. Before the start of discharging of battery packs on the EV, the EVSE has to communicate with EV’s Battery Management System (BMS) to inform the EV batteries to discharge.

Several protocols are developed for communication between EV and EVSE, among which CHAdeMO is widely used for DC off-board fast charging [64]. The protocol standardized both hardware interfaces and data exchange format in fast charging. With the same data structure and hardware interface, CHAdeMO can be further developed and used in discharging as well. As CHAdeMO connector injects power directly to the battery packs on EV, the current bypasses the on-board single-directional inverter, making it possible of the bidirectional power flow. It is also the standard interface on the testbed setup in this chapter, i.e. Mitsubishi MiEV.

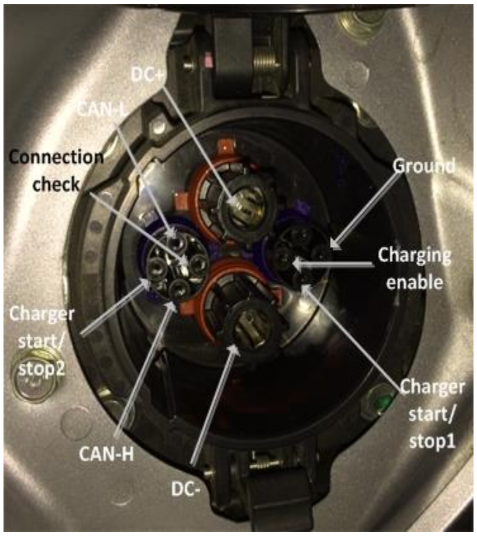

Figure 6-3 Layout of CHAdeMO port on Mitsubishi MiEV

Figure 6-3 shows hardware layout of a CHAdeMO connector. It has nine active connections which can be categorized into three different groups. The DC+ and DC- provide the DC link to charge and discharge the EV. CAN-H and CAN-L consist of communication channels for data exchange between EV and EVSE. On CAN bus, each data frame is transmitted every 100ms. The data frame starts with an ID indicating its functionality and followed by contents. The rest of the connections are for hand shaking and safety check before charging and discharging starts.

6.2.4 SunSpec Communication

Apart from the communication between EV and EVSE, control center and inverter need to exchange information for the purpose of remote monitor and control. The communication between the control center and inverter is implemented on an Ethernet to Modbus device with SunSpec standard.

The SunSpec standard, initially designed for PV, provides an open protocol to allow PVs, inverters, meters and environmental measurement devices to communicate on a single standard [137]. The benefits of the SunSpec standard include reduced engineering time and the need for customizations. It also results in faster deployment time and significant cost reductions, which makes SunSpec protocol optimal candidate for the proposed system.

Figure 6-4 illustrates how the SunSpec standard addresses the standardization of interconnected devices. There are three components in the SunSpec system: SunSpec devices, Supervisory Control And Data Acquisition (SCADA) and control center respectively. As shown in the figure, the inverter, meter, and charge controller are the SunSpec compliant devices. They communicate with SCADA through multiple physical layer protocols including but not limited to Zigbee, RS485, TCP/IP and Modbus following SunSpec standard. The SCADA serves as monitor and data logger for all SunSpec compliant devices. On the other side of the SCADA, the control center, which resides in the cloud, will perform the upper level algorithms mentioned in Figure 6-2 based on the information acquired by SCADA. The control commands will be sent to SunSpec devices through SCADA following SunSpec protocol.

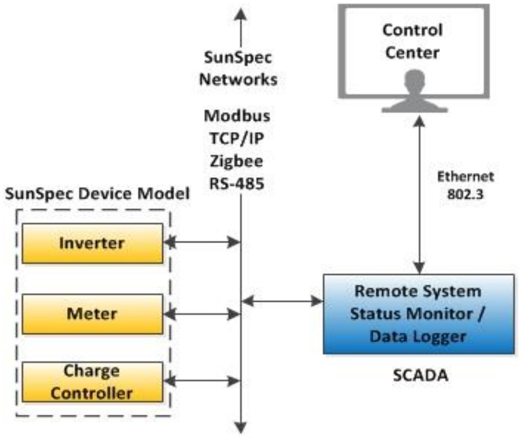

Figure 6-4 SunSpec protocol architecture

6.3 V2G/G2V Bidirectional Charging System Architecture

The previous section introduces the V2H/V2G platform. In this section, we are going to present the V2G/G2V bidirectional platform. The hardware settings of this V2H/V2G platform remains similar to

6.3.1 High Level Hardware Architecture

The physical setup is shown in Figure 6-5. It shows a conceptual design of the proposed V2G bidirectional charging system. It takes advantage of the Mitsubishi MiEV Power Box and utilizes the MiEV as a testbed. The proposed system synchronizes the power stored in the Mitsubishi MiEV with the grid and sends power back into the grid.

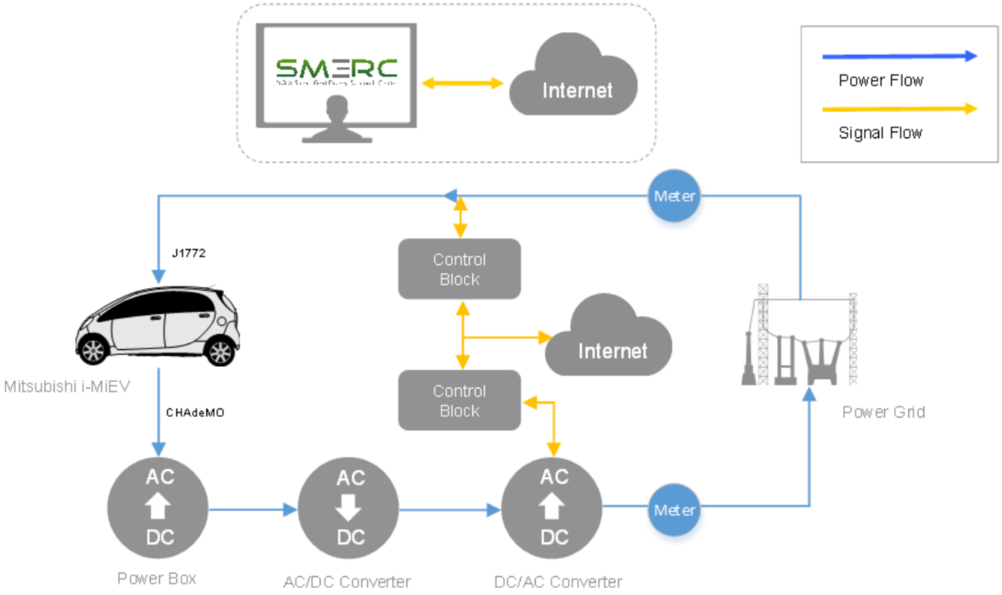

Figure 6-5 Bidirectional charging architecture

The Mitsubishi MiEV is equipped with two ports that supports J1772 and CHAdeMO separately. The CHAdeMO port is capable of feeding back power to the grid and therefore is used for V2G demonstration. The J-1772 port is used for G2V operation. The system has a web interface to monitor and control the charging/discharging status of this platform. All measured data are posted to the web interface and stored in database for analysis. There are two reasons that another pair of AC/DC Converter and DC/AC inverter is added in the platform. First, the power fed back by Mitsubishi power box is not grid-tied and therefore if we directly connect it to the grid, there will be a system collapse. Also, the Mitsubishi Power Box use a proprietary standard and therefore control of current could not be realized. Without information of the car, we could not properly control the charging/discharging schedules and therefore another layer of controllable DC/AC inverter is included in the system.

6.3.2 High Level Software Architecture

A software is designed for the bidirectional charging system as shown in Figure 6-6. As shown in the figure, the system is composed of two parts and programmed in three languages/platforms. On server side, the control flow is managed by threads, it keeps waiting for user input while execute user command. The remote controllers are responsible for executing the commands from the server side.

Additional attentions are given to ensure the communication robustness. It is very often that the wireless communication between sever and remote controller is so weak such that system will encounter communication failure. In this case, the system needs to identify the failure and reacts to the failure. In the case of failure, another command will be sent to remote controllers.

The communication failures happen most frequently on G2V side. According to statistics, 5-30% of the commands sent to the box cannot be received. The system now has functions that detect the failure. However, if the test field is equipped with better communication infrastructures, the instances of communication failures can be significantly cut down.

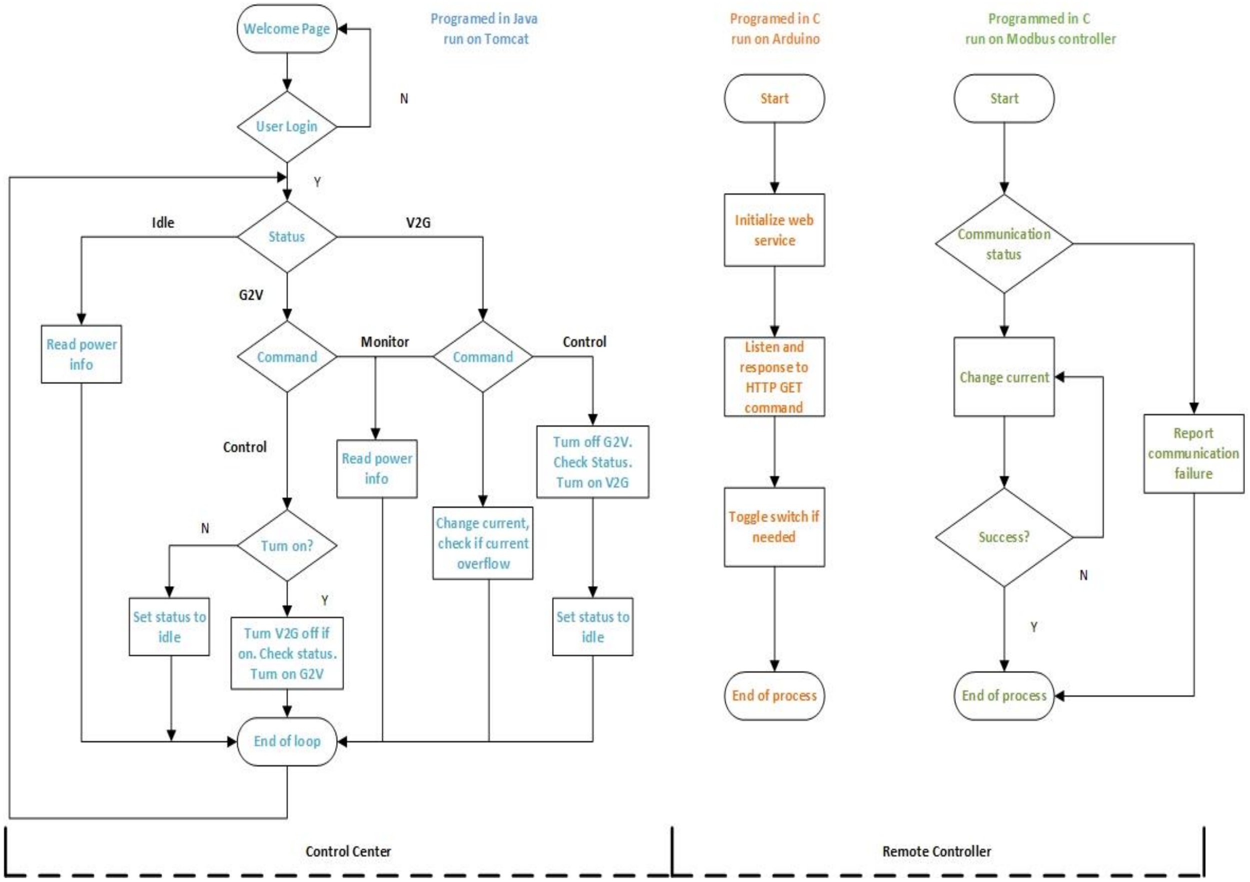

Figure 6-6 V2G/G2V bidirectional charging software flow

As shown in Figure 6-7, user can use automatic operation by entering estimated leave time and price input, and manual operation by just turning on/off the G2V and V2G. For V2G, user can change current to adjust V2G power. By pressing refresh bottom, user can get the up to date information of the charging status. The diagram in the bottom of the figure shows the most recent historical active power. On metering side, voltage, current, frequency, active power, apparent power, power factor and energy are measured on both V2G and G2V side. User can also submit show history command through the user interface.

SETTINGS and RECORDS

Item	Interface	Operation
Leave time	HH 15 MM 0	Change
Sell Limit	$ 0.1	Change
History Settings	Pick Day Show Hours	SHOW
Command	REFRESH Start	
Cost	$ 0.2106	
Energy	1.413 kWh	
Expected Cost	$ 0.0	
Expected Energy	0.0 kWh	
Item	**G2V**	**V2G**
Manual Stop	G2V Start	V2G Start
Manual Start	G2V Stop	V2G Stop
V2G Current		5 SUBMIT

V2G REAL-TIME DATA

Item	Value
Voltage	0.0 V
Current	0.0 A
Frequency	0.0 Hz
Active Power	0.0 W
Apparent Power	0.0 VA
Power Factor	1.0

G2V REAL-TIME DATA

Item	Value
Voltage	120.39 V
Current	0.0 A
Frequency	59.98 Hz
Active Power	0.0 W
Apparent Power	0.0 VA
Power Factor	1.0

Figure 6-7 V2G/G2V bidirectional charging user interface

6.4 Implementation Results

6.4.1 Hardware Setup

Experimental V2H/V2G hybrid system is built based on the architecture proposed in Figure 6-1. Table 6-1 summarizes the key parameters for the proposed testbed. The maximum power output that can be achieved by the testbed is 1.3 kW. The overall efficiency and dynamic behavior will be discussed in the remainder of this section.

Table 6-1 Specifications of testbed

EV Model	Mitsubishi MiEV
Battery	330 Volt, 16 kWh
Connector Protocol	CHAdeMO
Maximum Power	1.3 kW

Figure 6-8 demonstrates the setup of the proposed V2H/V2G hybrid system. A Mitsubishi MiEV is served as the testbed with a rated battery voltage of 330Vac and capacity of 16 kWh. As shown in the figure, it is connected with a CHAdeMO connector. The other end of the connector is connected to the DC/AC inverter. The output of the DC/AC inverter is not synchronized to the grid but is capable of supporting islanded AC load. The DC/AC inverter is cascaded with AC/DC converter with a rated output of 48Vdc. The output of the converter is able to support critical DC load. And finally, the power flow goes through a grid-tie inverter. A SunSpec compliant SCADA is connected with the inverter for remote control and monitor. The controller is further connected to the Ethernet and connects to the control center on the cloud. On grid side, for safety considerations, surge protectors are attached to the inverter before it is connected the grid. The rated overall power that can be extracted from the MiEV is no more than 1.5 kW, which is limited by the DC/AC inverter. As shown in the figure, the proposed platform is able to perform V2H on the output of DC/AC inverter while V2G on the grid-tie inverter. The system can also support critical DC load at the output of AC/DC converter.

Figure 6-9 demonstrates the experiment setup of the proposed V2G/G2V bidirectional charging system. As shown in the figure, it is connected with a CHAdeMO connector. The other end of the connector is connected to the DC/AC inverter. The output of the DC/AC inverter is synchronized to the grid. On grid side, for safety considerations, surge protectors are attached to the inverter before it is connected the grid. The rated overall power that can be extracted from the MiEV is no more than 1.5 kW, which is limited by the DC/AC inverter. On the G2V end, J-1772 plug is plugged into the AC charging port of the EV. The design follows the previously designed schematics provided in Figure 6-5.

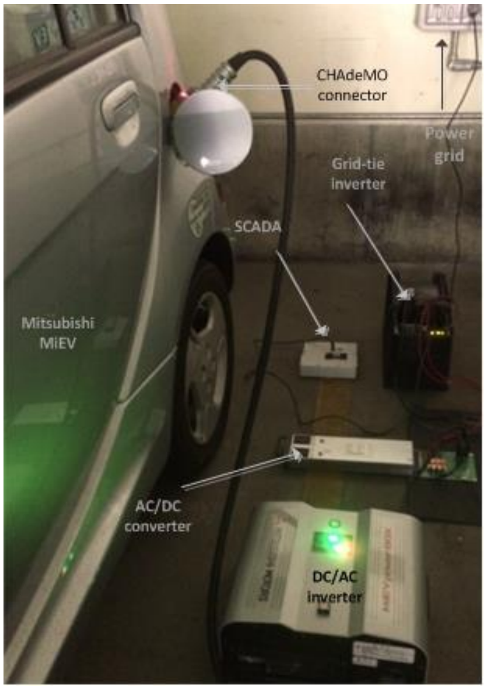

Figure 6-8 Experimental setup of V2H/V2G hybrid system

Figure 6-9 Experimental setup of V2G/G2V bidirectional charging system

Two tests are run in order to validate the designed V2H/V2G and V2G/G2V system. The first test is a measurement on AC current sent to the grid under different operations. It shows the dynamics of the system or how quickly the system can respond to the remote control signal. RMS value is used to evaluate AC current. The Hall Effect sensor measures and averages out the sampled measurements over a second. Due to the limitation of the AC current sensor and the circuit noise, the accuracy is within ±0.1A. The second test is on DC. The DC test measures the DC current on the output of the AC/DC converter when the system is driving a critical DC load while performing V2G. The DC test intends to show the robustness of the designed system as the system is under different operations. The measurement on DC test is sampled at 2.5GHz. It inevitably introduces environmental noise into the system. Therefore, a first order filter will be used to filter out the measurement noise.

6.4.2 System Performance

Figure 6-10 presents the transient state of AC current in RMS value when the system is under different operations. The measurement is performed at the output of grid-tie inverter. The grid-tie inverter is remotely monitored and controlled. The remote control current is initially set to 5A and later increased to 8A. As shown in the figure, under initial stable operation, the output current of the grid-tie inverter is at 4A though the intended V2G current is set to 5A. The 1A difference results from two facts: first of all, V2G can be only performed within local distribution network. The power sent back to the power grid cannot transmit back to the transmission network. The power cannot go through circuit panel, not to mention most of transformers prevent bidirectional power flow. Secondly, distribution network has impedance and resistance at comparable level. The inverter changes it voltage amplitude and phase angle to inject current into the power grid. When there is not enough consumption in the local distribution grid, the voltage in the distribution grid stays at the nominal voltage. The V2G grid-tie inverter has to elevate its output voltage in order to inject the desired current, which reaches the upper limit of the output voltage for the V2G grid-tie inverter. Therefore, at the initial stable operation, there is a 1A difference between the desired value and measured value.

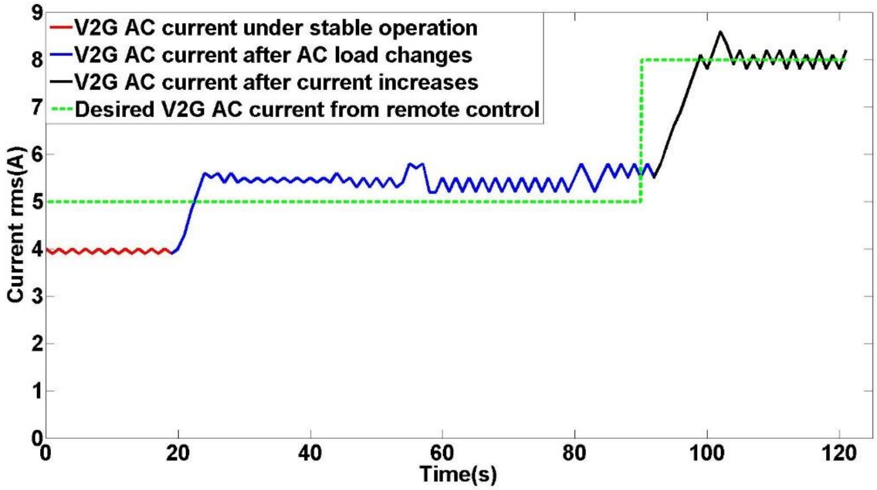

Figure 6-10 Transient state of AC load changes and V2G current increases

After operating in stable stage, the authors increase the AC load in the local distribution grid by turning on heavy duty heater for more than 2 kW. The grid voltage drops because of insufficient power supply and consequently the difference between V2G grid-tie inverter and grid voltage become larger. As expected, the output current of the V2G grid-tie inverter reaches the desired value of the current. It operates in stable state for around 75s. The zigzag current is due to sensor inaccuracy as well as slight load change from the distribution network. As load changes, the closed-loop inverter always maintains it output at 5A. The error between desired and measured current is within a reasonable tolerance range.

In the last part of this experiment, a DR signal to increase the current from 5A to 8A is sent to the inverter through SCADA. As shown in Figure 6-10, hybrid system responds to the command and increases its current to 8A. There is about 3s between the time a command is sent from the server and the time the current signal starts to ramp up. This delay primarily results from the communication. It is followed by a 15s ramp up which is caused by the characteristic of the battery and power electronic devices. The delays are characterized so that the studied V2G application could be considered for bidding into primary control markets.

After the experiment on AC transient state, experiment on DC side is also carried out to demonstrate the flexibility and versatility of the designed V2H/V2G system. At the output of AC/DC converter a critical DC load is connected to the system. In this chapter, a brush permanent magnetic DC motor with a rated voltage of 12-72Vdc is used as the critical load. The instant DC current is measured at the output of the DC/AC inverter where the nominal voltage is 48Vdc.

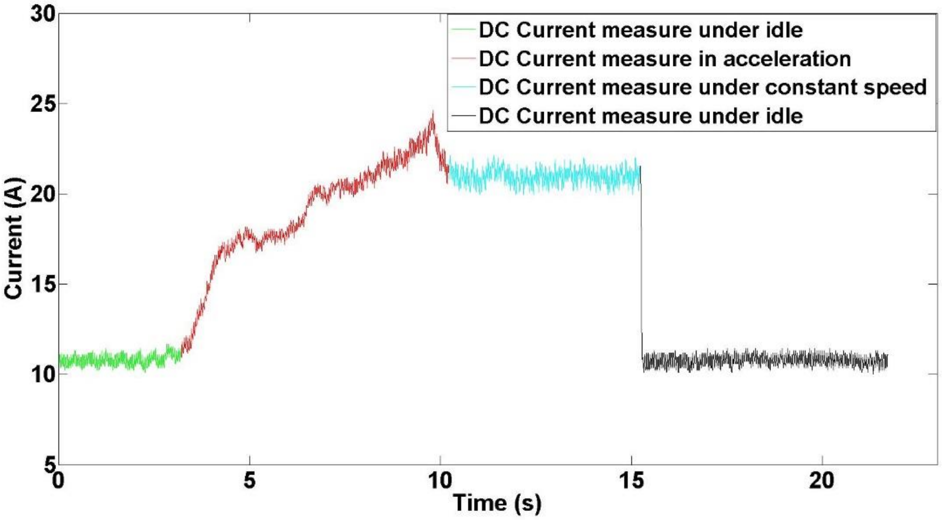

Figure 6-11 Transient state of DC load change with constant V2G power

Figure 6-11 shows the DC transient state under different operations of the DC motor when V2G is performed for 5A on the grid-tie inverter side. The initial current is around 11A when motor is first in idle state. Then the motor is accelerated, the current reaches a maximum of 25A. After reaching its maximum speed, it falls into the constant speed state where the current measurement is around 22A. For the whole process, the V2G is working on 5A on grid-tie inverter side. And finally the motor falls back to idle stage where the 11A current reflects the constant V2G on grid side. This experiment demonstrates the robustness and versatility of the designed system. It is able to support critical DC load while maintaining constant power of V2G.

The above two experiments demonstrate the preciseness of the designed system. If V2H and V2G combined are performed in 1.3 kW range continuously, with a battery capacity of 16 kWh, i.e. the capacity of Mitsubishi MiEV battery, it can achieve continuous V2H/V2G for more than 10 hours. However, it should be noted that the flexibility and versatility is at the expense of system level efficiency. According to the measurement, 1.3 kW power deliveries at V2H stage is only measured at 1.06 kW at the output of V2G stage, having an efficiency of 81.5%.

6.5 Summary

This chapter has proposed a V2H/V2G hybrid system and a V2G/G2V bidirectional charging system that can be remotely controlled and monitored. The commercialized EV model, Mitsubishi MiEV, is utilized as testbed. Widely used CHAdeMO protocol is chosen for communication between EV and EVSE. For communication between SCADA and inverter, SunSpec is implemented as the communication protocol. Experimental results show that the proposed systems support both islanded DC/AC load as well as the power grid. The two systems system can respond to remote DR signal and respond to it within 1.5 kW range. AC and DC test are performed to study the dynamics and robustness of the proposed systems. Experiments also indicate that V2G can only be performed in local distribution network and the performance of V2G depends heavily upon the load profile of the distribution network.

7 Conclusions and Future Work

V2G integration to power grid extents the traditional role of EVs as pure loads to distributed generations. By strategically control the power back feed to the grid at the same time meeting the demands of EV owners, V2G enables a variety of grid applications thus could potentially support the power grids. On the other hand, large scale integration of V2G introduces new challenges, two fundamental questions awaits to be answered for better utilizing the energy stored in the EVs. Firstly, there is no contract signed in real-life that constraints the starting and leaving time of an EV parked at a charging station, nor the total energy that an EV acquires during a bidirectional charging section. The problem of modeling the stochastic nature of EV availabilities and energy demands becomes a crucial research topic in V2G integration. Secondly, as the EV penetration continuous to grow, the control problem scales up quickly, traditional centralized control method may not be effective anymore. The problem of scalability becomes another critical area of research in V2G integration. This dissertation proposes a stochastic modeling method to account for the stochastic nature of the EVs in Chapter 2. KDE is applied to model the uncertainties of EVs, and SAA is utilized to numerically approximate the studied problem. Numerical results using the real-life building, solar and EV data shows the merits of the proposed method compared to its traditional deterministic counterpart. Note that the same proposed method could model system with uncertainties not limited to EVs, but also renewable generations, load, and etc. In Chapter 3, we give an answer to the scalability problem, by developing an ADMM based DSM. The proposed DSM takes into account the network and nodal cost in distribution networks. It dispatches the centralized computational burden to distributed nodes. By communicating Lagrangian multipliers instead of power/energy information, the ADMM based DSM protects the end user privacies. A modified IEEE 13-bus system and real-life collected EV data is utilized to demonstrate the correctness and properties of the proposed DSM. Numerical results shows that the ADMM based DSM can iteratively approximates the control solved in a centralized manner. And it can address large scale V2G integration problems which traditional centralized manner fails to handle. The proposed distributed method can be potentially applied in other applications in power grid as long as the problem is convex and continuous.

Chapter 4 and 5 serve as complements to Chapter 2 and 3. In Chapter 4, an important problem is studied, in which the control time-step is much smaller than the previous two chapter and system dynamics becomes phenomenon. We show the dynamics of V2G load sharing in the context of a microgrid. A load sharing control strategy that takes into the EV drivers’ preferences is proposed and verified. The active power can be shared proportionally between the V2G EVs. The difficulty in reactive power control is also analyzed and discussed. Chapter 5 bridges an important gap between reality and problems studied in Chapter 2 and 3. In most of the energy management problems, load and generation are always assumed to be known, while in reality they needs to be predicted. This dissertation proposes a two-tier prediction method for predicting uncertainties in systems. In global-tier, the two machine learning methods are used, which is refined by the computational economic local-tier real-time corrections. The proposed prediction method is verified using a solar generation installed on UCLA campus. Numerical results shows that by combining day-ahead predictions with real-time measurement using the proposed two-tier prediction method, the prediction can be larges cut off. It is therefore “safe” to make the assumptions in Chapter 2 and 3 that some the uncertainties in the system (such as loads) is known. The proposed perdition method can be applied for other types of uncertainty predictions in power grids.

Different than most of the existing literatures that studied the problem V2G integration to power grids, this dissertation presents the design and implementation of two V2G platforms, i.e. V2H/V2G hybrid system and V2G/G2V bidirectional charging system, utilizing a commercialized vehicle. We present the hardware design considerations and software architectures. Two tests are run to evaluate the performance of the prototype.

In terms of future research, there is a lot to explore. One of the key related area is how to handle V2G uncertainty in a robust and effective manner? This dissertation addresses the system uncertainties without considering the worst-case scenario. However, in military or hospital islanded microgrids, worst cast scenarios become critically important. On the other hands, as the EV penetration continuous to grow, much more data is generated and stored. In this dissertation, EV owners’ behaviors are analyzed individually. Therefore, the other key related area of research is effective ways of learning the EV owners aggregated behavior, which will facilitate large scale V2G integration to power grids.

References

[1] International Energy Agency, "Global EV Outlook," 2013.

[2] P. Keith, P. Denholm and A. J. Markel, "Costs and emissions associated with plug-in hybrid electric vehicle charging in the Xcel Energy Colorado service territory," 2007.

[3] T. Tammy, M. Webber and D. T. Allen, "Air quality impacts of using overnight electricity generation to charge plug-in hybrid electric vehicles for daytime use," *Environmental Research Letters,* vol. 4, no. 1, p. 014002, 2009.

[4] R. McCarthy and C. Yang, "Determining marginal electricity for near-term plug-in and fuel cell vehicle demands in California: Impacts on vehicle greenhouse gas emissions," *Journal of Power Sources,* vol. 195, no. 7, pp. 2099-2109, 2010.

[5] "Nissan Leaf," [Online]. Available: http://en.wikipedia.org/wiki/Nissan_Leaf.

[6] "Cherolet Volt," [Online]. Available: http://en.wikipedia.org/wiki/Chevrolet_Volt.

[7] "Tesla Model S," [Online]. Available: http://en.wikipedia.org/wiki/Tesla_Model_S.

[8] "U.S Energy Infromation Administration," 2015. [Online]. Available: https://www.eia.gov/tools/faqs/faq.cfm?id=97&t=3.

[9] "Charging Station," [Online]. Available: http://en.wikipedia.org/wiki/Charging_station.

[10] L. Du, C. Liu, A. Tang, Y. Zhang, Y. Li, K. Cheung and M. Chang, "Invited-Airtouch: a novel single layer 3D touch sensing system for human/mobile devices interactions," in

ACM Proceedings of the 53rd Annual Design Automation Conference, 2016.

[11] Q. Zhang, X. Yang, Y. Zhou, L. Wang and X. Guo, "A wireless solution for greenhouse monitoring and control system based on ZigBee technology," *Journal of Zhejiang University Science A*, vol. 8, no. 10, pp. 1584-1587, 2007.

[12] A. Tang, F. Hsiao, Y. Kim, L. Du, L. Kong, G. Virbila, Y. Kuan, C. Lee, G. Chattopadhyay, N. Chahat and T. Reck, "A 95 GHz centimeter scale precision confined pathway system-on-chip navigation processor for autonomous vehicles in 65nm CMOS," in *IEEE MTT-S International Microwave Symposium*, 2015.

[13] H. Farhangi, "The path of the smart grid," *IEEE power and energy magazine*, vol. 8, no. 1, pp. 18-28, 2010.

[14] N. Batista, R. Melício, J. Matias and J. Catalão, "Photovoltaic and wind energy systems monitoring and building/home energy management using ZigBee devices within a smart grid," *Energy*, vol. 49, pp. 306-315, 2013.

[15] D. Wang, Z. Tao, J. Zhang and A. Abouzeid, "RPL based routing for advanced metering infrastructure in smart grid," in *IEEE International Conference on Communications Workshops*, 2010.

[16] C. Hill, M. Such, D. Chen, J. Gonzalez and W. Grady, "Battery energy storage for enabling integration of distributed solar power generation," *IEEE Transactions on smart grid*, vol. 3, no. 2, pp. 850-857, 2012.

[17] J. J. Grainger, Power System Analysis, McGraw-Hill Education, 1994.

[18] C.-Y. Chung, E. Youn, J. Chynoweth, C. Qiu, C.-C. Chu and R. Gadh, "Safety design for smart Electric Vehicle charging with current and multiplexing control," in *Smart Grid Communications (SmartGridComm), 2013 IEEE International Conference on.*, 2013.

[19] S. Mal, A. Chattopadhyay, A. Yang and R. Gadh, "Electric vehicle smart charging and vehicle-to-grid operation," *International Journal of Parallel, Emergent and Distributed Systems,* vol. 27, no. 3, pp. 249-265, 2012.

[20] Y. He, B. Venkatesh and L. Guan, "Optimal scheduling for charging and discharging of electric vehicles," *IEEE transactions on smart grid,* vol. 3, no. 3, pp. 1095-1105, 2012.

[21] J. Hu, S. You, M. Lind and J. Østergaard, "Coordinated charging of electric vehicles for congestion prevention in the distribution grid," *IEEE Transactions on Smart Grid,* vol. 5, no. 2, pp. 703-711, 2014.

[22] W. Kempton and S. Letendre, "Electric Vehicles as a New Source of Power for Electric Utilities," *Transportation Research,* vol. 2, no. 3, pp. 157-175, 1997.

[23] S. Letendre and W. Kempton, "The V2G Concept: A New Model for Power?," *Public Utilities Fortnightly,* vol. 140, no. 4, pp. 16-26, 2002.

[24] W. Kempton and J. Tomić, "Vehicle-to-grid power fundamentals: Calculating capacity and net revenue," *Journal of power sources,* vol. 144, no. 1, pp. 268-279, 2005.

[25] G. Strbac, "Demand side management: Benefits and challenges," *Energy policy,* vol. 36, no. 12, pp. 4419-4426, 2008.

[26] D. Wang, D. Kalathil, K. Poolla and X. Guan, "Coordination of wind power and flexible load through demand response options," in *IEEE Conference on Decision and Control (CDC)*, 2015.

[27] A. Mohsenian-Rad, V. Wong, J. Jatskevich, R. Schober and A. Leon-Garcia, "Autonomous demand-side management based on game-theoretic energy consumption scheduling for the future smart grid," *IEEE transactions on Smart Grid,* vol. 1, no. 3, pp. 320-331, 2010.

[28] O. Erdinc, N. Paterakis, T. Mendes, A. Bakirtzis and J. Catalao, "Smart Household Operation Considering Bi-Directional EV and ESS Utilization by Real-Time Pricing-Based DR," *IEEE Transactions on Smart Grid,* vol. 6, no. 3, pp. 1281-1291, 2015.

[29] P. Mesarić and S. Krajcar, "Home Demand Side Management Integrated with Electric Vehicles and Renewable Energy Sources," *Energy and Buildings,* pp. 1-9, 2015.

[30] A. Chabaud, J. Eynard and S. Grieu, "A new approach to energy resources management in a grid-connected building equipped with energy production and storage systems: A case study in the south of France," *Energy and Buildings,* vol. 99, pp. 9-31, 2015.

[31] Y. Wang, B. Wang, T. Zhang, H. Nazaripouya, C. Chu and R. Gadh, "Optimal energy management for Microgrid with stationary and mobile storages," in *IEEE/PES Transmission and Distribution Conference and Exposition (T&D)*, 2016.

[32] A. Saber and G. Venayagamoorthy, "Optimization of vehicle-to-grid scheduling in constrained parking lots," in *IEEE Power & Energy Society General Meeting*, 2009.

[33] C. Guille and G. Gross, "A conceptual framework for the vehicle-to-grid (V2G)

implementation," *Energy policy,* vol. 37, no. 11, pp. 4379-4390, 2009.

[34] X. Bai and W. Qiao, "Robust Optimization for Bidirectional Dispatch Coordination of Large-Scale V2G," *IEEE Transactions on Smart Grid,* vol. 6, no. 4, pp. 1944-1954, 2015.

[35] Y. Wang, B. Wang, C. Chu, H. Pota and R. Gadh, "Energy management for a commercial building microgrid with stationary and mobile battery storage," *Energy and Buildings,* vol. 116, pp. 141-150, 2016.

[36] L. Jian, Y. Zheng, X. Xiao and C. Chan, "Optimal scheduling for vehicle-to-grid operation with stochastic connection of plug-in electric vehicles to smart grid," *Applied Energy,* vol. 146, pp. 150-161, 2015.

[37] Y. Wang, H. Nazaripouya, C.-C. Chu, R. Gadh and H. Pota, "Vehicle-to-grid automatic load sharing with driver preference in micro-grids," in *IEEE PES Innovative Smart Grid Technologies Conference Europe*, 2014.

[38] Y. Wang, B. Wang, R. Huang, C.-C. Chu, H. R. Pota and R. Gadh, "Two-tier prediction of solar power generation with limited sensing resource," in *IEEE PES Transmisson and Distribution Conference and Exposition*, 2016.

[39] Y. Wang, O. Sheikh, B. Hu, C.-C. Chu and R. Gadh, "Integration of V2H/V2G hybrid system for demand response in distribution network," in *IEEE International Conference on Smart Grid Communications,* 2014.

[40] Y. Wang, B. Wang, C.-C. Chu, H. Pota and R. Gadh, "Energy management for a commercial building microgrid with stationary and mobile battery storage," *Energy and*

Buildings, vol. 116, pp. 141-150, 2016.

[41] R. Palma-Behnke, C. Benavides, F. Lanas, B. Severino, L. Reyes, J. Llanos and D. Saez, "A Microgrid Energy Management System Based on the Rolling Horizon Strategy," *IEEE Transactions on Smart Grid,* vol. 4, no. 2, pp. 996-1006, 2013.

[42] D. Wang, X. Guan, J. Wu, P. Li, P. Zan and H. Xu, "Integrated Energy Exchange Scheduling for Multimicrogrid System With Electric Vehicles," *IEEE Transactions on Smart Grid,* vol. 7, no. 4, pp. 1762 - 1774, 2016.

[43] A. Anvari-Moghaddam, H. Monsef and A. Rahimi-Kian, "Cost-effective and comfort-aware residential energy management under different pricing schemes and weather conditions," *Energy and Buildings,* vol. 86, pp. 782-793, 2015.

[44] P. Palensky and D. Dietrich, "Demand Side Management: Demand Response, Intelligent Energy Systems, and Smart Loads," *IEEE Transactions on Industrial Informatics,* vol. 7, no. 3, pp. 381-388, 2011.

[45] Y. Yang, H. Li, A. A., J. Zheng and M. Greenleaf, "Sizing Strategy of Distributed Battery Storage System With High Penetration of Photovoltaic for Voltage Regulation and Peak Load Shaving," *IEEE Transactions on Smart Grid,* vol. 5, no. 2, pp. 982-991, 2014.

[46] S. Lee, B. Kwon and S. Lee, "Joint Energy Management System of Electric Supply and Demand in Houses and Buildings," *IEEE Transactions on Power Systems,* vol. 29, no. 6, pp. 2804-2812, 2014.

[47] S. Mocci, N. Natale, F. Pilo and S. Ruggeri, "Demand side integration in LV smart grids

with multi-agent control system," *Electric Power Systems Research,* vol. 125, pp. 23-33, 2015.

[48] Z. Wang, L. Wang, A. I. Dounis and R. Yang, "Integration of plug-in hybrid electric vehicles into energy and comfort management for smart building," *Energy and Buildings,* vol. 47, pp. 260-266, 2012.

[49] Y. Ota, H. Taniguchi, T. Nakajima, K. Liyanage, J. Baba and A. Yokoyama, "Autonomous Distributed V2G (Vehicle-to-Grid) Satisfying Scheduled Charging," *IEEE Transactions on Smart Grid,* vol. 3, no. 1, pp. 559-564, 2012.

[50] A. Pensini, C. N. Rasmussen and W. Kempton, "Economic analysis of using excess renewable electricity to displace heating fuels," *Applied Energy,* vol. 131, pp. 530-543, 2014.

[51] X. Li, J. Wen and A. Malkawi, "An Operation Optimization and Decision Framework for a Building Cluster with Distributed Energy Systems," *Applied Energy,* vol. 178, pp. 98-109, 2016.

[52] X. Li and J. Wen, "System Identification and Data Fusion for Energy Forecasting in Virtual and Real Buildings," *Energy and Buildings,* vol. 129, pp. 227-237, 2016.

[53] P. Malysz, S. Sirouspour and A. Emadi, "An Optimal Energy Storage Control Strategy for Grid-connected Microgrids," *IEEE Transactions on Smart Grid,* vol. 5, no. 4, pp. 1785-1796, 2014.

[54] Y. Zhang, N. Gatsis and G. Giannakis, "Robust Energy Management for Microgrids With

High-Penetration Renewables," *IEEE Transactions on Sustainable Energy*, vol. 4, no. 4, pp. 944-953, 2013.

[55] Q. Wang, J. Wang and Y. Guan, "Price-Based Unit Commitment With Wind Power Utilization Constraints," *IEEE Transactions on Power Systems,* vol. 28, no. 3, pp. 2718-2726, 2013.

[56] H. T. Nguyen and L. B. Le, "Optimal energy management for building microgrid with constrained renewable energy utilization," in *IEEE International Conference on Smart Grid Communications*, 2014.

[57] P. Garcia, C. Garcia, L. Fernandez, F. Llorens and F. Jurado, "ANFIS-Based Control of a Grid-Connected Hybrid System Integrating Renewable Energies, Hydrogen and Batteries," *IEEE Transactions on Industrial Informatics*, vol. 10, no. 2, pp. 1107-1117, 2014.

[58] O. Erdinc, O. Elma, M. Uzunoglu, U. Selamogullari, B. Vural, E. Ugur, A. Boynuegri and S. Dusmez, "Experimental performance assessment of an online energy management strategy for varying renewable power production suppression," *International Journal of Hydrogen Energy*, vol. 37, no. 6, pp. 4737-4748, 2012.

[59] A. Kavousi-Fard, A. Abunasri, A. Zare and R. Hoseinzadeh, "Impact of plug-in hybrid electric vehicles charging demand on the optimal energy management of renewable micro-grids," *Energy*, vol. 78, pp. 904-915, 2014.

[60] Z. Xu, X. Guan, Q.-S. Jia, J. Wu, D. Wang and S. Chen, "Performance Analysis and Comparison on Energy Storage Devices for Smart Building Energy Management," *IEEE*

Transactions on Smart Grid, vol. 3, no. 4, pp. 2136-2147, 2012.

[61] Conell University Facilities Service, "Real Time Building Utility Use Data," [Online]. Available: http://portal.emcs.cornell.edu/.

[62] SMERC, "Ackerman PV project," [Online]. Available: https://evsmartplug.net/smartgrid/ackerman_pv/.

[63] B. Wang, B. Hu, C. Qiu, P. Chu and R. Gadh, "EV charging algorithm implementation with user price preference," in *IEEE Innovative Smart Grid Technologies Conference*, 2015.

[64] CHAdeMO society, "Basic function of quick charger for the electric vehicle," 2012.

[65] J. Lin, K.-C. Leung and V. Li, "Optimal Scheduling With Vehicle-to-Grid Regulation Service," *IEEE Internet of Things Journal*, vol. 1, no. 6, 2014.

[66] E. Sortomme and M. El-Sharkawi, "Optimal Scheduling of Vehicle-to-Grid Energy and Ancillary Services," *IEEE Transactions on Smart Grid*, vol. 3, no. 1, pp. 351-359, 2012.

[67] C. Zhou, K. Qian, M. Allan and W. Zhou, "Modeling of the Cost of EV Battery Wear Due to V2G Application in Power Systems," *IEEE Transactions on Energy Conversion*, vol. 26, no. 4, pp. 1041-1050, 2011.

[68] D. Wang, J. Coignard, T. Zeng, C. Zhang and S. Saxena, "Quantifying electric vehicle battery degradation from driving vs. vehicle-to-grid services," *Journal of Power Sources*, vol. 332, pp. 193-203, 2016.

[69] A. Shapiro, D. Dentcheva and A. P. Ruszczynski, Lectures on Stochastic Programming: Modeling and Theory, 2nd Edition, SIAM, 2014.

[70] S. Ahmed and A. Shapiro, "The Sample Average Approximation Method for Stochastic Programs With Integer Recourse," ISyE, 2002.

[71] B. W. Silverman, Density estimation for statistics and data analysis, CRC press, 1986.

[72] SAE International, "SAE standard on EV charging connector," 2012.

[73] Nissan Motor Company, "“Vehicle to Home” Electricity Supply System," 2014. [Online]. Available: http://www.nissan-global.com/EN/TECHNOLOGY/OVERVIEW/vehicle_to_home.html.

[74] Gurobi Optimization Inc, 2015. [Online]. Available: http://www.gurobi.com/.

[75] CAISO, "California solar statistics," [Online]. Available: http://www.californiasolarstatistics.ca.gov/.

[76] B. Nykvist and a. M. Nilsson, "Rapidly falling costs of battery packs for electric vehicles," *Nature Climate Change*, vol. 5, no. 4, pp. 329-332, 2015.

[77] S. Chen, P. Li and D. Brady, "Determining the optimum grid-connected photovoltaic inverter size," *Solar Energy*, pp. 96-116, 2013.

[78] L. Barelli, G. Bidini and F. Bonucci, "A micro-grid operation analysis for cost-effective battery energy storage and RES plants integration," *Energy*, vol. 113, pp. 831-844, 2016.

[79] Q. Li, F. Bai, B. Yang, Z. Wang, B. El Hefni, S. Liu, S. Kubo, H. Kiriki and M. Han,

"Dynamic simulation and experimental validation of an open air receiver and a thermal energy storage system for solar thermal power plant," *Applied Energy,* vol. 178, pp. 281-293, 2016.

[80] S. Mukoyama, T. Matsuoka, H. Hatakeyama, H. Kasahara, M. Furukawa, K. Nagashima, M. Ogata, T. Yamashita, H. Hasegawa, K. Yoshizawa and Y. Arai, "Test of REBCO HTS magnet of magnetic bearing for flywheel storage system in solar power system," *IEEE Transactions on Applied Superconductivity,* vol. 25, no. 3, pp. 1-4, 2015.

[81] Y. Zhu and K. Tomsovic, "Optimal distribution power flow for systems with distributed energy resources," *International Journal of Electrical Power & Energy Systems,* vol. 29, no. 3, pp. 260-267, 2007.

[82] H. Nazaripouya, Y. Wang, P. Chu, H. Pota and R. Gadh, "Optimal sizing and placement of battery energy storage in distribution system based on solar size for voltage regulation," in *IEEE Power & Energy Society General Meeting*, 2015.

[83] E. Muñoz, G. Razeghi, L. Zhang and F. Jabbari, "Electric vehicle charging algorithms for coordination of the grid and distribution transformer levels," *Energy,* vol. 113, pp. 930-942, 2016.

[84] B. Wang, R. Huang, Y. Wang, H. Nazaripouya, Q. C. C. Chu and R. Gadh, "Predictive scheduling for Electric Vehicles considering uncertainty of load and user behaviors," in *IEEE/PES Transmission and Distribution Conference and Exposition (T&D),* 2016.

[85] E. Xydas, C. Marmaras and L. Cipcigan, "A multi-agent based scheduling algorithm for

adaptive electric vehicles charging," *Applied Energy,* vol. 177, pp. 354-365, 2016.

[86] W. Shi and V. W. Wong, "Real-time vehicle-to-grid control algorithm under price uncertainty," in *IEEE International Conference on Smart Grid Communications (SmartGridComm)*, 2011.

[87] J. Yang, L. He and S. Fu, "An improved PSO-based charging strategy of electric vehicles in electrical distribution grid," *Applied Energy*, vol. 128, pp. 82-92, 2014.

[88] A. Crossland, D. Jones and N. Wade, "Planning the location and rating of distributed energy storage in LV networks using a genetic algorithm with simulated annealing," *International Journal of Electrical Power & Energy Systems,* vol. 59, pp. 103-110, 2014.

[89] T. Sousa, H. Morais, J. Soares and Z. Vale, "Day-ahead resource scheduling in smart grids considering vehicle-to-grid and network constraints," *Applied Energy,* vol. 96, pp. 183-193, 2012.

[90] P. Siano, C. Cecati, H. Yu and J. Kolbusz, "Real time operation of smart grids via FCN networks and optimal power flow," *IEEE Transactions on Industrial Informatics,* vol. 8, no. 4, pp. 944-952, 2012.

[91] N. Yadaiah, A. Kumar and J. Bhattacharya, "Fuzzy based coordinated controller for power system stability and voltage regulation," *Electric Power Systems Research,* vol. 69, no. 2, pp. 169-177, 2004.

[92] Z. Wang, K. Yang and X. Wang, "Privacy-preserving energy scheduling in microgrid systems," *IEEE Transactions on Smart Grid,* vol. 4, no. 4, pp. 1810-1820, 2013.

[93] J. Joo and M. Ilić, "Multi-layered optimization of demand resources using lagrange dual decomposition," *IEEE Transactions on Smart Grid,* vol. 4, no. 4, pp. 2081-2088, 2013.

[94] Y. Zhang and G. Giannakis, "Distributed stochastic market clearing with high-penetration wind power," *IEEE Transactions on Power Systems,* vol. 31, no. 2, pp. 895-906, 2016.

[95] S. Boyd, N. Parikh, E. Chu, B. Peleato and J. Eckstein, "Distributed optimization and statistical learning via the alternating direction method of multipliers," *Foundation and Trends in Machine Learning,* vol. 3, no. 1, pp. 1-122, 2010.

[96] W. Shi, X. Xie, C. Chu and R. Gadh, "Distributed optimal energy management in microgrids," *IEEE Transactions on Smart Grid,* vol. 6, no. 3, pp. 1137-1146, 2015.

[97] L. Wang, S. Sharkh and A. Chipperfield, "Optimal coordination of vehicle-to-grid batteries and renewable generators in a distribution system," *Energy,* vol. 113, pp. 1-37, 2016.

[98] W. Shi, N. Li, X. Xie, C.-C. Chu and R. Gadh, "Optimal residential demand response in distribution networks," *IEEE journal on selected areas in communications,* vol. 32, no. 7, pp. 1441-1450, 2014.

[99] S. Low, "Convex Relaxation of Optimal Power Flow—Part I: Formulations and Equivalence," *IEEE Transactions on Control of Network Systems,* vol. 1, no. 1, pp. 15-27, 2014.

[100] S. Low, "Convex Relaxation of Optimal Power Flow-Part II: Exactness," *IEEE Transactions on Control of Network Systems,* vol. 1, no. 2, pp. 177-189, 2014.

[101] B. Zhang and D. Tse, "Geometry of injection regions of power networks," *IEEE Transactions on Power Systems,* vol. 28, no. 2, pp. 788-797, 2013.

[102] A. Millner, "Modeling lithium ion battery degradation in electric vehicles," in *IEEE conference on Innovative Technologies for an Efficient and Reliable Electricity Supply (CITRES)*, 2010.

[103] J. Eckstein, "Parallel alternating direction multiplier decomposition of convex programs," *Journal of Optimization Theory and Applications,* vol. 80, no. 1, pp. 39-62, 1994.

[104] W. Kersting, "Radial distribution test feeders," in *Proc. IEEE PES Winter Meet.*, 2001.

[105] ERCOT, "Day-ahead Energy Price," [Online]. Available: http://www.ercot.com/.

[106] Cornell University Facilities Service, "Real Time Building Utility Use Data," [Online]. Available: http://portal.emcs.cornell.edu/.

[107] SAE, "SAE J1772 protocol," [Online]. Available: http://standards.sae.org/wip/j1772/.

[108] Z. Wang and S. Wang, "Grid Power Peak Shaving and Valley Filling Using Vehicle-to-Grid Systems," *IEEE Transactions on Power Delivery,* vol. 28, no. 3, pp. 1822-1829, 2013.

[109] H. M.-R. a. J. H. C. Wu, "Vehicle-to-aggregator interaction game," *IEEE Transaction on Smart Grid,* vol. 3, no. 1, p. 434–442, 2012.

[110] S. Han, S. Han and K. Sezaki, "Estimation of Achievable Power Capacity From Plug-in Electric Vehicles for V2G Frequency Regulation: Case Studies for Market Participation,"

IEEE Transaction on Smart Grid, vol. 2, no. 4, pp. 632-641, 2011.

[111] Y. Gao, Y. Chen, C.-Y. Wang and K. Liu, "A contract-based approach for ancillary services in V2G networks: Optimality and learning," in *IEEE INFOCOM*, 2013.

[112] Z. Yang, S. Yu, W. Lou and C. Liu, "P^2 : Privacy-Preserving Communication and Precise Reward Architecture for V2G Networks in Smart Grid," *IEEE Transactions on Smart Grid,* vol. 2, no. 4, pp. 697-706, 2011.

[113] C. Sao and P. Lehn, "Autonomous load sharing of voltage source converters," *IEEE Transactions on Power Delivery,* vol. 20, no. 2, pp. 1009-1016, 2005.

[114] H. Pota, "Droop control for islanded microgrids," in *IEEE Power and Energy Society General Meeting*, 2013.

[115] E. Coelho, P. Cortizo and P. Garcia, "Small-signal stability for parallel-connected inverters in stand-alone AC supply systems," *IEEE Transactions on Industry Applications* , vol. 38, no. 2, pp. 533-542, 2002.

[116] J. Simpson-Porco, F. Dorfler and F. Bullo, "Voltage stabilization in microgrids via quadratic droop control," in *IEEE 52nd Annual Conference on Decision and Control (CDC)*, 2013.

[117] X. Li, A. Dysko and G. Burt, "Enhanced mode adaptive decentralized controller for inverters supplying a multi-bus microgrid," in *IEEE/PES Innovative Smart Grid Technologies Europe (ISGT EUROPE)*, 2013.

[118] F. Lindholm, J. Fossum and E. Burgess, "Application of the superposition principle to solar-cell analysis," *IEEE Transaction on Electron Devices,* vol. 26, no. 3, pp. 165-171, 1979.

[119] H. Huang, J. Xu, Z. Peng, S. Yoo, D. Yu, D. Huang and H. Qin, "Cloud motion estimation for short term solar irradiation prediction," in *IEEE International Conference on Smart Grid Communications (SmartGridComm)*, 2013.

[120] G. Capizzi, C. Napoli and F. Bonanno, "Innovative Second-Generation Wavelets Construction With Recurrent Neural Networks for Solar Radiation Forecasting," *IEEE Transaction on Neural Networks and Learning Systems,* vol. 23, no. 11, pp. 1805-1815, 2012.

[121] R. Huang, T. Huang, R. Gadh and N. Li, "Solar generation prediction using the ARMA model in a laboratory-level micro-grid," in *IEEE International Conference on Smart Grid Communications (SmartGridComm)*, 2012.

[122] A. I. Negash, A. Hooshmand and R. Sharma, "A waveletbased method for high resolution multi-step PV generation forecasting," in *IEEE PES T&D Conference and Exposition*, 2014.

[123] F. Deng, G. Su, C. Liu and Z. Wang, "Prediction of solar radiation resources in China using the LS-SVM algorithms," in *International Conference on Computer and Automation Engineering (ICCAE)*, 2010.

[124] N. S. Altman, "An introduction to kernel and nearest-neighbor nonparametric regression,"

American Statistics, vol. 46, no. 3, p. 175–185, 1992.

[125] A. Mellit, M. Benghanem, A. Hadjarab, A. Guessoum and K. Moulai, "Neural network adaptive wavelets for sizing of stand-alone photovoltaic systems," in *IEEE Conference on Intelligent Systems*, 2004.

[126] S.-F. Su, C.-B. Lin and Y.-T. Hsu, "A high precision global prediction approach based on local prediction approaches," *IEEE Transactions on Systems, Man, and Cybernetics, Part C: Applications and Reviews*, vol. 32, no. 4, pp. 416-425, 2002.

[127] A. V. Oppenheim, R. W. Schafer and J. R. Buck, Discretetime signal processing, Englewood Cliffs: Prentice-hall, 1989.

[128] M. Kisacikoglu, B. Ozpineci and L. Tolbert, "EV/PHEV Bidirectional Charger Assessment for V2G Reactive Power Operation," *IEEE Transactions on Power Electronics* , vol. 28, no. 12, pp. 5717-5727, 2013.

[129] A. Lam, K.-C. Leung and V. Li, "Capacity management of vehicle-to-grid system for power regulation services," in *IEEE Third International Conference on Smart Grid Communications (SmartGridComm)*, 2012.

[130] J. Soares, H. Morais, T. Sousa, Z. Vale and P. Faria, "Day-Ahead Resource Scheduling Including Demand Response for Electric Vehicles," *IEEE Transactions on Smart Grid*, vol. 4, no. 1, pp. 596-605, 2013.

[131] C. Liu, K. Chau, D. Wu and S. Gao, "Opportunities and Challenges of Vehicle-to-Home, Vehicle-to-Vehicle, and Vehicle-to-Grid Technologies," *Proceedings of the IEEE,* vol.

101, no. 11, pp. 2409-2427, 2013.

[132] D. Tuttle, R. Fares, R. Baldick and M. Webber, "Plug-In Vehicle to Home (V2H) duration and power output capability," in *IEEE Transportation Electrification Conference and Expo (ITEC)*, 2013.

[133] H. Turker, A. Hably and S. Bacha, "Housing peak shaving algorithm (HPSA) with plug-in hybrid electric vehicles (PHEVs): Vehicle-to-Home (V2H) and Vehicle-to-Grid (V2G) concepts," in *Fourth International Conference on Power Engineering, Energy and Electrical Drives (POWERENG)*, 2013.

[134] Y. Ota, H. Taniguchi, H. Suzuki, T. Nakajima, J. Baba and A. Yokoyama, "Implementation of grid-friendly charging scheme to electric vehicle off-board charger for V2G," in *IEEE PES International Conference and Exhibition on Innovative Smart Grid Technologies (ISGT Europe)*, 2012.

[135] W. Kempton, V. Udo, K. Huber, K. Komara, S. Letendre, S. Baker and D. Brunner, "A test of vehicle to grid (V2G) for energy storage and frequency regulation in the PJM system," 2009.

[136] T. Gage, "The eBox: A New EV with Li Ion Battery and V2G," 2008.

[137] Sunspec Alliance, "Communicating the Customer Benefits of Information Standards," 2012.